
Theses and Dissertations

Summer 2011

Computational analysis applied to the study of post-traumatic osteoarthritis

Curtis Michael Goreham-Voss
University of Iowa

Follow this and additional works at: <https://ir.uiowa.edu/etd>



Part of the [Biomedical Engineering and Bioengineering Commons](#)

Copyright 2011 Curtis M. Goreham-Voss

This dissertation is available at Iowa Research Online: <https://ir.uiowa.edu/etd/1224>

Recommended Citation

Goreham-Voss, Curtis Michael. "Computational analysis applied to the study of post-traumatic osteoarthritis." PhD (Doctor of Philosophy) thesis, University of Iowa, 2011.
<https://doi.org/10.17077/etd.qf2atp8r>

Follow this and additional works at: <https://ir.uiowa.edu/etd>



Part of the [Biomedical Engineering and Bioengineering Commons](#)

COMPUTATIONAL ANALYSIS APPLIED TO THE STUDY OF POST-
TRAUMATIC OSTEOARTHRITIS

by
Curtis Michael Goreham-Voss

An Abstract

Of a thesis submitted in partial fulfillment
of the requirements for the Doctor of
Philosophy degree in Biomedical Engineering
in the Graduate College of
The University of Iowa

July 2011

Thesis Supervisor: Professor Thomas D. Brown

ABSTRACT

Post-traumatic osteoarthritis (PTOA) is a debilitating joint disease in which cartilage degenerates following joint trauma, including intra-articular fracture or ligament rupture. Acute damage and chronically altered joint loading have both been implicated in the development of PTOA, but the precise pathway leading from injury to cartilage degeneration is not yet known. A series of computational analyses were performed to gain insight into the initiation and progression of cartilage degeneration.

Finite element models of *in vitro* drop-tower impacts were created to evaluate the local stress and strain distributions that cartilage experiences during such experiments. These distributions were compared with confocal imaging of cell viability and histologically apparent matrix damage. Shear strain and tensile strain both appear to correlate with the non-uniform percentage of cell death seen in the impact region. In order to objectively evaluate structural damage to the cartilage matrix, an automated image processing program was written to quantify morphologic characteristics of cartilage cracks, as seen in histology slides. This algorithm was used to compare the damage caused by different rabbit models of PTOA and to investigate the progression of matrix damage over time. Osteochondral defect insults resulted in more numerous and more severe cracks than ACL transection. Interestingly, no progression of structural damage was identified between 8 weeks and 16 weeks in these rabbit PTOA models.

A finite element based optimization algorithm was developed to determine cartilage material properties based on the relaxation behavior of an indentation test. This was then used to evaluate the spatial and temporal progression of cartilage degeneration after impact. Impacting cartilage with 2.18 J/cm^2 through a metal impactor caused an immediate increase in permeability and decrease in modulus, both of which recover to nearly pre-impact levels within two weeks. Biologic testing suggests that the modulus changes were due to collagen fibril damage that is then repaired. Impacting with higher

energy caused material softening that did not return to normal, suggesting an impact injury threshold below which cartilage had some ability to repair itself.

To evaluate the effects of cartilage cracks on local stress and strain environments, finite element models of cracked cartilage were created. A physiologically-relevant, depth-dependent cartilage material model was developed and used to ensure accurate strains throughout the cartilage depth. The presence of a single crack was highly disruptive to the strain fields, but the particular shape or size of that crack had little effect. The most detrimental perturbations included two cracks within close proximity. When two cracks were within 0.5 mm of one another, the strain field between them increased in an additive fashion, suggesting a threshold for the amount of structural damage cartilage can withstand without being severely overloaded. The finite element models of cracked cartilage were also incorporated into an iterative degeneration simulation to evaluate the ability of mechanical loading to cause localized cartilage damage to spread to full-joint osteoarthritis.

Abstract Approved: _____
 Thesis Supervisor

 Title and Department

 Date

COMPUTATIONAL ANALYSIS APPLIED TO THE STUDY OF POST-
TRAUMATIC OSTEOARTHRITIS

by

Curtis Michael Goreham-Voss

A thesis submitted in partial fulfillment
of the requirements for the Doctor of
Philosophy degree in Biomedical Engineering
in the Graduate College of
The University of Iowa

July 2011

Thesis Supervisor: Professor Thomas D. Brown

Copyright by
CURTIS MICHAEL GOREHAM-VOSS
2011
All Rights Reserved

Graduate College
The University of Iowa
Iowa City, Iowa

CERTIFICATE OF APPROVAL

PH.D. THESIS

This is to certify that the Ph.D. thesis of

Curtis Michael Goreham-Voss

has been approved by the Examining Committee
for the thesis requirement for the Doctor of Philosophy
degree in Biomedical Engineering at the July 2011 graduation.

Thesis Committee: _____
Thomas D. Brown, Thesis Supervisor

Todd O. McKinley

Nicole M. Grosland

Jia Lu

Tae-Hong Lim

To my wife Jess, for her patient and caring support and my daughter Anna, who quickly became my favorite distraction from thesis writing

ACKNOWLEDGMENTS

I gratefully acknowledge and thank my colleagues and my friends at the Orthopaedic Biomechanics Laboratory for their assistance during the course of my studies. I would especially like to thank Dr. Thomas Brown for giving me the opportunity to become part of orthopaedic biomechanics at Iowa and for his continued support of my professional development. I am also greatly indebted to Julie Mock for her patient and friendly help with all manner of travel and organizational details. The students I have worked with at the biomechanics lab have been a pleasure to work and travel with, and I wish you all the best.

Virtually every member of the OBRL staff has assisted me in some phase of this project and I appreciate the efforts this involved. In addition, I would like to thank Dr. Jim Martin, for his patient explanations of cartilage biology, and the rest of the staff of the Ponseti Biochemistry and Cell Biology Lab, who prepared all of the histology, confocal, and biochemistry results presented in this dissertation work. Finally, I would like to thank my committee members, Drs. Todd McKinley, Nicole Grosland, Jia Lu, and Tae-Hong Lim, for contributing their time and ideas to this project.

This research was supported by funding from the National Institutes of Health (AR055533).

ABSTRACT

Post-traumatic osteoarthritis (PTOA) is a debilitating joint disease in which cartilage degenerates following joint trauma, including intra-articular fracture or ligament rupture. Acute damage and chronically altered joint loading have both been implicated in the development of PTOA, but the precise pathway leading from injury to cartilage degeneration is not yet known. A series of computational analyses were performed to gain insight into the initiation and progression of cartilage degeneration.

Finite element models of *in vitro* drop-tower impacts were created to evaluate the local stress and strain distributions that cartilage experiences during such experiments. These distributions were compared with confocal imaging of cell viability and histologically apparent matrix damage. Shear strain and tensile strain both appear to correlate with the non-uniform percentage of cell death seen in the impact region. In order to objectively evaluate structural damage to the cartilage matrix, an automated image processing program was written to quantify morphologic characteristics of cartilage cracks, as seen in histology slides. This algorithm was used to compare the damage caused by different rabbit models of PTOA and to investigate the progression of matrix damage over time. Osteochondral defect insults resulted in more numerous and more severe cracks than ACL transection. Interestingly, no progression of structural damage was identified between 8 weeks and 16 weeks in these rabbit PTOA models.

A finite element based optimization algorithm was developed to determine cartilage material properties based on the relaxation behavior of an indentation test. This was then used to evaluate the spatial and temporal progression of cartilage degeneration after impact. Impacting cartilage with 2.18 J/cm^2 through a metal impactor caused an immediate increase in permeability and decrease in modulus, both of which recover to nearly pre-impact levels within two weeks. Biologic testing suggests that the modulus changes were due to collagen fibril damage that is then repaired. Impacting with higher

energy caused material softening that did not return to normal, suggesting an impact injury threshold below which cartilage had some ability to repair itself.

To evaluate the effects of cartilage cracks on local stress and strain environments, finite element models of cracked cartilage were created. A physiologically-relevant, depth-dependent cartilage material model was developed and used to ensure accurate strains throughout the cartilage depth. The presence of a single crack was highly disruptive to the strain fields, but the particular shape or size of that crack had little effect. The most detrimental perturbations included two cracks within close proximity. When two cracks were within 0.5 mm of one another, the strain field between them increased in an additive fashion, suggesting a threshold for the amount of structural damage cartilage can withstand without being severely overloaded. The finite element models of cracked cartilage were also incorporated into an iterative degeneration simulation to evaluate the ability of mechanical loading to cause localized cartilage damage to spread to full-joint osteoarthritis.

TABLE OF CONTENTS

LIST OF TABLES	viii
LIST OF FIGURES	ix
CHAPTER 1. BACKGROUND AND SIGNIFICANCE.....	1
Cartilage structure, composition, and function.....	1
Composition and properties.....	1
Impact behavior and properties	3
Mechanobiology.....	4
Cartilage injury and degradation	6
Post-traumatic osteoarthritis	8
Presentation, prevalence, and current treatment strategies.....	8
PTOA etiology and potential treatments	10
Computational analysis and modeling of cartilage.....	12
Rationale.....	14
Center of Research Translation	15
CHAPTER 2. MODELING OF CARTILAGE IMPACTION	16
Development of a cartilage impact material model.....	18
Methods	18
Results	20
Validation of the cartilage impact material	21
Applications of FE modeling of cartilage impaction.....	23
CHAPTER 3. ASSESSMENT OF STRUCTURAL DAMAGE IN CARTILAGE	29
Development of a quantitative assessment of cartilage crack morphology.....	29
Methods	30
Inter- and intra-operator variability	34
Results	40
CHAPTER 4. CARTILAGE INDENTATION AND DEGRADATION.....	48
Methods	50
Results.....	56
CHAPTER 5. FINITE ELEMENT MODELING OF CARTILAGE CRACKS.....	68
Development of a depth-dependent cartilage material model.....	68
Methods	69
Results	76
Finite element modeling of the local stress environment around cartilage cracks	80
Methods	80
Results	84
A finite element model of cascading degradation in structurally-damaged cartilage.....	95
Methods	96

Results	98
CHAPTER 6. DISCUSSION.....	103
Limitations.....	110
CHAPTER 7. CONCLUSIONS	115
CHAPTER 8. ONGOING AND FUTURE WORK	118
Impact and indentation	118
Structural Cartilage Damage.....	119
Histology artifact.....	119
Additional database sources	121
Crack modeling and degeneration simulation	121
APPENDIX. DEPTH-DEPENDENT MATERIAL PROPERTIES.....	123
REFERENCES	129

LIST OF TABLES

Table 1. Insensitivity of the indentation material property optimization algorithm to varying start points.....	55
Table 2. Normalized properties following impact with 2.18 J/cm ² with standard deviations shown in parenthesis.....	57
Table 3. Correlation of impact characteristics with cartilage thickness.	60
Table 4. Correlation of material property changes at one week with impact characteristics.....	62
Table 5. Current specimens counts for cartilage explant impact series.....	111

LIST OF FIGURES

Figure 1.	Stress-strain curves from unconfined compression of a cartilage plug	3
Figure 2.	Stress-strain curve from impact loading of articular cartilage.....	4
Figure 3.	Three potential pathways from joint injury to the development of post-traumatic OA.....	10
Figure 4.	Representative stress-strain curves from impacts of bovine osteochondral explants.....	17
Figure 5.	Finite element model of metal-on-cartilage impact.....	19
Figure 6.	Hyper-viscoelastic cartilage material properties optimized to experimental impacts.	21
Figure 7.	Examples of experimental impact stress-strain curves and their corresponding computational models.	21
Figure 8.	Finite element model of cartilage-on-cartilage impact.	22
Figure 9.	Comparison of cartilage material model results with experimental results for 3.09 J/cm ² impacts.	23
Figure 10.	Deformed meshes for three series-average simulations at the time point of maximum compression.....	24
Figure 11.	Tensile and compressive strains at instant of maximum compression under three differing impact conditions.....	25
Figure 12.	Shear strain and pressure stress at instant of maximum compression under three differing impact conditions.....	25
Figure 13.	Confocal images of impacted cartilage. (a) Live and dead cells, green indicates healthy chondrocytes, red cells are damaged. (b) Isolated damaged cells.....	26
Figure 14.	Structural damage seen in cartilage impacted with 2.18 J/cm ² (M-C).	27
Figure 15.	Hoop and radial strains in cartilage impacted with 2.18 J/cm ² (MoC).....	28
Figure 16.	Typical histological image of cracked cartilage.	30
Figure 17.	Crack morphology program: (a) Histology loaded in GUI. (b) Thresholded image. (c) Articular surface and tidemark selected. (d) Cracks automatically identified and processed. (e) Close-up of processed cracks with centerlines.	32
Figure 18.	Summary of crack morphology parameters.	34

Figure 19. Crack morphology parameters for subset of images used for reproducibility testing, as a function of the OA model.	36
Figure 20. Crack morphology parameters for subset of images used for reproducibility testing as a function of the time-point.	37
Figure 21. Inter-operator reproducibility of crack morphology program.	37
Figure 22. Differences in categorical crack morphology output according to analyst, OA model, and time-point.	38
Figure 23. Intra-operator consistency on first repeated image.	39
Figure 24. Intra-operator consistency on second repeated image.	39
Figure 25. A comparison of one crack as analyzed by four different analysts.	40
Figure 26. Crack morphology characteristics between 8 week and 16 week specimens.	42
Figure 27. Specimen-level crack characteristics between 8 week and 16 week specimens.	43
Figure 28. Crack morphology characteristics among control and ACL transection specimens.	43
Figure 29. Specimen-level crack characteristics among differing levels of ACL transection.	44
Figure 30. Crack morphology characteristics among control and osteochondral defect specimens.	44
Figure 31. Specimen-level crack characteristics among differing sizes of osteochondral defects.	45
Figure 32. Crack morphology characteristics among control, ACL transection, osteochondral defect, and combined specimens.	45
Figure 33. Specimen-level crack characteristics among control, ACL transection, osteochondral defect, and combined models.	46
Figure 34. Effect of injury model on crack type.	47
Figure 35. Effect of injury model on subsurface cracks.	47
Figure 36. Element showing combination of fluid pressures (p) and solid matrix stresses (S_{ij}) acting on each material point in poroelastic and biphasic formulations.	48
Figure 37. Mechanical indentation testing. (a) Indentor and (b) close-up of spherical indentation tip approaching cartilage osteochondral specimen.	51
Figure 38. Axisymmetric finite element model of cartilage indentation.	52

Figure 39. Convergence of the reaction force curve as the mesh resolution was increased.	52
Figure 40. Optimization procedure for determination of cartilage properties from indentation results.	53
Figure 41. Examples of fit between experimental results (solid lines) and optimized finite element results (dashed lines).	56
Figure 42. Normalized properties following impact with 2.18 J/cm ²	57
Figure 43. Normalized material properties at explant center in unimpacted control specimens.	58
Figure 44. Typical examples of osteochondral specimens with depressed impacted region immediately after impact.	58
Figure 45. Normalized material properties at impact center.	59
Figure 46. Effect of pre-impact cartilage thickness on resultant impact characteristics.	61
Figure 47. Change in material properties at one week versus maximum impact stress and stress rate of change.	62
Figure 48. Illustration of coefficient of restitution.	63
Figure 49. Change in material properties at 1 day post-impact versus the impact energy absorbed.	64
Figure 50. Normalized property surfaces from cartilage-on-cartilage impact of 3.09 J/cm ²	66
Figure 51. Normalized property surfaces from metal-on-cartilage impact of 3.09 J/cm ²	66
Figure 52. Changes in the material properties at impact center under three different loading conditions: 3.09 J/cm ² cartilage-on-cartilage, 3.09 J/cm ² metal-on-cartilage, and 2.18 J/cm ² metal-on-cartilage.	67
Figure 53. Variation of cartilage material properties through depth.	70
Figure 54. Depth-dependence of cartilage properties, separated by testing speed and strain region, and normalized to maximum series values.	71
Figure 55. Compressive and tensile modulus variation with outliers removed.	72
Figure 56. Variation of Poisson ratios, normalized to series maximum, with depth.	73
Figure 57. Finite element model of unconfined compression, using two planes of symmetry.	77
Figure 58. Unconfined compression of cartilage from (a) experimental, and (b) depth-dependent finite element analysis.	78

Figure 59. Depth-wise variation of cartilage material properties.	78
Figure 60. Comparison of depth-dependent displacements from (a) physical tests, and (b) corresponding finite element simulations.	78
Figure 61. Comparison of (a-d) through-thickness cartilage strains from MRI testing with (e-h) corresponding finite element simulations.	79
Figure 62. Finite element model of cracked cartilage.	80
Figure 63. Mesh convergence approaching the crack opening.	82
Figure 64. Mesh convergence approaching the tip.	82
Figure 65. Final mesh for the baseline crack model.....	83
Figure 66. Perturbations to the crack geometry included altering the (a) crack angle relative to the local articular surface, (b) crack depth, and (c) crack width. (d) A hairline subsurface crack was created and (e) a series of geometries with two cracks of varying spacing was generated.	84
Figure 67. Fluid pressure and strain distributions in the uncracked and baseline crack finite element models.	85
Figure 68. Deformed meshes of the (a) uncracked, and (b) baseline crack FE models, both overlaid on the undeformed mesh of the uncracked model.	86
Figure 69. Line plots of the strain and pore pressure output were extracted along a path at depth 'd' parallel to the tibial articular surface, as shown.	86
Figure 70. Fluid pressure and strains at various relative depths from the articular surface in the uncracked model.....	87
Figure 71. Fluid pressure and strains at various depths from the articular surface in the baseline crack model.....	87
Figure 72. Fluid pressure and strains 100 μm below the articular surface as the crack width is altered.	88
Figure 73. Fluid pressure and strains 100 μm below the articular surface as the crack depth is altered.	89
Figure 74. Fluid pressure and strains 100 μm below the articular surface as the crack angle is altered.....	90
Figure 75. Comparison of the pore pressure in the uncracked, baseline crack, and 20° angle cracks.	91
Figure 76. Fluid pressure and strains 300 μm below the articular surface in the subsurface model.	92
Figure 77. Fluid pressure and strains 100 μm below the articular surface in the filled crack model.	93

Figure 78. Fluid pressure and strains 100 μm below the articular surface, as the proximity of two cracks is adjusted.	94
Figure 79. Deformed mesh for two cracks separated by 0.25 mm.	95
Figure 80. Examples of multiple cracks in cartilage histology.	95
Figure 81. Flowchart illustrating the functionality of the degeneration simulation algorithm, DEGEN.	97
Figure 82. Damage distributions for baseline crack under a shear strain damage law and a compressive strain damage law, after 10 iterations.	99
Figure 83. Comparison of compressive strains and tensile strains following 10 damage propagation cycles under shear and compressive strain damage laws.	101
Figure 84. Tensile strains before and after 10 iterations of degeneration simulation under the compressive damage law.	101
Figure 85. Damage distributions for two baseline cracks separated by 0.5 mm under a shear strain damage law and a compressive strain damage law, following 5 iterations.	102
Figure 86. Comparison of compressive and tensile strains following 10 damage propagation cycles under shear and compressive strain damage laws.	102
Figure 87. Time course of proteoglycan and proline content compared to that of elastic modulus following 2.18 J/cm^2 metal-on-cartilage impact.	107
Figure 88. Representative histology from unimpacted control specimens and 7 days and 14 days following impact with 2.18 J/cm^2	107
Figure 89. Histology of specimens impacted with 3.09 J/cm^2 . Arrows highlight structural damage.	108
Figure 90. Sample of WGA staining of impacted cartilage. WGA outline suggests impact-induced damage in (a), while the unstained edges in (b) suggest post-stain histology processing damage. (c) Cartilage plug with no significant damage shows visibility of WGA versus a counter-stain.	120

CHAPTER 1. BACKGROUND AND SIGNIFICANCE

Cartilage structure, composition, and function

Articular cartilage is a complex soft tissue covering diarthrodial joints. It has unique compositional and functional properties that provide a smooth bearing surface with minimal friction. It is compliant enough that contacting layers will conform to one another, yet it is strong enough to withstand the varied and demanding loads experienced in the joint during day-to-day living. Cartilage is remarkably resilient, and is capable of functioning for decades without problem. In this section, the basic properties of cartilage and how they influence cartilage function are discussed.

Composition and properties

Cartilage has a heterogeneous, multiphasic composition. By wet weight, cartilage is approximately 70-80% water and electrolytes [1]. The remaining solid phase consists largely of type II collagen (15%) and aggrecan (4%) along with smaller amounts of other proteins [2]. These components interact to give cartilage its unique mechanical properties. Collagen proteins are long chains which arrange as fibrils. These mechanically stiff fibrils [3] are embedded in a soft gel consisting mostly of large aggrecan molecules. The fluid phase of cartilage runs through the web of collagen and aggrecan, interacting both mechanically and electrochemically with the other components. Due to ionic interactions and mechanical impediments, cartilage has extremely low permeability, meaning that fluid moves very slowly through the solid phase [4]. Functionally, when cartilage is loaded, the fluid is pressurized and carries much of the load, since the low permeability prevents its egress. The collagen fibrils provide lateral reinforcement that restricts the deformation of the matrix [5]. If the load is sustained for an extended period, the fluid will eventually displace and more of the load will be transferred to the solid matrix [6]. Since the collagen fibrils do not contribute significantly to compressive stiffness, the soft aggrecan gel bears the load and

substantial deformation occurs. In healthy cartilage, the fluid phase will typically bear 70% or more of the applied load [7, 8].

Cartilage composition is also spatially heterogeneous. The orientation of collagen fibrils varies throughout the cartilage depth. In the superficial zone (the top 10-20%), collagen is oriented nominally parallel to the articular surface, in the transitional zone (middle 40-60%), the fibrils are randomly oriented, and in the deep zone (bottom 30%), the fibrils are nominally perpendicular to the subchondral bone [9, 10]. This results in cartilage having high tensile stiffness near the articular surface, and decreasing tensile stiffness through the depth. Furthermore, collagen arrangement varies across the artilage surface, as demonstrated by split lines initiated by pricking the articular surface [11, 12]. The tensile properties of cartilage are higher in the direction parallel to the primary collagen fibril alignment than perpendicular to it [13]. The proteoglycan (PG) distribution also varies through the cartilage depth and across the articular surface. In particular, PG content is highest in weight-bearing areas of the joint surface [14, 15].

Cartilage has a dynamic elastic modulus on the order of 10 to 20 MPa, under physiologic loading [16]. The equilibrium modulus of cartilage, i.e. the stiffness of the matrix after the fluid pressure has been allowed to dissipate, is usually reported in the range of 0.5 to 1.5 MPa [17-19]. The constituents of the solid matrix of cartilage are typically considered incompressible, and the bulk behavior of cartilage is nearly incompressible when cartilage is loaded at high rates [20]. However, under slow rates and sustained loading, fluid exudation occurs and the drained matrix is highly compressible.

Cartilage is both nonlinear and viscoelastic. As the stress-strain curves generated by Park et al. [21] show (Figure 1), cartilage displays toe and linear regions of low and high stiffness, respectively. The nonlinearity of cartilage arises both from increased recruitment of collagen fibrils, and from the nonlinear behavior of the fibrils themselves [3, 22]. At low rates of cyclic loading, cartilage is soft, and displays significant

hysteresis. As the loading rate is increased to physiologic (~ 1 Hz) and supra-physiologic (~ 40 Hz) frequencies, the degree of nonlinearity and hysteresis decreases. The rate-dependence of cartilage load uptake is due to the effect of fluid pressurization and flow, as well as to inherent viscoelastic properties of the collagen network.

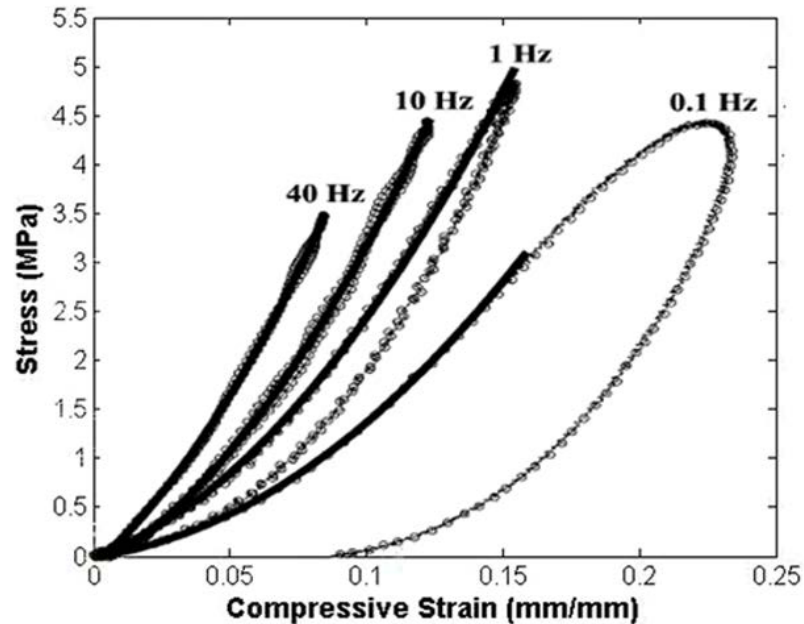


Figure 1. Stress-strain curves from unconfined compression of a cartilage plug

Impact behavior and properties

The biomechanical response of cartilage under impact is of enough significance to warrant special mention. Cartilage impact has been defined as loading resulting in peak stresses approaching 40 MPa, at stress rates ranging from 5 to 80 GPa/s [23]. Impact is of particular interest in the context of post-traumatic osteoarthritis, due to the loading rates experienced by cartilage during joint fracture or ligament rupture. Impact is frequently used to initiate cartilage degeneration in animal or *in vitro* studies.

Early work quantifying cartilage behavior under impact loading was performed by Finlay and Repo [24-28], with more recent follow-ups by Burgin and Aspden [23, 29, 30]. Those studies demonstrated that at impact loading rates, nonlinearity and hysteresis again appear in the stress-strain curves (Figure 2, contrast to the 40 Hz curve in Figure 1). Moduli during impact ranged from 30 to 100 MPa and the energetic coefficient of restitution (that is, the ratio of energy returned by the rebound of the cartilage to the energy expended compressing it) is in the range of 0.4 to 0.6. In some instances, cartilage was able to withstand stresses over 60 MPa without any indications of overt fracture, whereas in other instances cartilage structural damage occurred at stresses as low as 20 MPa.

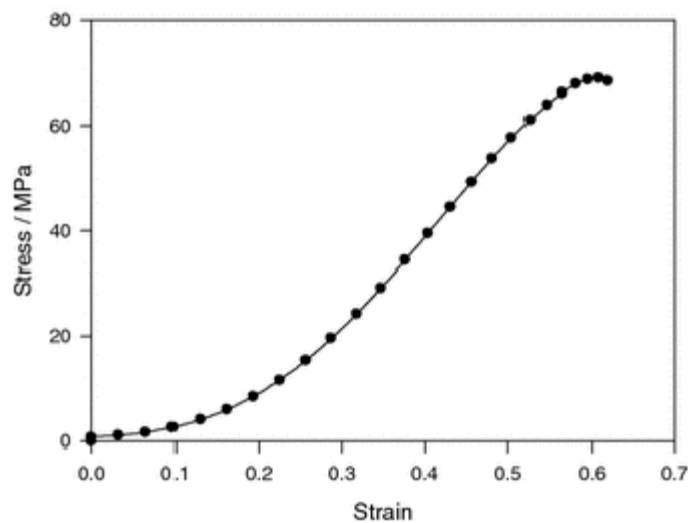


Figure 2. Stress-strain curve from impact loading of articular cartilage.

Mechanobiology

Cartilage is a mechano-sensitive tissue, that is, it responds biologically to mechanical loading. Chondrocytes, the single type of cell in cartilage, regulate the biosynthesis of all proteoglycan molecules, in a process that has been shown to be

sensitive to mechanical, electrical, and chemical stimulation [31-34]. Typically, chondrocyte activity is observed by monitoring the biosynthesis of aggrecan. Normal physiologic or sub-physiologic loading has been shown to invoke biosynthesis that maintains the cartilage matrix [35, 36]. As a later section will detail, extended periods of disuse or extended periods of increased loading can disrupt the normal biosynthetic process, resulting in cartilage degeneration.

The exact signals and cellular mechanisms that drive cartilage mechanobiology are not yet fully understood. Due to the complex nature of cartilage tissue, it is difficult to isolate loading modes. One possible signaling mechanism is that chondrocytes are sensitive to their own direct deformation. Imaging with confocal microscopy has demonstrated that chondrocytes experience substantial strain (15-20%) when a cartilage explant is loaded [37]. However, it is difficult to separate the effect of volumetric strain from that of the change in osmolarity, which also occurs with cartilage compression [38]. Pure shear strain has been used to induce deviatoric tissue strains without associated volumetric strains [39, 40]. Biosynthesis increased significantly under this loading, but it is not clear whether or not individual chondrocytes experienced volumetric strain. Hydrostatic pressure does not invoke deviatoric or volumetric strains in the chondrocytes, but has been shown to affect biosynthesis [41], likely through membrane pathways or through a response in the cytoskeleton [42, 43]. However, the relevance of purely hydrostatic loading to physiologic conditions is unclear.

Another possibility for chondrocyte mechano-transduction is interstitial fluid flow [44]. The majority of loading environments used to test cartilage invoke fluid pressure gradients and therefore result in interstitial fluid flow (the notable exception being hydrostatic fluid pressure). *In vitro* testing can cause fluid velocities on the order of 10 $\mu\text{m/s}$. *In vivo* articulation may invoke higher fluid velocities, although this has not been rigorously determined [6]. There are two possible mechanisms through which fluid flow may signal biologic response. The first is through the transport of solutes that are critical

to cartilage metabolism [45]. The second possibility is that interstitial fluid flow directly applies shear stress to chondrocytes. Studies using controlled fluid flow over isolated cells or cell monolayers have demonstrated alterations to biosynthesis in response to fluid-induced shear [46, 47]. Biosynthesis can be upregulated or downregulated in a dose-dependent response to the fluid shear level.

Cartilage injury and degradation

While cartilage can function for decades without problems, it is susceptible to injury and degradation. The previous section highlighted the stimulatory effects of moderate loading. Deviations from moderate or physiologic loading invoke detrimental mechanobiologic responses. Cartilage that is not subjected to regular loading has decreased biosynthesis and loses mechanical stiffness [48]. Cartilage that is overloaded experiences damage in the form of altered biologic responses, altered material properties, and matrix structural damage. These forms of damage can be correlated, but do not always occur together. Changes in material properties are prefaced by biologic response, as cartilage stiffness is governed by the content of proteoglycans and collagens, which in turn depends on chondrocyte function. Changes in material properties and biologic responses can both occur at levels well below those that cause structural damage [49]. Once structural damage in the form of cartilage cracks has occurred, changes in material properties become harder to interpret, since the changes in the structural stiffness cannot be distinguished from those in the inherent material properties.

Determining a single damage threshold for cartilage loading is not feasible, because cartilage responds differently depending on the type of load applied. Literature is largely unanimous on the deleterious effects of static stress on cartilage health. Flachsmann et al. showed that the articular surface of cartilage will rupture at 15 MPa under static loading [50]. Torzilli et al. found significant chondrocyte death when cartilage was compressed to 10% strain, although death was localized within the

superficial and upper transitional layers, even when nominal strains up to 70% were applied [51]. Several groups have shown decreases in aggrecan production under static loads of only 1 to 3 MPa [52, 53]. Quinn et al. have shown that static compression reduces solute transport in articular cartilage [54]. Of course, the relevance of extended static loading to *in vivo* physiologic loading is somewhat limited.

The influence of a single load-and-unload cycle or of dynamic cyclic loading is less clear-cut. While several studies have demonstrated the beneficial effect of physiologic levels of repetitive loading [35, 36], other studies have shown detrimental effects under surprisingly low levels of cyclic loading [55, 56]. It is likely that the stress magnitude, stress rate, and duration of loading all influence the cartilage response. In an *in vitro* study using a single, sub-impact load, Milentijevic and Torzilli showed that cell death extended further into the cartilage with slower stress rates and higher stress magnitudes [57]. This is likely because lower loading rates allow the fluid phase slightly more time to flow out from under the load, which in turn results in more matrix compression. *In vitro* studies have found decreased moduli, increased permeability, and higher rates of matrix damage when cartilage is cyclically loaded at loads above 10 MPa [58]. A study by Burton-Wurster et al. reported inhibition of proteoglycan, protein, and fibronectin synthesis following extended repetitive loading [52]. In a study using an external device to increase loading in live rabbits, Roemhildt et al. found increased permeability and thickness within 12 weeks of applying the device [59].

Impact is perhaps the laboratory mechanism most widely-used to study cartilage mechanobiology in relation to post-traumatic osteoarthritis. Controlled impacts administered through a drop-tower or pendulum have been employed in *in vitro* studies and in survival animal models [60-62]. Like sub-impact loading, the stress magnitude and stress rate of change have both been shown to affect the cartilage response [63, 64]. The biologic responses to cartilage impact include chondrocyte death [65], down-regulation of biosynthesis [66], up-regulation of matrix metalloproteinases (MMPs) [67],

and increased fibronectin fragments [68]. Cartilage material properties can change following impact, with the modulus decreasing and the permeability increasing. Swelling also can occur with the water content of the cartilage increasing by up to 10 to 15% [66]. Material property changes, cell death, and other biologic responses have all been shown to occur at impact levels beginning around half of what would be required to fracture the cartilage [49].

Post-traumatic osteoarthritis

The previous sections have described cartilage function, mechano-sensitivity, and injury. In this section, cartilage injury is discussed in the clinical context, where cartilage degeneration is seen in the form of osteoarthritis. Detection, prevalence, and current and promising treatment strategies will be discussed.

Presentation, prevalence, and current treatment strategies

Post-traumatic osteoarthritis (PTOA) is osteoarthritis that occurs secondarily to traumatic injuries such as intra-articular fractures or ACL ruptures. Osteoarthritic cartilage is softer and thinner than healthy cartilage, and appears dull and roughened as opposed to smooth and shiny. Fibrillation is seen in the surface of degenerating cartilage. In severe OA, cartilage can erode completely away, resulting in contact of the exposed underlying bone. In a clinical setting, PTOA patients present with joint pain and limited mobility. PTOA is confirmed through joint-space narrowing seen radiographically. However, neither joint-space narrowing nor joint pain occur until the disease has progressed to an advanced state, leaving physicians with limited options for treatment. The societal and financial burden of PTOA is high. One study has estimated that over 5 million people suffer or have suffered from significantly symptomatic PTOA, incurring direct healthcare expenditures of \$3 billion per year and total costs of \$12 billion per year [69].

Typical treatments for PTOA include pain management until joint replacement becomes necessary. As PTOA patients are typically younger and more active than the traditional arthroplasty cohorts, joint replacement is far less than ideal. In recent years, joint distraction has been studied as an alternative surgical treatment. In joint distraction, external fixation is used to reduce the load in articular cartilage for a period of typically 2-3 months, allowing cartilage to recover and joint space to be restored [70-72]. This has been shown to reduce patient pain and improve mobility, although external fixation devices are off-putting to many patients. Other possible surgical interventions prior to arthroplasty include arthroscopic lavage or debridement, bone marrow stimulation through microfracture or abrasion, or osteotomies to unload areas of degenerating cartilage. However, none of these techniques are particularly widespread, due to very specific indications and/or lack of rigorous scientific studies supporting their use [73].

Due to the limited treatment options available for late-stage PTOA, there is considerable research effort dedicated to detecting PTOA at an earlier stage. MRI techniques including T2 imaging, T1 ρ , and dGEMRIC are being used to detect compositional changes in cartilage such as increased water content or decreased proteoglycans [74-76]. Similarly, arthroscopic assessments of cartilage integrity and composition through indentation and ultrasound have been piloted [77-79]. Some of these techniques hold substantial promise for earlier detection and intervention in PTOA, although many questions remain regarding clinical implementation, and interpretation of the output data. Improving early detection will also assist with refining the ability to predict which patients will progress to full-joint degeneration. Certain classes of injuries have been shown to be more likely to progress to PTOA than others. PTOA is common following intra-articular fracture of the tibial-talar joint and after ACL ruptures, but it is less common in the hip (where primary osteoarthritis dominates) [80, 81]. Meniscus tears have also been implicated in PTOA development [82]. However, it is still difficult to tell with any certainty which patients with fractures or ligament ruptures will progress

quickly to PTOA and which will not. Ongoing work involving CT-based metrics and residual contact stress exposures is seeking to improve the prediction of long-term joint function [83].

PTOA etiology and potential treatments

Although *in vitro*, survival animal, and clinical studies have identified specific loading events and cellular responses associated with cartilage degeneration, the precise pathways leading from joint injury to PTOA are still unknown. It is likely that a combination of several factors contribute to joint degeneration, as illustrated in Figure 3. All of these pathways involve abnormal mechanical loading, triggering a biologic response.

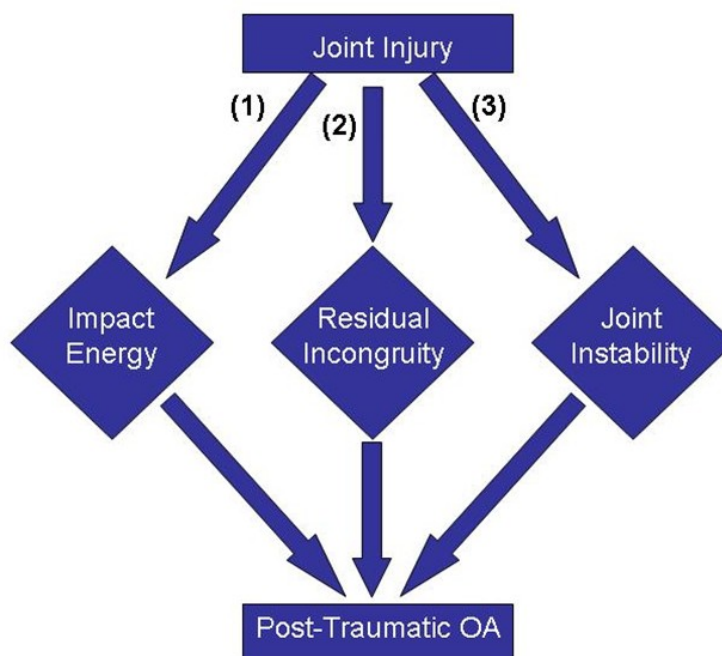


Figure 3. Three potential pathways from joint injury to the development of post-traumatic OA.

Buckwalter and Brown have suggested that the severity of a traumatic injury (pathway 1 in Figure 3) predisposes a joint to developing post-traumatic OA [84]. Supporting evidence comes from a study by Thompson et al., in which osteoarthritic cartilage changes were found in a canine model only six months after a significant transarticular load [85]. This is also supported by the large number of *in vitro* studies demonstrating cartilage damage following a single impact. In fact, a study by Jeffrey et al. found a high inverse correlation between chondrocyte viability and impact energy [86]. This factor has not been extensively addressed in clinical studies, largely due to the difficulty of quantifying injury severity in a clinical setting. The fracture severity measures developed by Anderson et al. were designed to address this problem [83, 87-89]. Using CT data from fractured limbs, they were able to calculate impact energy from the liberated interfragmentary surface area, and they identified a threshold energy level above which nearly all patients progressed to symptomatic PTOA.

Residual articular incongruities remaining after reconstructive surgery for intra-articular fracture (pathway 2 in Figure 3) have been extensively studied for their relationship to post-traumatic OA. Clinical studies of the effect of articular incongruities in the knee and hip have not been fully conclusive, with some studies showing that the presence of incongruities correlates highly with cartilage degeneration [90, 91], but with other studies finding limited correlation [92]. Biomechanical tests have demonstrated an increase in joint contact pressures in the presence of an articular incongruity [93-96]. However, Brown et al. have shown in a cadaver study that such increases in contact pressures in the knee do not become significant until a step-off incongruity reaches at least 1.5 mm [97]. No clear consensus has emerged regarding the accuracy of surface reduction necessary to prevent the development of post-traumatic OA. Recent work by Anderson et al. has moved in the direction of correlating clinical outcome with *in vivo* biomechanical conditions by means of patient-specific finite element models of fractured

joints, with OA propensity indexed in terms of chronic contact stress over-exposure [98, 99].

Another potential determinant of the development of post-traumatic OA is the degree of stability a joint experiences after injury (pathway 3 in Figure 3). Articular incongruities, ligament tears, and meniscal damage can result in a loss of normal mechanical constraints. This leads to abnormal joint motion, or instability [84]. Considerable clinical experience shows that joint instability is associated with cartilage degeneration [100-104]. Canine models of joint instability have been shown to progress to osteoarthritis, corroborating clinical findings [105-107]. Lovasz et al. have shown that a very small articular incongruity in a rabbit knee will result in pronounced cartilage degeneration if that incongruity results in an unstable joint [108].

In a series of cadaver tests, McKinley et al. have shown that instability resulting from an articular incongruity significantly changes the contact mechanics of the tibial-talar joint [109-111]. Those studies have indicated increased contact pressures, as well as increased temporal and spatial gradients of contact pressures. When considered with respect to the fore-mentioned studies indicating the adverse response of cartilage to abnormal mechanical stimuli, the results found by McKinley et al. appear to indicate a high possibility of instability as a trigger for post-traumatic OA.

Computational analysis and modeling of cartilage

Computational analyses have played a prominent and still-increasing role in PTOA research. Computational processing offers objective, quantitative output data in place of subjective observations. An excellent example of this is the automated histology-grading program developed by Moussavi-Harami et al., in which several measurements of cartilage health (proteoglycan content, cellularity, etc.) were encoded into an image processing algorithm [112]. In a similar spirit, the fracture energy calculations of Anderson et al. can grade fracture severity with more repeatability and

objectively than the rank-order methods previously used [87]. Shamir et al. demonstrated that an automated image processing algorithm operating on clinical radiographs could predict progression to severe OA with 72% accuracy [113]. These automated analyses tend to be faster (or at least require less hands-on time) than clinician or scientist observations, so they can be performed on larger datasets and they result in more statistically reliable conclusions.

Finite element (FE) modeling of cartilage also provides quantitative information in PTOA research, usually representing data that would be extremely difficult, if not impossible, to obtain experimentally. Numerical and computational representations of cartilage have been used to determine cartilage material properties since the mixture theory of Green and Naghdi [114] was adapted to cartilage modeling [115, 116]. Subsequent modification and advancements to this model, now commonly referred to as a biphasic or poroelastic material model, have added discrete modeling of the collagen fibril network [5, 117], inherent viscoelastic effects in the extracellular matrix, various forms of non-linearity [118, 119], and triphasic modeling to address ion charges and osmotic effects [120, 121]. FE models have been used to investigate the functional role of cartilage components. Insights gained in this manner include the laterally supporting role of collagen fibrils [122], the self-sealing effect caused by strain-dependent permeability [123], and the high percentage of load carried by the interstitial fluid of cartilage [8].

FE models at the full-joint level have been used to elucidate the differences in joint loading that lead to, or result from, PTOA. For example, Goreham-Voss et al. [124] created a poro-elastic model of an ankle experiencing different degrees of instability due to an incongruity, and showed that such instability could increase local stresses two-fold and increase local stress rates of change by five-fold. Chantarapanich et al. [125] created patient-specific linear elastic finite element models of the knee joint, to evaluate the difference in contact stress between normal and osteoarthritic knees. Yang et al. [126]

created subject-specific finite element models of two patients with differing knee alignment, and simulated the effects of meniscectomies on the resulting cartilage stresses. As previously mentioned, Anderson et al. have performed a series of patient-specific finite element analyses of fractured and intact ankles and developed a contact stress exposure metric that can predict OA development with reasonable accuracy [98, 99].

Rationale

Post-traumatic osteoarthritis is a painful and burdensome disease that can affect patients in their most active years. PTOA can transform a simple injury incurred through normal daily activity from a temporary setback to a life-long impediment. Current treatment options are expensive, invasive, and carry their own sets of complications.

Despite considerable ongoing research into cartilage degeneration, the precise triggers and pathways leading to PTOA are still unknown. This significantly impedes attempts to develop new, more optimal treatment strategies for PTOA. Several aspects of current PTOA research would benefit from the precise, quantitative data of computational analysis and simulation. In particular, four major questions arise:

1. What local strain and stress distributions develop in cartilage during commonly used impact experiments, and could these distributions be used to narrow the list of candidates for cellular signaling leading to degeneration?
2. How does the structural damage to cartilage change over time, and how do the damage created by different PTOA models compare to one another, as well as to clinical cartilage damage?
3. What are the precise spatial and temporal evolutions of cartilage material properties following traumatic loading, and do these evolutions suggest mechanobiologic pathways that may be either interrupted or amplified as a treatment option?

4. Could altered strain environments around cartilage cracks be responsible for the increased chondrocyte death observed in that region, and could chronic loading conceivably cause localized degeneration to spread into full-joint osteoarthritis?

The development and application of computational tools to assess each of these questions is addressed in Chapters 2 through 5, respectively. Chapters 6 and 7 provide discussions, limitations, and conclusions from the completed work. Chapter 8 discusses additional work that is planned, or already underway, to improve or expand the interpretation of existing data.

Center of Research Translation

Much of analysis completed for this project was performed within the context of an NIH-funded Center of Research Translation (CORT) entitled *New Approaches to Assess and Forestall Osteoarthritis in Injured Joints*. This broad CORT program is a consortium of biomechanists, biologists, and surgeons using bench-top and animal experiments, imaging, and clinical patient populations to gain further insight into the development of PTOA. As such, this program provides an excellent resource for the various source data (histology, mechanical indentation tests, biochemical assays, etc.) upon which the analyses here were performed.

CHAPTER 2. MODELING OF CARTILAGE IMPACTION

In post-traumatic osteoarthritis research, cartilage impact is frequently used to invoke tissue degeneration. The specific methodology of these impacts varies between research groups, from drop-tower impacts of osteochondral specimens to pendulum impacts of cadaver or live-animal joints. In most cases, the impact is delivered through a metal platen directly to the articular surface, although in some experiments the joint is left intact and the impact is delivered through adjacent bone. Regardless of the methodology, the goal of such an impact is to mimic, in a controlled manner, the traumatic injury cartilage experiences during a joint fracture or ligament rupture. Through these experiments, cartilage injury thresholds can be tested and the time-course of cartilage degeneration can be followed, since the exact time and energy of the impact are known.

Cartilage impacts are generally quantified in terms of energy delivered and resultant stress or stress rates of change. The impact energy (E) is a straightforward calculation from the drop height (h), drop mass (m), and acceleration due to gravity (g):

$$E = m \cdot g \cdot h . \quad (2.1)$$

The nominal impact stress ($\sigma(t)$) can be derived from the output of an accelerometer attached to the drop mass, by multiplying the acceleration ($a(t)$) by the drop mass and dividing by the nominal area (A) of the impact face:

$$\sigma(t) = \frac{a(t) \cdot m}{A} . \quad (2.2)$$

It is sometimes useful to evaluate cartilage impact response in terms of a stress-strain curve. Nominal strain ($\epsilon(t)$) can be calculated by integrating the acceleration twice with respect to time, and dividing by the (pre-impact) cartilage thickness (th):

$$\epsilon(t) = \frac{\iint a(t) \cdot dt}{th} . \quad (2.3)$$

From these stress-strain curves (Figure 4), the nonlinearity and energy-absorbing properties of cartilage are clearly evident.

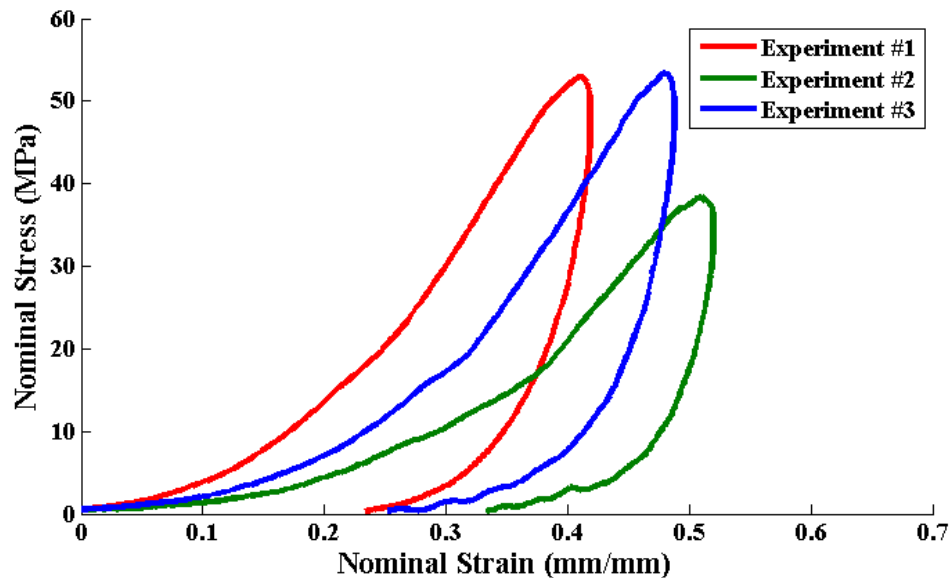


Figure 4. Representative stress-strain curves from impacts of bovine osteochondral explants.

Drop-tower impacts are a useful modality to quantify the spatial and temporal progression of cartilage degeneration. The particular preparation most commonly addressed in the present work is a 25 mm square osteochondral specimen excised from the weight-bearing portion of bovine tibial plateaus. The osteochondral specimen was affixed to a metal plate with polycaprolactone (chosen for its adhesion, non-toxicity, and attractive curing time and temperature) for spatial registration of indentation results with the impact center (indentation is the subject of Chapter 4). Following evaluation of the cartilage thickness with ultrasound, the specimens were impacted in a drop tower with a brass platen, and the impacts were quantified as described above. A variety of mechanical, biologic, and histologic assessments of the cartilage were thus enabled.

Development of a cartilage impact material model

Nominal stress-strain curves provide a useful way to evaluate the gross response of cartilage to various perturbations of impact parameters; however, they provide limited information about the local stresses and strains chondrocytes experience. This is an ideal application for computational simulations to bridge the gap between mechanical insult and biologic response. Although computational models of cartilage are plentiful in the literature, very few attempts have been made to model cartilage under impact loading conditions. Historically, the poroelastic formulations for physiologic loading have not been able to accommodate the high stresses (50+ MPa) and rapid loadings (<5ms to peak) characteristic of drop-tower impacts. It has been previously shown that incompressible elastic formulations have the same short-time response as a biphasic formulation, with the pressure term (one-third of the trace of the stress tensor) in the elastic formulation being equivalent to the pore (fluid) pressure in the biphasic formulation [127, 128]. Aside from these largely theoretical derivations, there have been no attempts to physically validate finite element material models of cartilage impact. In this project, a finite element model for cartilage impact was developed and validated versus experimental impacts. This material model was then used to evaluate changes in the experimental procedure, as well as to compare local stress and strain results to histologically-apparent damage.

Methods

An axi-symmetric finite element model of the physical drop tower impact was generated in Abaqus CAE (Figure 5). The impacted specimen consisted of cartilage, subchondral bone, and underlying cancellous bone layers. The subchondral bone was taken as 0.6 mm thick, and the cancellous bone was set such that the overall specimen height was 7 mm. The cartilage layer, nominally 3 mm thick, was adjusted to be specimen-specific, for comparison with corresponding physical experiments. The impact

platen was modeled as an analytical rigid surface, and a point mass was attached to the impactor surface. Using a point mass and a rigid surface considerably reduces the number of elements and corresponding computational time required, as compared to modeling and meshing the entire impactor and drop mass. The subchondral bone and cancellous bone were modeled as linearly elastic materials, with elastic moduli of 19.8 GPa and 760.3 MPa, respectively, and with Poisson's ratios of 0.4 [129, 130].

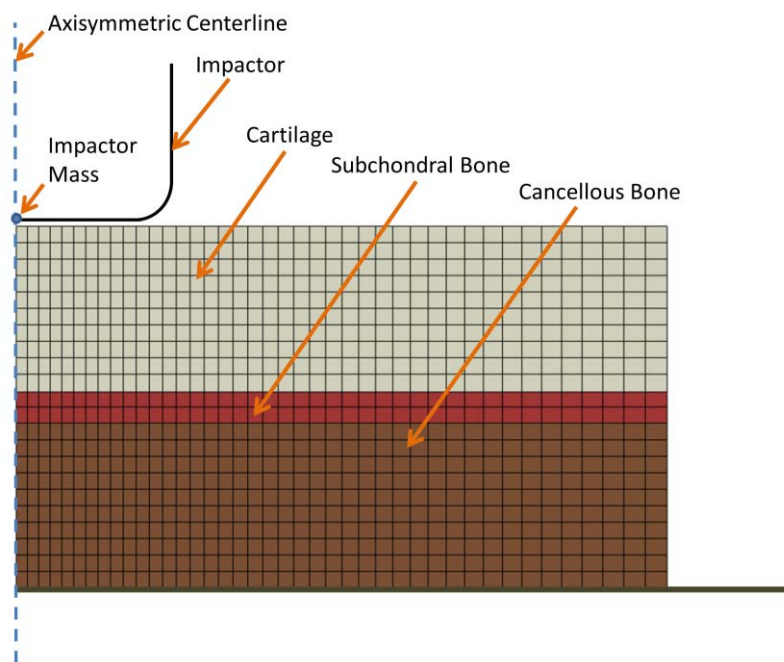


Figure 5. Finite element model of metal-on-cartilage impact.

Stress-strain curves such as those shown in Figure 4 clearly require a nonlinear material model. A hyperelastic model with a first-order Ogden strain energy potential (U) results in the correct concavity of the stress-strain curve (material stiffening with higher load), while requiring only two material properties, μ and α ,

$$U = \frac{2 \cdot \mu}{\alpha} (\lambda^{\alpha} + \lambda^{-\alpha} + \lambda^{-\alpha}) \quad (2.4)$$

where λ_i are the principal stretches. In addition, a viscoelastic component is necessary to accommodate the hysteresis apparent in the stress-strain curve. A relaxation function g_R , governing both the shear and volumetric moduli, was defined as,

$$g_R(t) = g - (g - g_0) \cdot (1 - e^{-t/\tau}), \quad (2.5)$$

where g is the relaxation coefficient and τ is the time constant.

A formal optimization of cartilage impact material properties was performed using an optimization algorithm originally developed for deriving material properties from cartilage indentation tests. A detailed description of this optimization algorithm can be found in Chapter 4. Briefly, the Abaqus impact analyses were parameterized such that they could be run from a custom-written Matlab function, which accepted a provisional set of material properties and returned the error between the computational and experimental results. Matlab's *lsqnonlin* optimization function was then used to determine material properties that minimized the difference between experimental and finite element curves. A set of 20 experimental osteochondral impacts were selected for impact material determination. Using an initial starting point determined by parametric state space sampling, the optimization algorithm was run on each impact.

Results

All impact tests were able to be fit to a very high degree of accuracy, with r -squared values ranging from 0.984 to 0.999 and averaging 0.996. The resultant material properties are shown in Figure 6. The average hyperelastic material properties for cartilage under impact are $\mu = 0.71$ MPa and $\alpha = 19.6$ (unitless), with viscoelastic properties of $g = 0.868$ (unitless) and $\tau = 0.158$ ms. Experimental impacts were chosen from specimens without evidence of significant structural damage following the impact. Thus, the material properties ascertained here are representative of inherent material (not structural) properties of healthy bovine cartilage. Three representative experimental stress-strain curves and their respective optimized fits are shown in Figure 7.

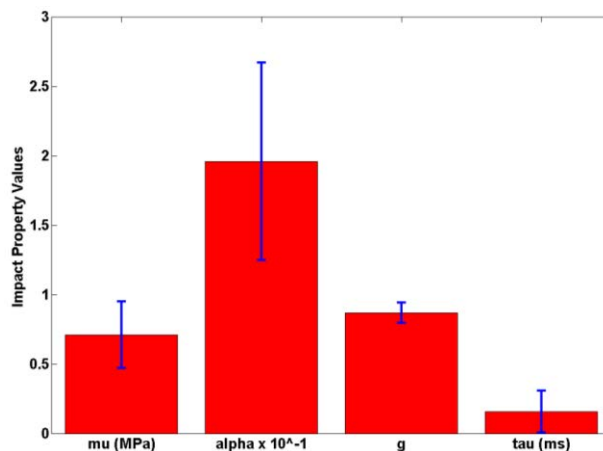


Figure 6. Hyper-viscoelastic cartilage material properties optimized to experimental impacts. Dispersion bars show standard deviation.

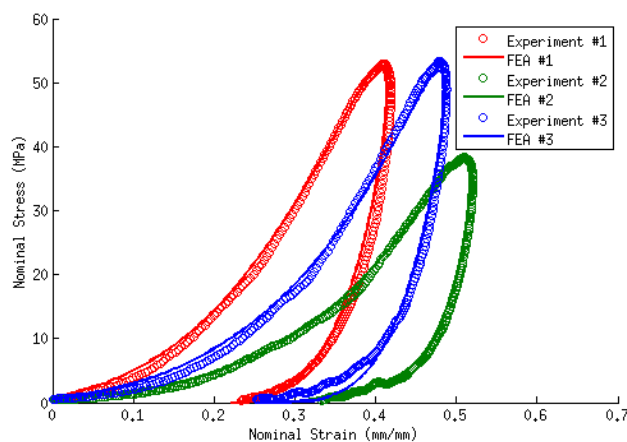


Figure 7. Examples of experimental impact stress-strain curves and their corresponding computational models.

Validation of the cartilage impact material

Additional work involved impact experiments where the metallic impactor was replaced with an osteochondral plug, in the interest of delivering a more physiologically relevant cartilage-on-cartilage (C-C) impact. These C-C impacts and an additional set of metal-on-cartilage (M-C) impacts utilized 3.09 J/cm^2 of impact energy, which is higher

than the 2.18 J/cm^2 used in most of the other impacts considered. These higher-energy impacts provide an opportunity to test the range of accuracy of the optimized cartilage impact material model. The finite element model was modified to include a platen tip consisting of cartilage, subchondral bone and cancellous bone (Figure 8). Bone properties were set as above, and the described impact material model was used for the cartilage. The average cartilage thicknesses for both the platen tip and the impacted specimen were calculated from the experimental impacts, and the FE model geometry was set accordingly. Similarly, simulations of both the 2.18 and 3.09 J/cm^2 impacts were performed using the average thicknesses from each respective series. Figure 9 shows the nominal stress for the average 3.09 J/cm^2 M-C and C-C impacts, overlaid on all of the experimental curves. The agreement is quite good, with similar peak stresses and stress rates of change. The higher energy M-C impact appears slightly softer than most of the experimental results; however, it is still within the range of experimental responses. To the author's knowledge, these simulations represent the first experimentally determined and validated cartilage impact material model for finite element analysis.

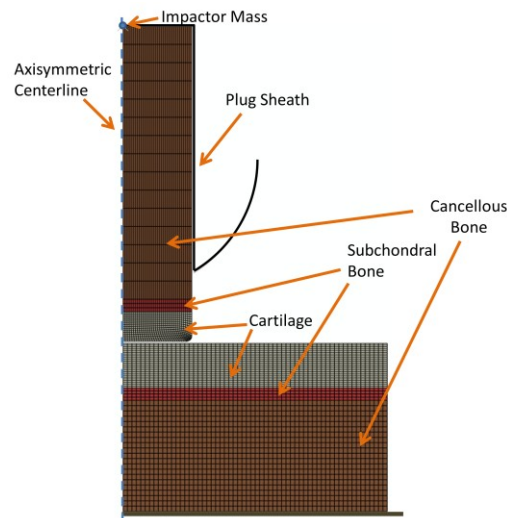


Figure 8. Finite element model of cartilage-on-cartilage impact.

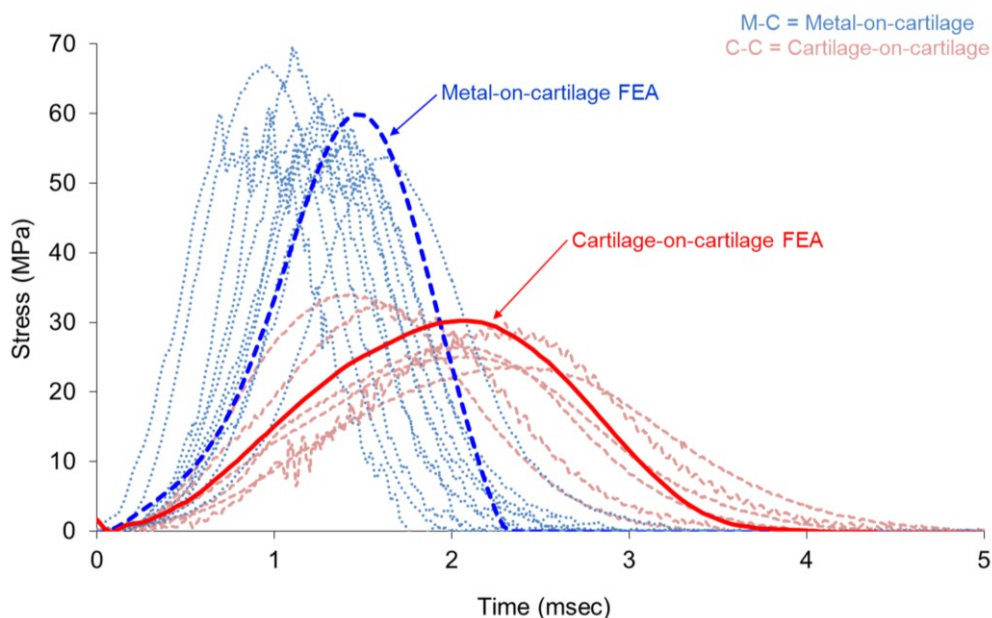


Figure 9. Comparison of cartilage material model results with experimental results for 3.09 J/cm^2 impacts.

Applications of FE modeling of cartilage impaction

The cartilage impact model was developed to help interpret experimental impacts through testing improvements to the experimental protocol and through providing supplemental information about cartilage stresses that could not be measured experimentally. This section details the application of the cartilage impact model to compare the local strains in the cartilage between different impact experiments, and to compare to histologic outcomes.

Three “series-average” simulations from the previous section provide an opportunity to compare the stress and strain distributions between different impact conditions. The three series are 3.09 J/cm^2 C-C, 2.18 J/cm^2 M-C, and 3.09 J/cm^2 M-C. These simulations all use the same (optimized) impact material model, and each simulation uses the average cartilage thickness of its respective series. Figure 10 shows

the deformed mesh for each of the three simulations, at the instant of maximum compression.

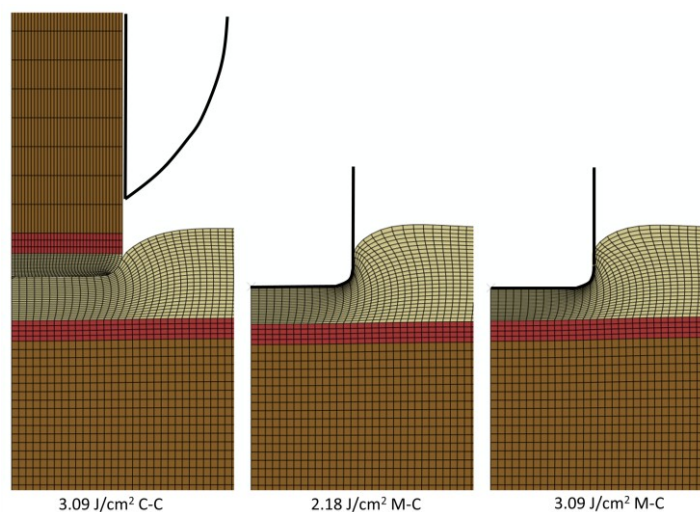


Figure 10. Deformed meshes for three series-average simulations at the time point of maximum compression.

Figures 11 and 12 show the compressive and tensile strains, and the shear strain and pressure in each of the three simulations at the point of maximum compression, displayed on the undeformed geometry. It is immediately clear (and unsurprising) that the M-C impacts result in higher strains and pressure throughout the cartilage than the C-C impacts. The non-uniform strain distributions developed depend upon the geometry of the impactor, with concentrated tensile, compressive, and shear strains shear the edge of the impactor. The pressure is highest in the deep zone of the cartilage, near the subchondral bone, suggesting that fluid load support is retained in that zone. Increasing the energy of the M-C impact by nearly 50% did not greatly affect the tensile or shear strains; however, doing so did induce a larger region of high compressive strains, and the deep zone pressure was substantially increased.

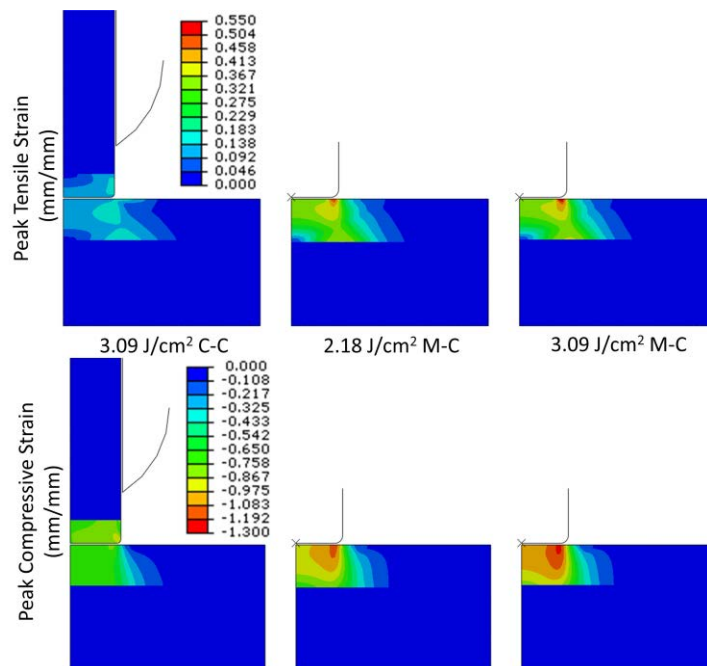


Figure 11. Tensile and compressive strains at instant of maximum compression under three differing impact conditions.

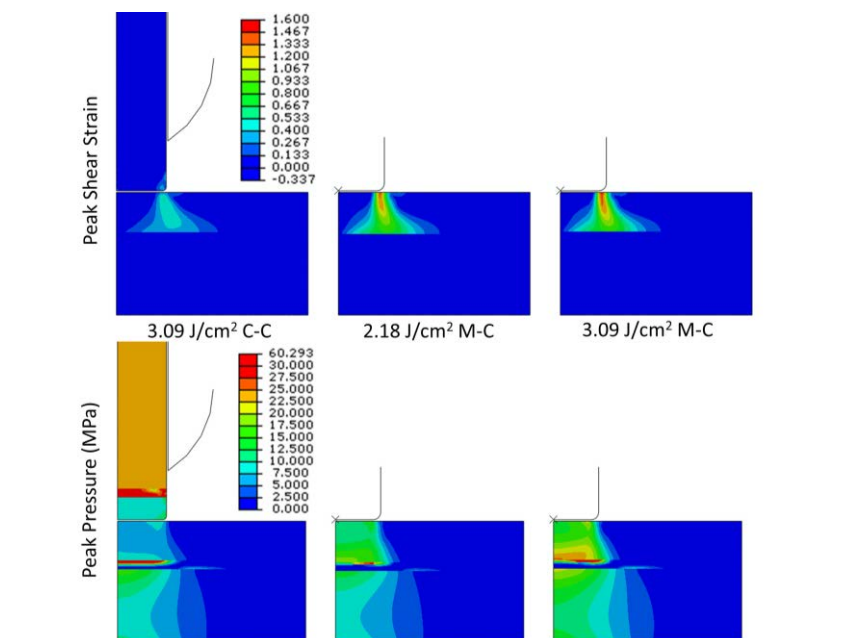


Figure 12. Shear strain and pressure stress at instant of maximum compression under three differing impact conditions.

It is interesting to compare the above strain and pressure distributions to confocal images of chondrocyte viability and death. Figure 13a shows a typical confocal image of impacted cartilage. This image gives the impression of a ring of concentrated cell death appearing near the outer radius of the impactor. However, the red (damaged) cell distribution is actually fairly uniform across the impact area (Figure 13b). The annulus seen in Figure 13a is actually an absence of healthy cells, rather than a concentration of damaged cells. In the center of the image, where red and green cells are both present, the larger and brighter green cells obscure the red cells. This makes the comparison of cell viability with impact stresses from FEA somewhat complicated. The distribution of damaged cells, in terms of absolute density of damaged cells, would seem to correlate with the relatively uniform distribution of pressure. The absolute density of healthy cells (inversely) correlates more strongly with the highly-localized distribution of shear strain. The uniformity of the cell death *fraction* would fall somewhere in between either the absolute healthy or damaged cell distributions, and may correlate well with compressive strain.

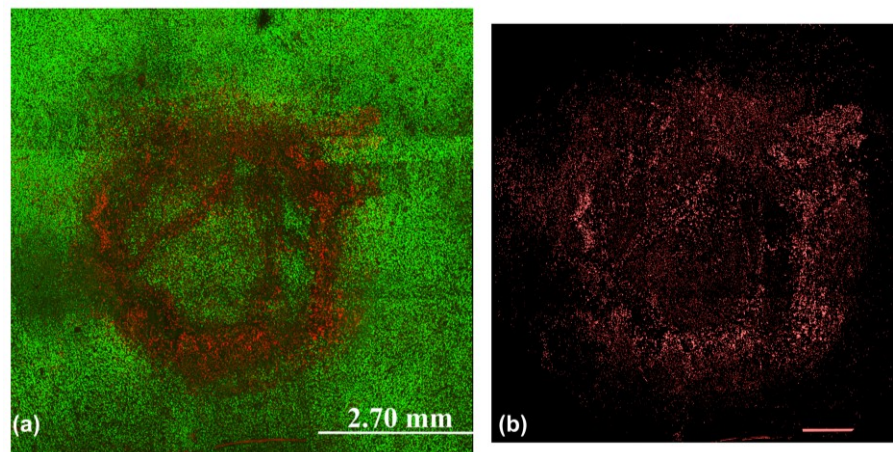


Figure 13. Confocal images of impacted cartilage. (a) Live and dead cells, green indicates healthy chondrocytes, red cells are damaged. (b) Isolated damaged cells.

The cartilage impact simulations also provide an opportunity to evaluate the relationships between strains and structural damage. Registration of histologically-apparent cracks to the impact site is very difficult to perform with any high degree of accuracy due to the lack of landmarks and the swelling and distortion that can accompany histologic preparation. Nonetheless, some gross comparisons are still possible. High tensile strains are seen in the superficial and transitional zones, which is consistent with the 30- to 50-percent depths of cartilage cracks seen histologically (Figure 14). Equibiaxial tensile strains (hoop and radial) develop under the flat portion of the impactor, while radial tensile strains dominate around the edge of the impactor (Figure 15). The shape of the high-shear-strain concentrations in Figure 12 is reminiscent of some of the cartilage cracks. However, if shear strains were the primary mode of failure, one would expect to see major cracks concentrated around the edge of the impact area in these cross-sectional histology images. Instead, the cracks seem to be distributed evenly across the specimen surface. Through evaluation of stress intensity factors, Kelly and O'Connor implicated tensile strains, as opposed to shear strains, in the propagation of superficial cartilage cracks during impact loading [131].

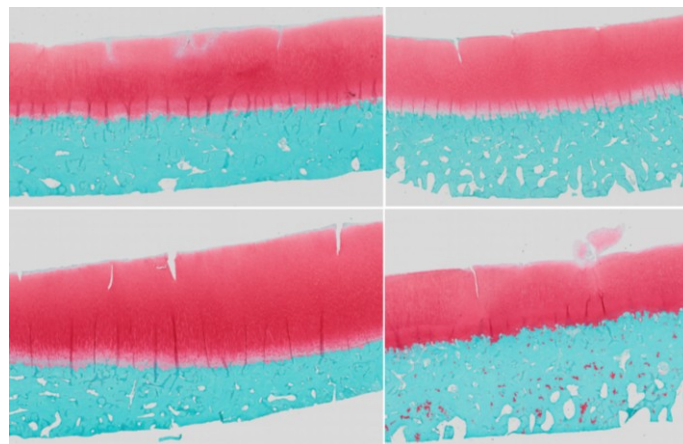


Figure 14. Structural damage seen in cartilage impacted with 2.18 J/cm^2 (M-C).

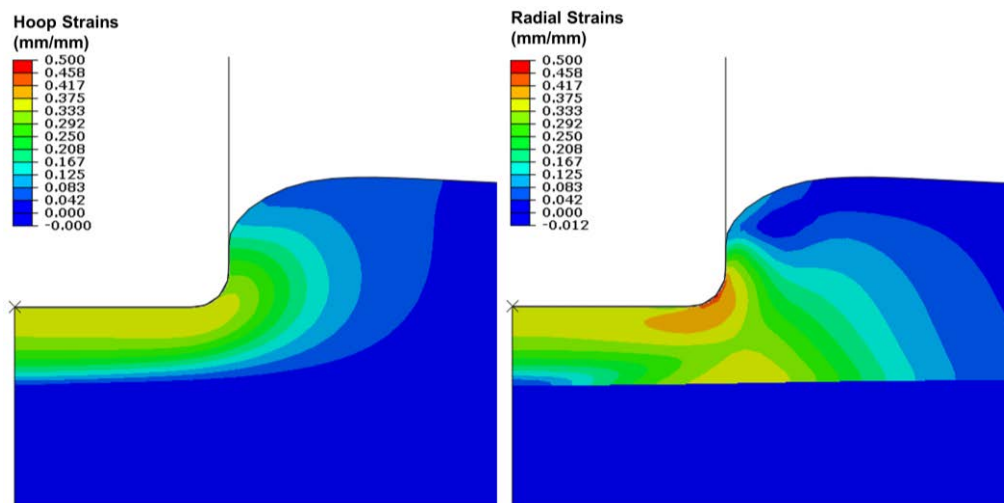


Figure 15. Hoop and radial strains in cartilage impacted with 2.18 J/cm^2 (MoC).

CHAPTER 3. ASSESSMENT OF STRUCTURAL DAMAGE IN CARTILAGE

Development of a quantitative assessment of cartilage crack morphology

Progressive cartilage degeneration can be recognized through a loss of proteoglycan, changes in material properties, changes in cellularity, chondrocyte death, and mechanical disruption of the cartilage matrix [62, 132, 133]. Of these indicators, mechanical damage in the form of cartilage cracks is perhaps the least extensively studied. Mechanical damage is typically reported only as a binary ‘present’ or ‘absent’ result [134-136], or, as in the case of the Mankin scale, the relative depth of representative cracks through the cartilage thickness is noted [137].

In a few studies, slightly more information has been collected about the form and morphology of cartilage cracks. Tomatsu et al. applied shear loads to porcine femoral condyles, and categorized the resulting cracks according to their ending location and whether they penetrated to the articular surface [138]. Krueger et al. quantified the total fissure lengths in the articular surface (i.e. from a ‘top-down’ view of the articular surface) of impacted cartilage, as well as the average fissure depth as a percentage of cartilage thickness [139, 140]. Another set of studies, by Flachsmann et al., examined cartilage cracks in the articular surface, analyzing the total rupture length and categorizing the rupture shape as linear or stellar [141, 142].

In reality, mechanical damage to cartilage takes a wide variety of forms, and its morphology may vary significantly depending on whether the damage is acute (impact, fractures, etc.) or long-term-chronic, and depending on the species and age of the cartilage and various other factors. In this chapter, a semi-automated algorithm is described which was developed to analyze cartilage histology sections, and to calculate a suite of morphologic characteristics of cracks and defects. This program can be used to

create a database of cartilage crack morphology from a variety of sources, including (1) the *in vitro* drop-tower impacts described in Chapter 2, (2) animal models using ACL transections and intra-articular fractures, and (3) human clinical samples retrieved from amputations and joint arthroplasties, or from human cadaver specimens. The accumulation of such a database provides guidance for geometry in the finite element modeling of cartilage cracks described in Chapter 5. The database also allows for the objective comparison of cartilage structural damage across the varied models used in PTOA research, and it allows the users of those models to objectively assess how relevant the resulting damage is to that seen in human patients.

Methods

The crack morphology program operates on histology images of cartilage such as are routinely prepared for Mankin grading. Osteochondral specimens were decalcified, embedded in paraffin, and sectioned to 5 μm thickness. The sections were then stained with hematoxylin, safranin-O, and fast green. The slides were digitized using a high-resolution camera mounted on an Olympus BX 60 microscope equipped with a 4X objective. A stepper-motor-driven stage passed the entire section under the objective, and individual images were concatenated into a single large image per section (all slide preparation work was performed by the Ponseti Biochemistry and Cell Biology Lab). An example of a histology slide with cartilage cracks is shown in Figure 16.



Figure 16. Typical histological image of cracked cartilage.

The crack morphology assessment program was written in Matlab. In a simple user interface (Figure 17), the user selects scanned slide images to be opened, and the first of the images is displayed on-screen. The RGB (red-green-blue) color formatted image is converted to grayscale, and an automatic grey-level threshold is calculated to segment the background from the cartilage and bone. The user can adjust this segmentation threshold as necessary. The user then selects several points to define the articular surface and the tidemark, the upper and lower cartilage bounds. The program automatically identifies all crack objects within the cartilage bounds. Objects smaller than 10 pixels are discarded, eliminating spaces left by unfilled chondrocyte lacunae. Each remaining object is then processed and quantified as an individual crack or defect. Following processing, the user is able to delete incorrectly identified cracks. The user can also manually outline cracks, which are then processed via the same routines as those used for the automatically identified cracks. Once a slide is completely processed, all crack and slide results are automatically saved, and the user advances to the next selected slide image.

During processing of an individual crack, thinning operations are used to reduce the crack to a series of distinct branches. Branch proximity and direction are evaluated, and branches determined to be in-line are recombined. The largest branch is identified as the crack centerline. If the crack is a surface crack (i.e. the crack breaches the articular surface), the centerline is constrained to pass through the center of the crack opening. Based on the branches and centerline, five morphologic characteristics are then calculated. The **Type** of the defect is set to 'Defect' if the number of branches is greater than 4 or if the ratio of the opening width of the crack to the crack length is greater than 0.8; otherwise, Type is set to 'Crack'. This distinguishes discrete fissures in the cartilage from large convoluted defects representative of crushing or material removal. The **Angle** of the crack is defined as the angle between a line fit to the centerline and a line fit to the local articular surface. The **Center Length** of the crack is the length of the centerline

only, while the **Total Length** is the combined length of all of the crack branches, including the centerline. The **Tortuosity** of the crack is a measure of the contorsion of the crack, defined here as

$$Tortuosity = 1 - \frac{Chord}{Center\ Length}, \quad (3.13)$$

where Chord is the distance between the start point and end point of the centerline. A tortuosity value of zero indicates a straight line, and higher values indicate more tortuous cracks.

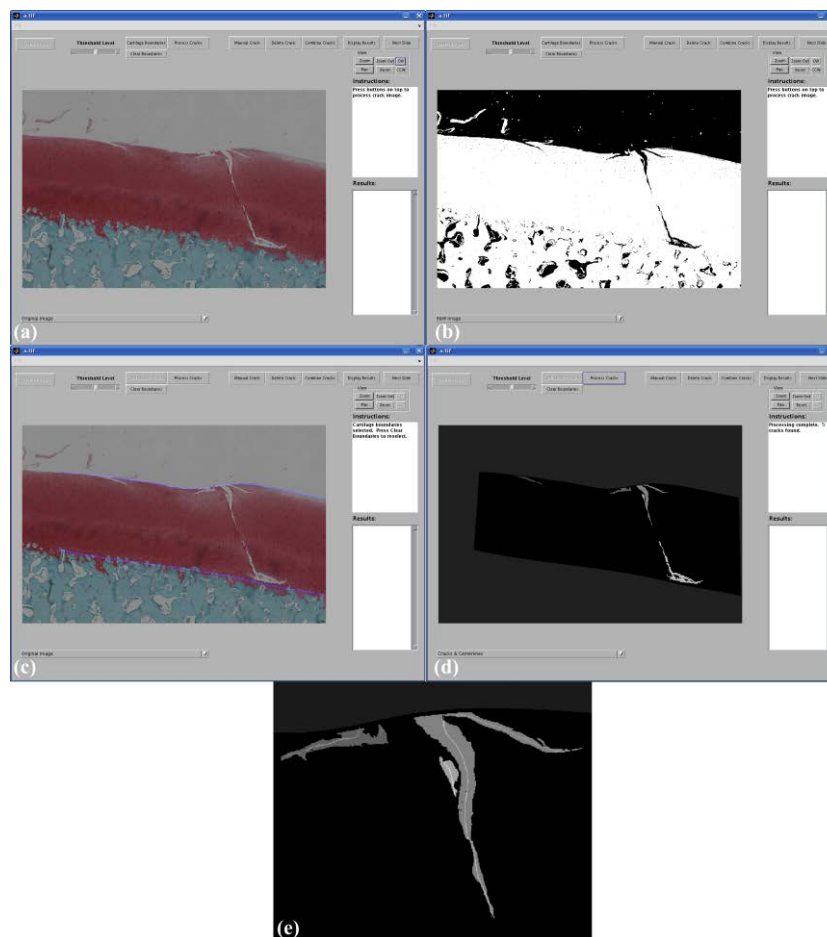


Figure 17. Crack morphology program: (a) Histology loaded in GUI. (b) Thresholded image. (c) Articular surface and tidemark selected. (d) Cracks automatically identified and processed. (e) Close-up of processed cracks with centerlines.

An additional eight morphologic characteristics are calculated from the original, unthinned defect object. The **Location** of the crack is set to ‘Surface’ if the crack breaches the articular surface, and ‘Subsurface’ otherwise. The **Opening Width** of the crack is the width of the crack at its opening to the articular surface (surface cracks only) and the **Area** of the crack is the total area of the crack. The **Encompassed Area** is calculated as the area within the convex hull of the crack, and is meant to include portions of cartilage severely undercut by a crack branch, where the mechanical stability of that portion of cartilage would be clearly compromised. The **Relative Depth** of the crack is the normalized distance the crack extends through the cartilage thickness, and the **Depth Range** is the percentage of the cartilage thickness through which the crack extends. The **Thickness** records the absolute thickness of the cartilage at the centroid of the crack. Finally, two additional parameters are calculated based on the perimeter of the crack and the centerline. Local crack widths are defined as twice the distance between the centerline point and the nearest perimeter point, at each point along the centerline. The **Average Width** can then be calculated as the mean of the centerline widths, which provides an overall sense of the crack width (as opposed to the width specifically at the opening). The **Width Deviation** is calculated as the standard deviation of the widths calculated along the centerline. This indicates whether a crack is of uniform width or of varied width, e.g. wide at the opening and thinning to a point. The crack morphology parameters are summarized and illustrated in Figure 18.

In a previous study of rabbit PTOA models, cartilage histology sections were prepared for a large series of rabbits subjected to different joint insults. In that study, OA was induced by a partial or complete transection of the ACL, by an osteochondral defect of 1, 1.5, 2 or 3 mm created in one of the femoral compartments, or by both a transection and a defect. Several non-operative control specimens were also processed. For each specimen, four mid-compartmental sagittal plane histologic sections were taken, one from each compartment (medial and lateral, tibial and femoral). The slides were Safranin-

O and fast green stained and digitized for processing, as described in the first paragraph of this section. As the next sections will detail, a subset of these slides were used to test the inter- and intra-operator variability of the crack morphology program, then the entire set was processed to determine the effect of different PTOA models on resulting structural damage to the cartilage. Significant differences between crack morphology parameters were tested using ANOVA on means (ordinal data) or chi-squared tests of proportions (categorical data).






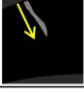
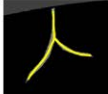

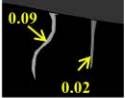
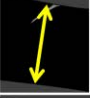
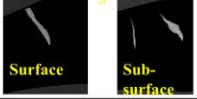
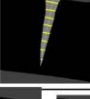
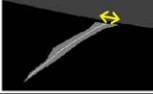

Parameter	Description	Illustration	Parameter	Description	Illustration
Type	'Cracks' for discrete cracks, 'Defect' for large disruptions with >5 branches.		Area	Total area of crack.	
Angle	Angle between line fit to centerline and local articular surface.		Encompassed Area	Area within convex hull of crack image. Includes areas that are obviously structurally compromised.	
Center Length	Length of centerline.		Relative Depth	Maximum depth of the crack, calculated as a percentage of the local thickness. Bound by [0 100].	
Total Length	Sum of all branch lengths, including centerline.		Depth Range	Percentage of the local thickness the crack extends through. Bound by [0 100]. For a surface crack, equal to relative depth.	
Tortuosity	Measure of the how tortuous the centerline is. Bound by [0 1], with a straight line having a tortuosity of 0.		Thickness	Local thickness of the cartilage at crack centroid.	
Location	'Surface' for cracks that breach articular surface, 'Subsurface' otherwise.		Average Width	Average width of crack, calculated along centerline.	
Opening Width	Width of surface crack at its opening in the articular surface.		Width Deviation	Standard deviation of crack widths along centerline. Distinguishes uniform width vs. non-uniform width cracks.	

Figure 18. Summary of crack morphology parameters.

Inter- and intra-operator variability

Since the purpose of the crack morphology program was to provide quantitative, objective information about structural damage in cartilage, the inter- and intra-operator

variability need to be evaluated. For these purposes four analysts, including the author of this thesis, served as program operators. A set of 21 slides with a wide range of structural damage was selected, with two of these slides replicated 3 times, thus resulting in a testing set of 25 slides. Following a brief practice period with a separate set of images, each analyst independently processed all 25 slides. The analysts were blinded to any information about the source of the cartilage damage, and they were not told ahead of time that there were repeated images. In many ways, this test could be considered a “worst case” scenario, since the analysts recruited, while experienced biomedical engineering graduate students, had no prior experience with cartilage histology. Analyst instructions were limited to describing how to operate the user interface; no instructions regarding interpretations of cracks were given.

Figures 19 and 20 show the crack morphology results for the subset of images used for the reliability testing (only the 21 unique slides are included), separated according to the OA model used and the time-point of the histology, respectively. The OA model results are lumped such that any degree of ACL transection is included in the ‘ACL’ group, any size of osteochondral defect is included in the ‘Defect’ group, and the specimens subjected to both ACL transection and osteochondral defect are included in the ‘Both’ group. Control specimens had no ACL transection or osteochondral defect.

The results of the inter-operator reproducibility testing are shown in Figure 21. Excellent agreement among analysts is shown, with only two parameters showing statistically significant differences. Two analysts had slightly different average opening widths. The opening width is determined from the intersection of the crack and the articular surface, the latter of which is a spline curve fit to selected points. The precise location of the spline curve can vary depending on the location of the points selected, especially relative to the narrow opening of most cracks. In addition, many cracks are significantly wider at the opening than at a few μm below the articular surface, due to superficial tearing of the cartilage. For this reason, the crack width is considered to be

more accurately represented by the mean crack width than by the opening width. Statistically significant differences between analysts were also seen in thickness. This is likely due to the ambiguity of determining the tidemark in many specimens. Further training presumably could reduce this variance. Inter-operator reproducibility for the categorical morphology outputs (Crack Type and Crack Location) are shown in Figure 22. No statistical difference was found among analysts for crack type, while a slight statistical difference was found for crack location, with one analyst identifying more subsurface cracks.

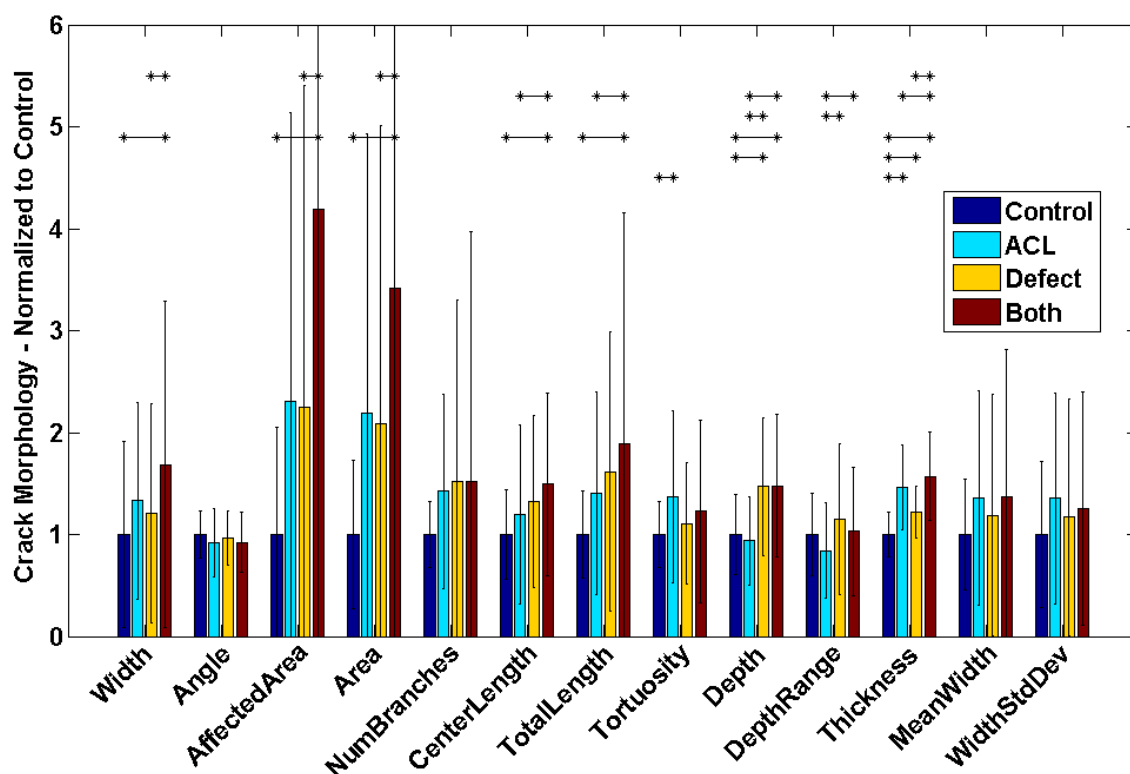


Figure 19. Crack morphology parameters for subset of images used for reproducibility testing, as a function of the OA model. Dispersion bars are standard deviations. Statistical significance ($p < 0.05$) of differences is indicated by horizontal bars.

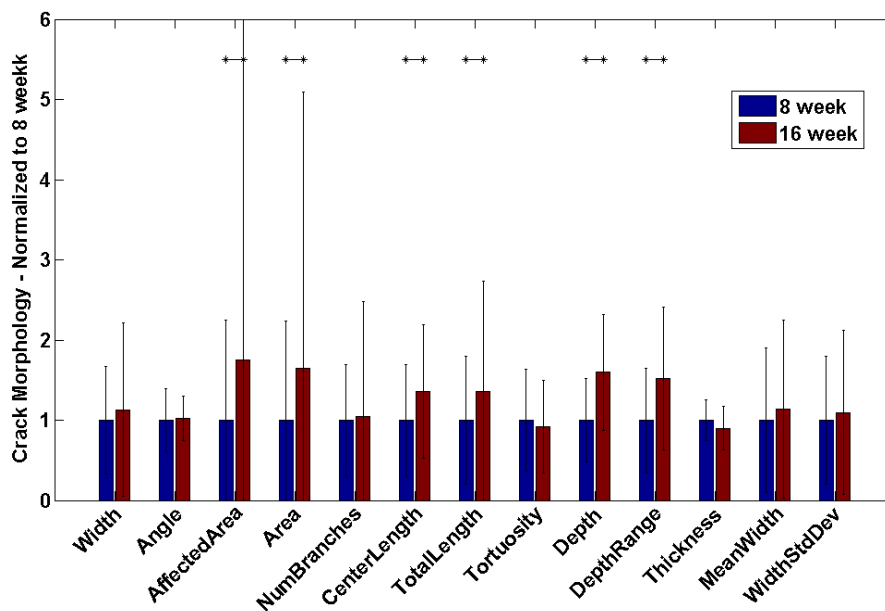


Figure 20. Crack morphology parameters for subset of images used for reproducibility testing as a function of the time-point. Dispersion bars are standard deviations. Statistical significance ($p < 0.05$) of differences is indicated by horizontal bars.

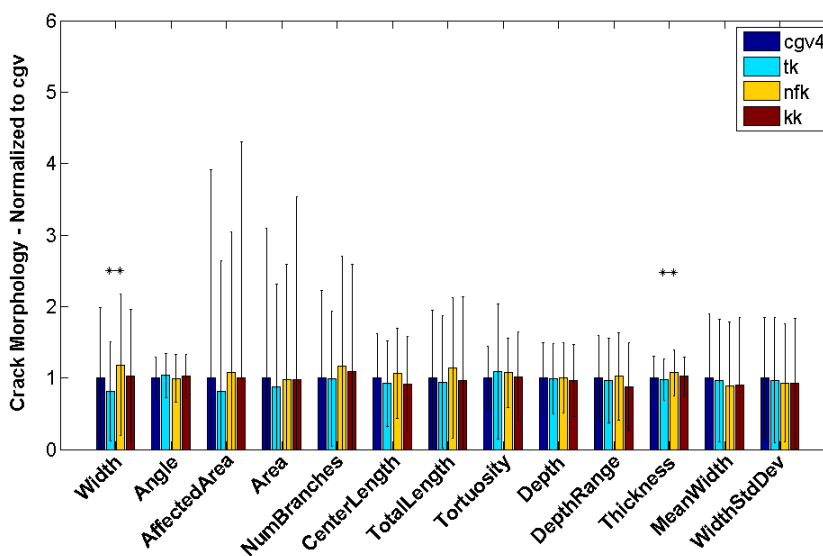


Figure 21. Inter-operator reproducibility of crack morphology program. Dispersion bars represent standard deviations, and horizontal bars indicate statistically significant differences ($p < 0.05$).

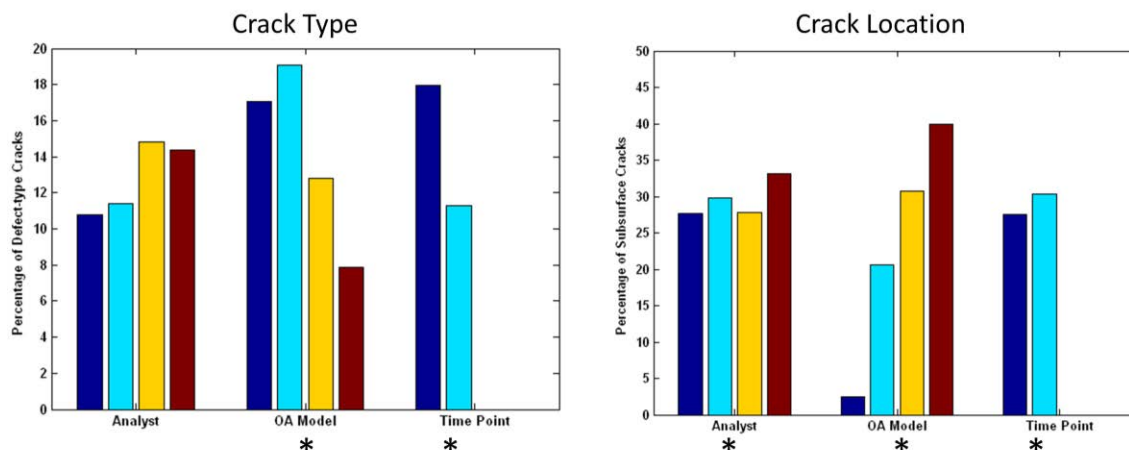


Figure 22. Differences in categorical crack morphology output according to analyst, OA model, and time-point. Asterisks indicate statistical significance ($p < 0.05$) among groups.

Intra-operator reproducibility was tested by comparing the resultant crack populations from the two slides that were each repeated three times. Figures 23 and 24 demonstrate excellent agreement between the three repeated slides, with no statistically significant differences, indicating high intra-operator consistency.

Figure 25 shows the output for one representative crack, as determined by each of the four analysts, and the maximum difference among the analysts' results. The variability of the opening width was evident, as the crack processed by cgV has a slightly extended tail on the left side of the opening, resulting in a maximum difference of 34.1% compared to the opening width determined by nfk. In this case, the affected area was also influenced by the extended opening, since it expanded the convex hull around the crack. However, the reliability of the mean width was also demonstrated. The maximum difference in mean width among the four analysts was less than 4%. All other output also had differences around 10% or less.

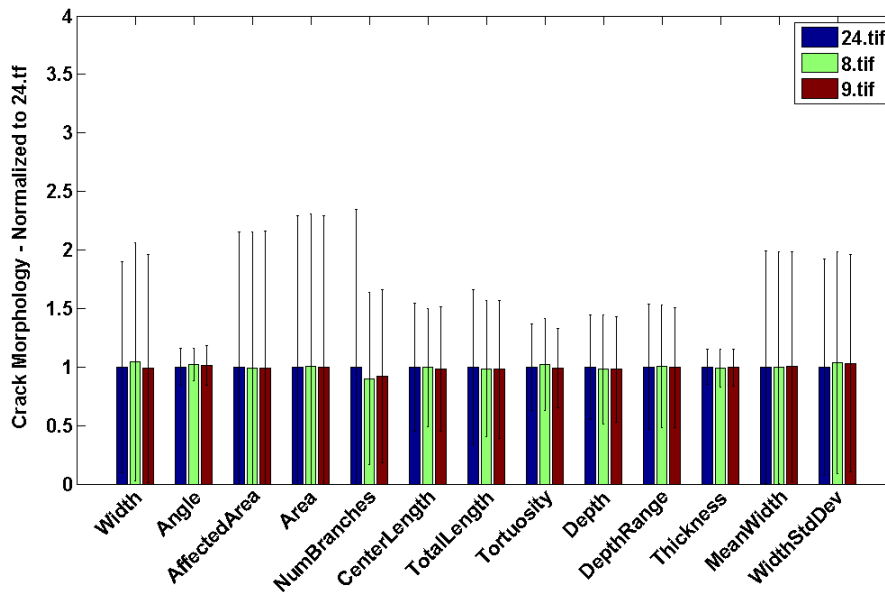


Figure 23. Intra-operator consistency on first repeated image. No statistically significant ($p < 0.05$) differences were found.

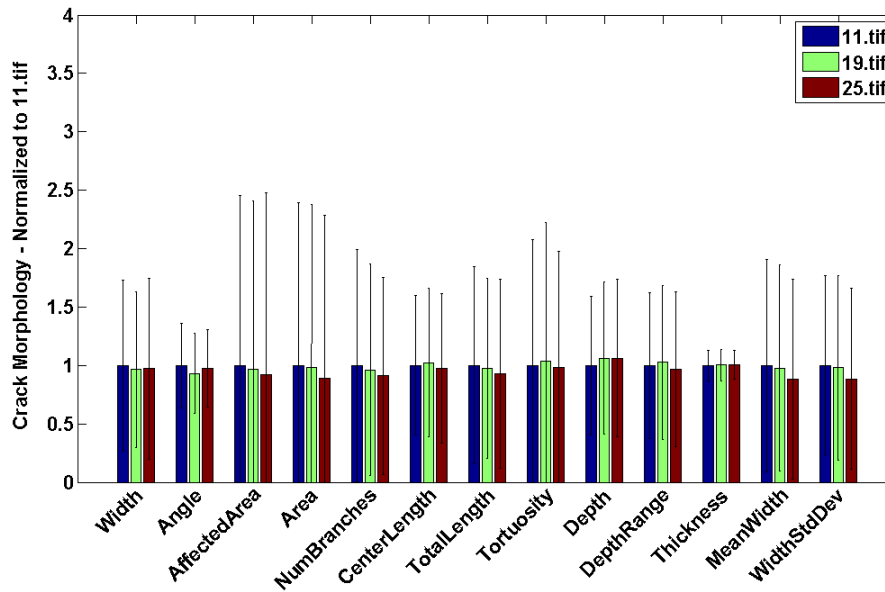


Figure 24. Intra-operator consistency on second repeated image. Again, no statistically significant ($p < 0.05$) differences were found.

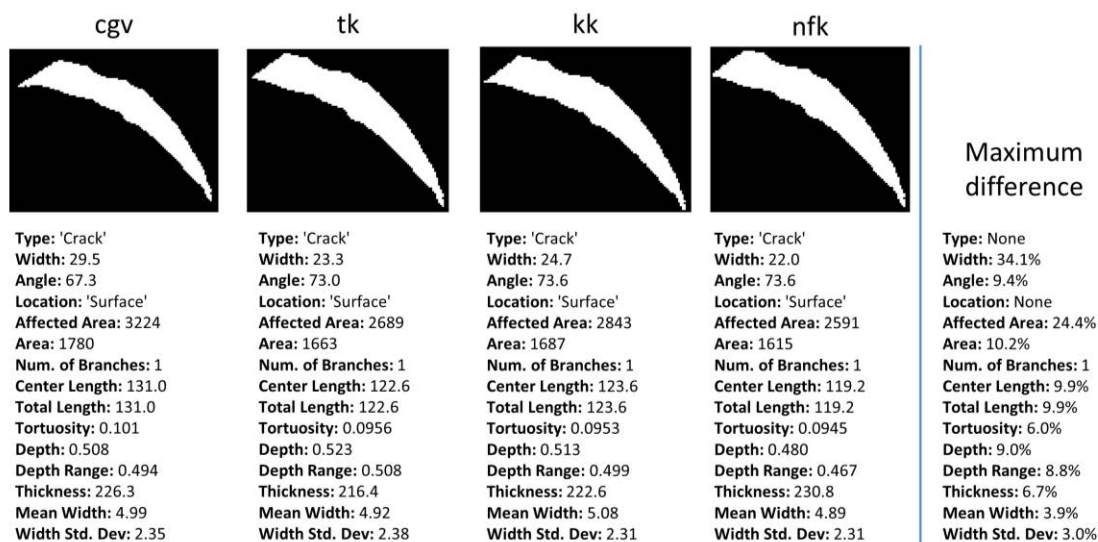


Figure 25. A comparison of one crack as analyzed by four different analysts.

Results

A total of 512 histology slides, representing 127 rabbit knees, were analyzed using the crack morphology program. In addition to the crack population outputs, several 'Whole-Specimen' outputs were calculated. For each rabbit knee, the total number of cracks, total crack area, and total affected area of all cracks from all four slides were summed. In addition, the total analyzed area of cartilage was also summed, and each of the three preceding values was divided by the analyzed area, to provide a sense of the proportional amount of joint damage, in terms of crack density, crack area percentage, and affected area percentage.

Figures 26 and 27 show that neither the individual crack morphology parameters nor the whole-specimen values changed significantly between the 8 week and 16 week time-points. This implies that the structural damage seen in this set of histology slides occurred relatively acutely, with no significant progression of damage between 8 weeks and 16 weeks. Of course, this observation is slightly limited, as the 16 week specimens were obviously different rabbits than the 8 week specimens, so the progression within a

single rabbit cannot be commented upon. Nonetheless, the clear lack of differences between the groups in Figures 26 and 27, given high statistical power (8 week $n = 450$ cracks; 16 week $n = 516$ cracks), strongly suggests arrested crack development within this timeframe. The data presented here for simplicity pools all OA models, although multi-way ANOVAs accounting for interactions similarly found no difference in crack morphology based on time-point. Based on these results, time-point was removed as a factor in the remaining analyses.

Figure 28 shows the effect of ACL transection on the resulting crack morphology. Very little difference was seen between the crack populations from the control set and the 50% and 100% ACL transection groups. A slight increase in depth was observed as the degree of transection was increased, with statistical significance reached between the control and 100% ACL transection groups. At the specimen level, the trends shown in Figure 29 indicate an increased number of cracks and area of cracks with increased ACL transection, although only the number of cracks in the 100% transection group was significantly different from the control group. These results suggest that instability induced by ACL transection did moderately increase the total amount of structural damage seen in cartilage, although the resulting cracks were fairly similar to those incurred during normal wear and tear.

Osteochondral defects had a much larger effect on the resultant structural damage. (Figure 30). Larger osteochondral defects generally resulted in cracks that were deeper, wider, and longer than those formed in control specimens, or from smaller osteochondral defects. There appears to be a threshold effect at 2 mm osteochondral defects, where the crack areas became much larger, and other parameters such as depth and mean width became statistically significant. Only a few statistically significant differences involving the 3 mm osteochondral defects were seen, due to the high standard deviations and the low number of samples (47 cracks from 3 rabbits, versus 209 cracks from 29 rabbits for the 2 mm osteochondral defects).

Figure 31 shows that the threshold effect for the 2 mm osteochondral defect was even more pronounced at the whole-specimen level. There was a dramatic, 20-fold increase in total cracked area and total affected area in the 2 mm defect specimens versus the control specimens. Statistical significance exists for the difference between the 2 mm defect and control specimens for all output parameters. Again, the 3 mm defect specimens did not quite reach statistical significance, due to the dispersion of the data and the low number of specimens.

Finally, a group of 19 rabbits was subjected to both a 50% ACL transection and a 2 mm defect, to determine any synergistic effects that might have occurred as a result of combining instability with acute damage. Figures 32 and 33 demonstrate that there were no significant differences between the 2 mm defect model and the combined model. This is not unexpected, as the 50% ACL model did not have any significant difference from the control set.

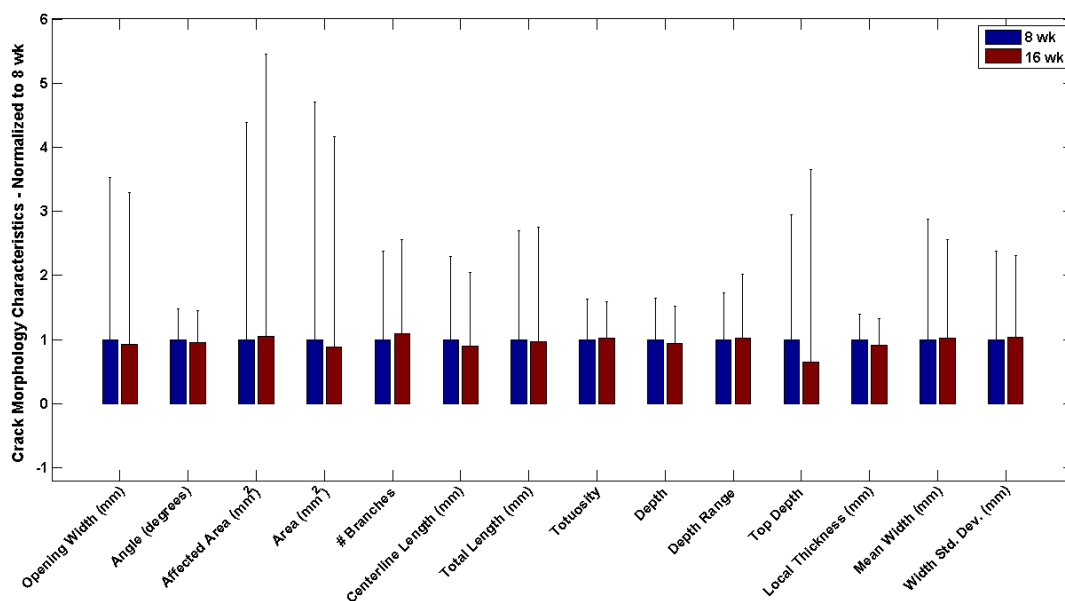


Figure 26. Crack morphology characteristics between 8 week and 16 week specimens. No significant differences were found.

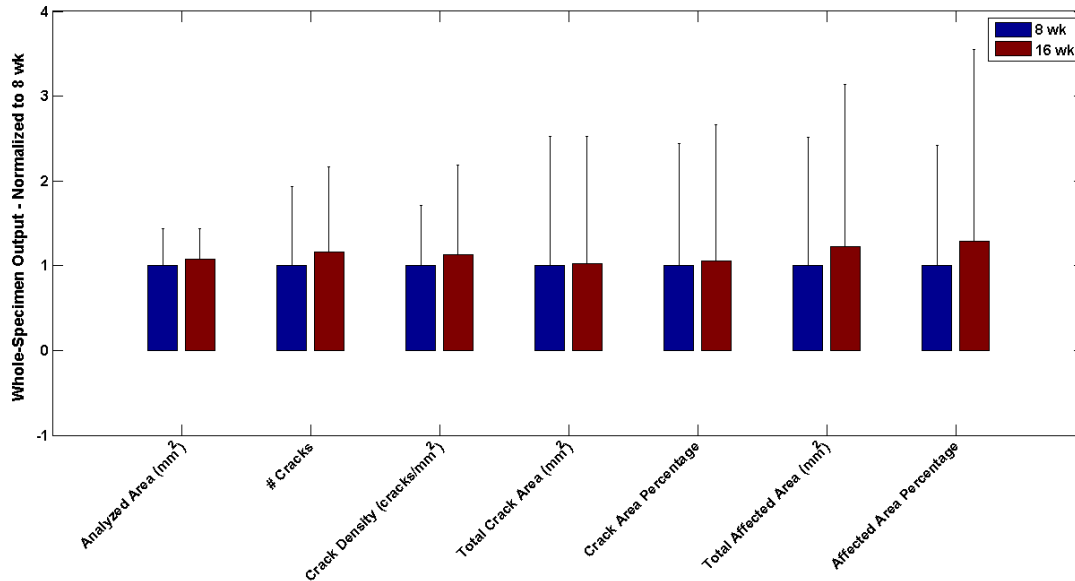


Figure 27. Specimen-level crack characteristics between 8 week and 16 week specimens. No significant differences were found. Dispersion bars are standard deviations.

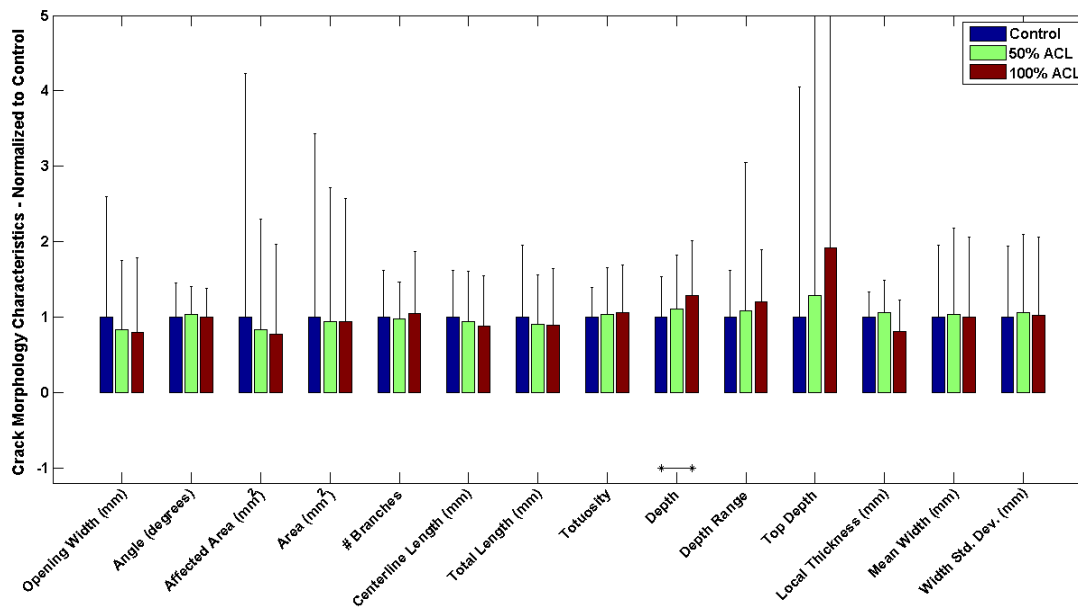


Figure 28. Crack morphology characteristics among control and ACL transaction specimens. Horizontal bars indicate statistical significance ($p < 0.05$). Dispersion bars are standard deviations.

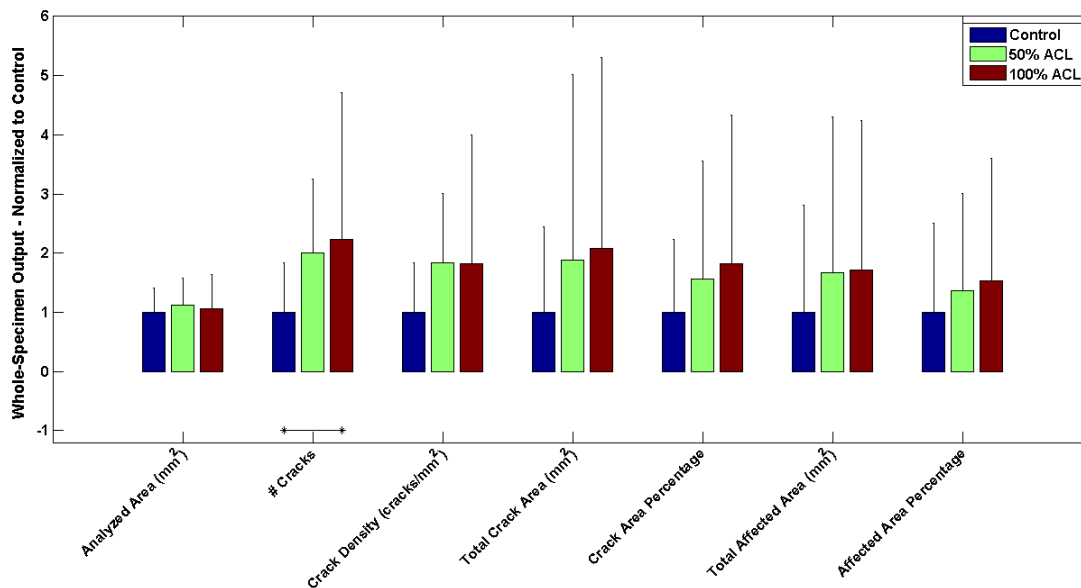


Figure 29. Specimen-level crack characteristics among differing levels of ACL transection. Horizontal bars indicate statistical significance ($p < 0.05$). Dispersion bars are standard deviations.

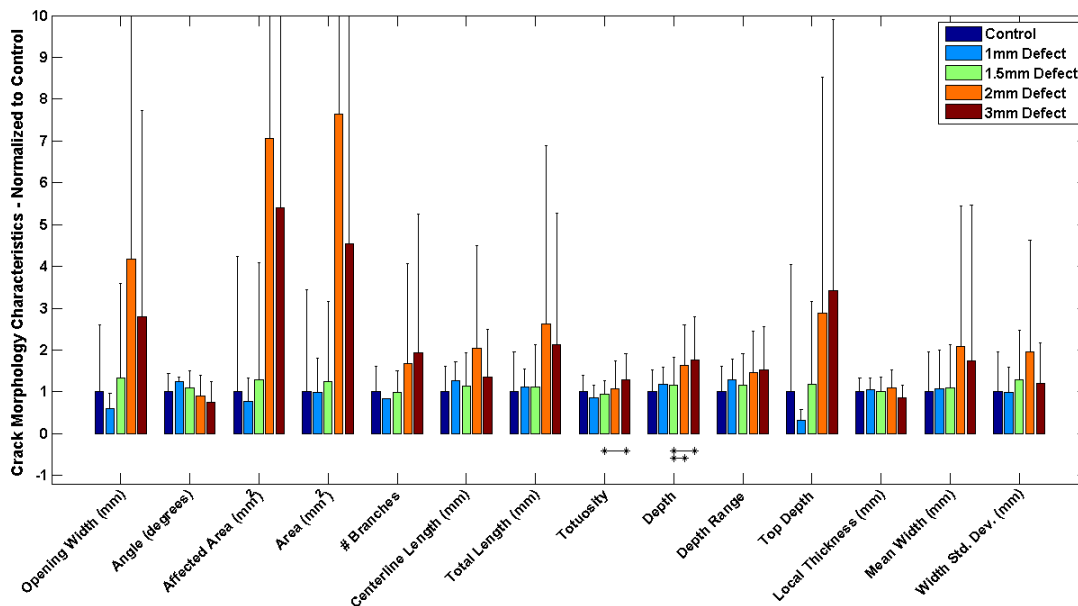


Figure 30. Crack morphology characteristics among control and osteochondral defect specimens. Horizontal bars indicate statistical significance ($p < 0.05$). Dispersion bars are standard deviations.

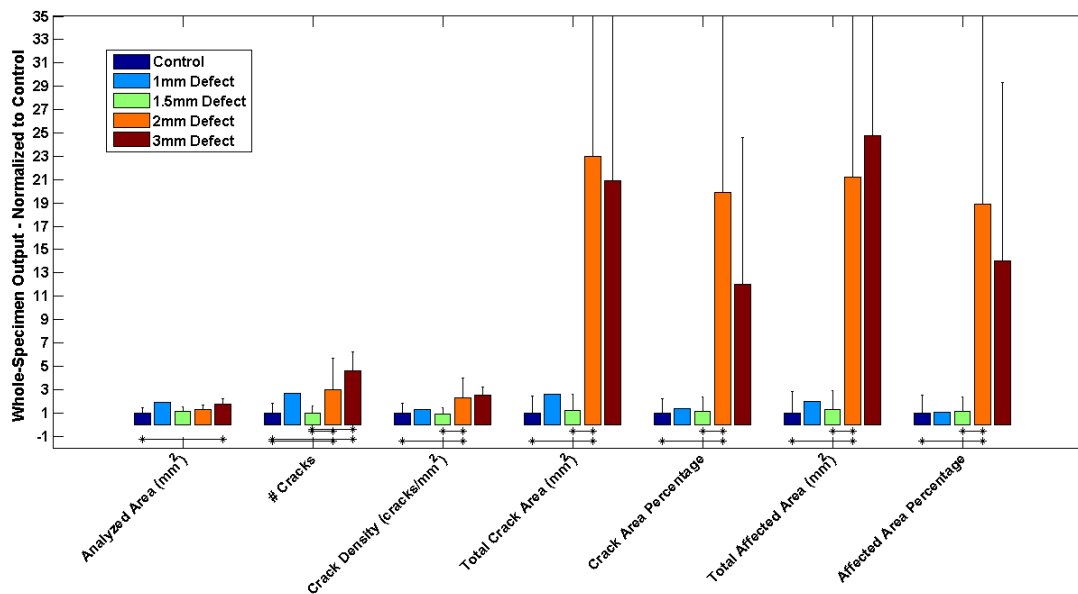


Figure 31. Specimen-level crack characteristics among differing sizes of osteochondral defects. Horizontal bars indicate statistical significance ($p < 0.05$). Dispersion bars are standard deviations.

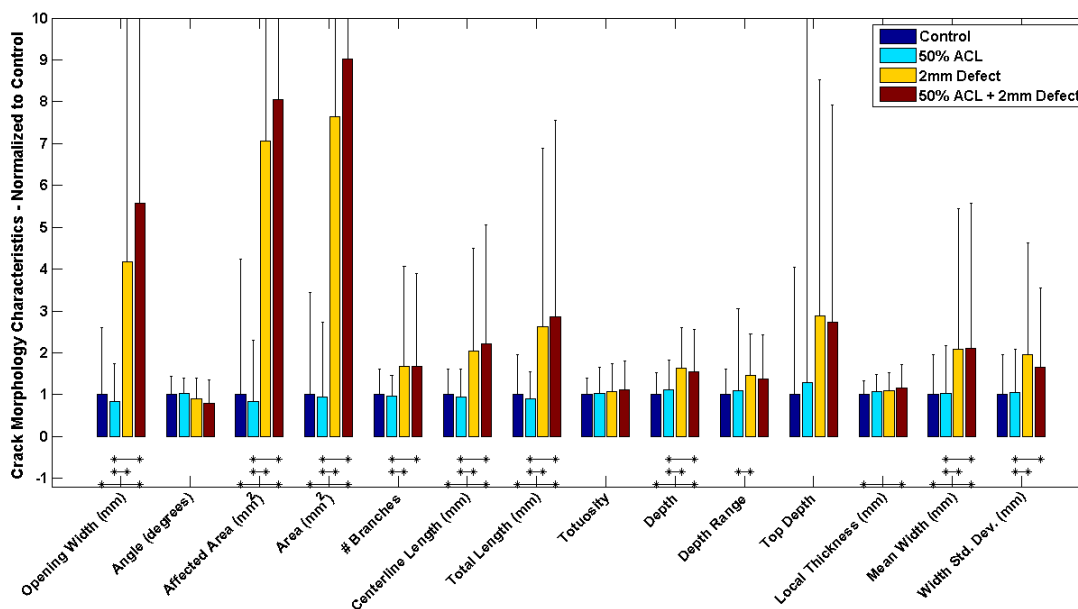


Figure 32. Crack morphology characteristics among control, ACL transection, osteochondral defect, and combined specimens. Horizontal bars indicate statistical significance ($p < 0.05$). Dispersion bars are standard deviations.

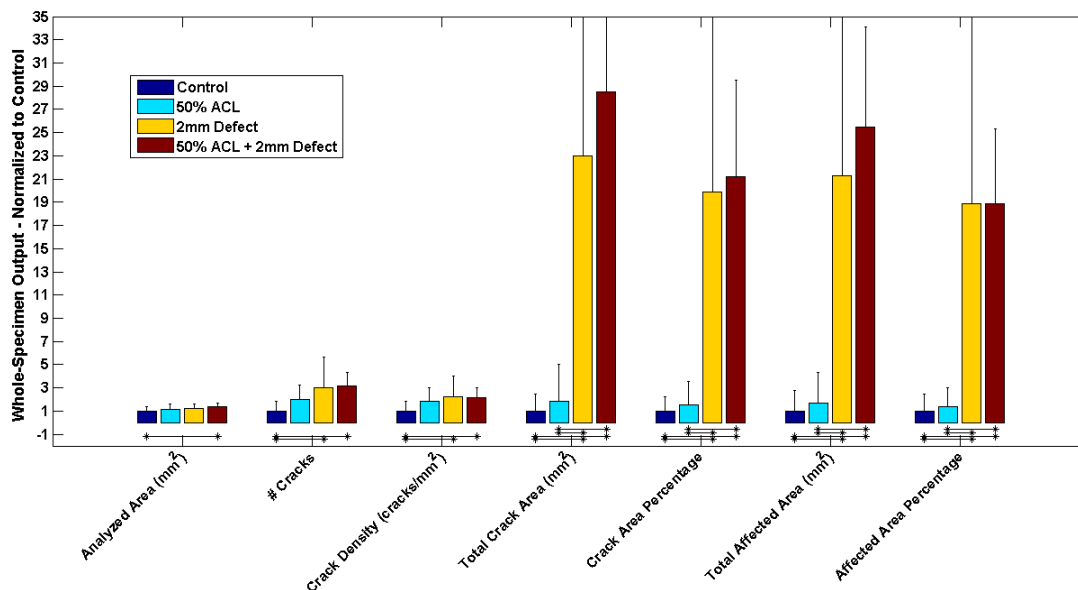


Figure 33. Specimen-level crack characteristics among control, ACL transection, osteochondral defect, and combined models. Horizontal bars indicate statistical significance ($p < 0.05$). Dispersion bars are standard deviations.

The preceding discussion has focused on the numerical measurements of crack geometry. The categorical attributes of crack type and crack location were also analyzed. Figures 34 and 35 show the percentage of defect-type cracks and the percentage of subsurface cracks under the various ACL transection and osteochondral defect characteristics as well as in the combined model. Although differences are seen, cross-tabulation and chi-squared tests revealed no statistically significant ($p < 0.05$) difference in categorical output among the various PTOA models. In all cases, only a minority of cracks were defect-type or subsurface. There were trends toward increasing number of subsurface cracks with larger defects and more defect-type cracks in the combined model, although statistical significance was not reached. Again, this suggests that synergistic effects in the combined model were minimal.

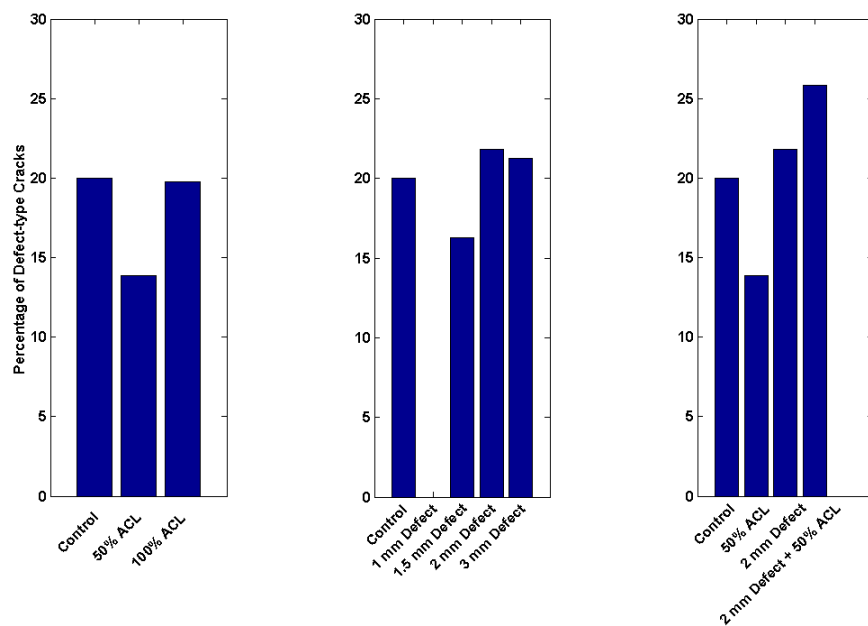


Figure 34. Effect of injury model on crack type. No differences were statistically significant ($p < 0.05$).

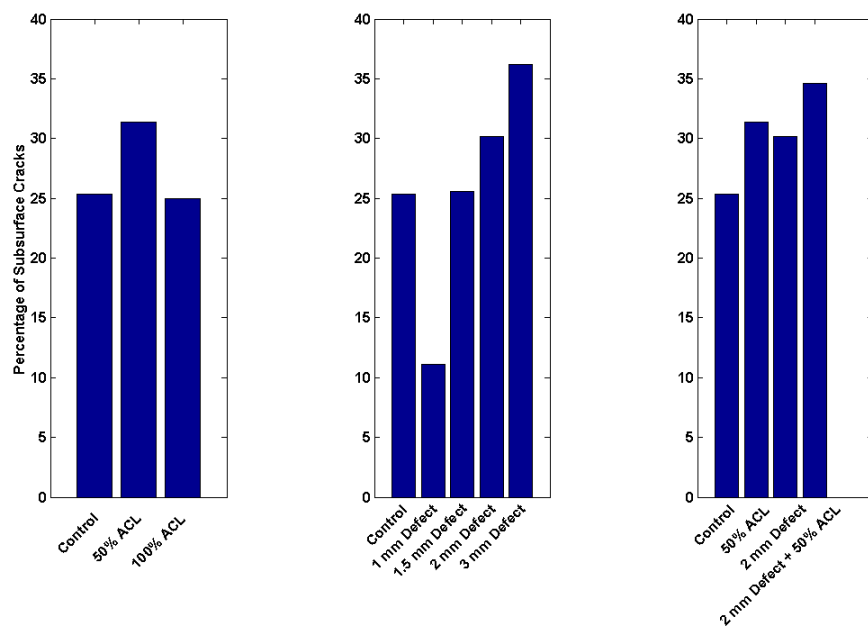


Figure 35. Effect of injury model on subsurface cracks. No differences were statistically significant ($p < 0.05$).

CHAPTER 4. CARTILAGE INDENTATION AND DEGRADATION

Changes of poroelastic (or biphasic) material properties of cartilage are recognized indicators of cartilage degeneration and osteoarthritis onset. In a poroelastic material, the total stress at any point can be written as

$$\sigma = \sigma_e - \nu \cdot I, \quad (4.1)$$

where σ is the total stress tensor, p is the pore fluid pressure, I is an identity matrix, and σ_e is the effective stress in the solid matrix. A two-dimensional element illustrating this stress state is shown in Figure 36.

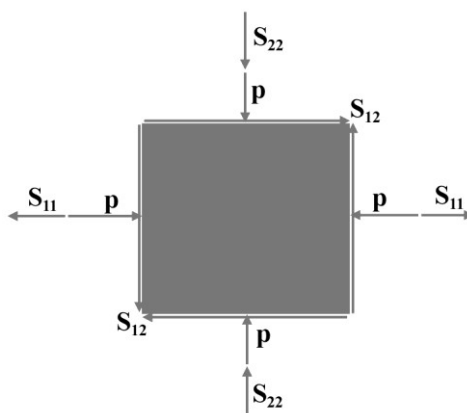


Figure 36. Element showing combination of fluid pressures ('p') and solid matrix stresses (' S_{ij} ') acting on each material point in poroelastic and biphasic formulations.

The total stress at any point depends on the stress due to deformation of the solid matrix, plus a hydrostatic fluid pressure. The pressure is subtracted in Equation 4.1 to account for the sign convention that fluid pressure is typically given as positive in compression, whereas stress tensors are positive in tension. The earliest poroelastic material models defined the solid matrix stress as proportional to strain, using the familiar

Hooke's law for linear elastic materials. The equations of motion for the solid-fluid mixture are then

$$\nabla \sigma = \rho \ddot{u} \quad (4.2)$$

and

$$\phi \nabla p + \pi = \rho_f \ddot{u}_f, \quad (4.3)$$

where π is the diffusive drag between the solid and the fluid. The diffusive drag depends on the permeability, k , of the fluid and on the porosity of the mixture (that is, the percentage of the mixture which is fluid). Therefore, in its simplest form, a biphasic material is described by four properties: an elastic modulus and Poisson's ratio associated with the solid phase (or any other equivalent choice of elastic constants), and the permeability and porosity, to define the fluid phase interaction with the solid phase. The porosity of cartilage is morphologically around 80% [6], leaving the elastic modulus, Poisson's ratio, and permeability to be determined experimentally.

Early development of the poroelastic/biphasic material model for cartilage focused on an analytical solution to the problem of a step load applied to the surface of articular cartilage through a porous indenter. The solution to this problem is a complex procedure involving non-dimensionalization and multiple Laplace and Hankel transforms, detailed in Mak et al. [115]. Once the solution has been formulated, mechanical indentation tests are performed and a curve fitting procedure can be used to derive poroelastic material properties from the resultant displacement-vs-time curves [116].

The indentation procedure outlined above requires very specific testing apparatus to match the analytical solution, including porous indentors and loading equipment capable of delivering force as a step-load. More recently, advances in finite element modeling of poroelastic materials and increases in computational speed have allowed for a relaxation of those constraints. In order to assess the material property changes invoked

by the impacts, an algorithm using Abaqus and Matlab was developed to derive poroelastic cartilage properties from osteochondral specimens impacted *in vitro* and/or also subjected to repetitive loading.

Methods

Bovine osteochondral specimens were harvested and mounted on plates as described in Chapter 2. The plate allows precise registration of the specimen for indentation, impact, histology, and other analyses that may be performed. The cartilage was subjected to impacts or repetitive loading, with indentation performed at time points before, during, and after impactation and loading. For indentation, the plate holding the cartilage was mounted into the indenter shown in Figure 37. The stage on the indenter was motorized, allowing the mapping of spatial differences in the specimen, from the center of the impact (located at the center of the specimen) to points located 4 mm and 8 mm away from the impact center. As the impactor had a radius of 2.75 mm, both remote points were outside of the directly impacted area. The indenter had a non-porous spherical tip 3 mm in diameter. Following the application of a small tare load and subsequent equilibration, the indenter was displaced to 10% of the cartilage thickness in 0.25 seconds, and was then held for 500 seconds. The reaction force in the indenter was monitored through a transducer, and the resultant load vs. time curve was used for material property derivation.

A finite element model of the indentation, created in Abaqus and Matlab, was used to drive an optimization procedure, adjusting poroelastic material properties until the FE reaction force curve matched that from the experiment. In Abaqus, the indentation experiment was simulated as an axisymmetric model, shown in Figure 38.

The indenter was modeled as a rigid analytical surface. The nodes at the bottom of the cartilage were fixed and fluid drainage was precluded, representing the much stiffer and much less permeable subchondral plate. The perimeter of the cartilage

specimen was considered free-draining. A sealed-at-contact fluid boundary condition was enforced on the articular surface through Abaqus subroutines. Using the UMESHOTION subroutine to detect contact, and the FLOW subroutine to control the fluid velocity, the outward normal fluid velocity on the articular surface was set to depend on the local pore fluid pressure, such that

$$V_n = k_s \cdot P \quad \text{and} \quad k_s = \begin{cases} \gg k/L, & \text{where unloaded (unsealed)} \\ 0, & \text{where loaded (sealed)} \end{cases}, \quad (4.4)$$

where V_n is the outward normal fluid velocity, k_s is the surface permeability, L is a characteristic length of the underlying elements, and P is the pore fluid pressure. Setting k_s to a high value when unloaded enforces free-draining conditions, while setting k_s equal to 0 where loaded precludes fluid flow. Logarithmic node spacing was used in the radial direction, such that for a given average element edge length, the contact region had a finer mesh than the remote region. A mesh convergence study, shown in Figure 39, demonstrated that an average element edge length of 0.3 mm was sufficiently small.

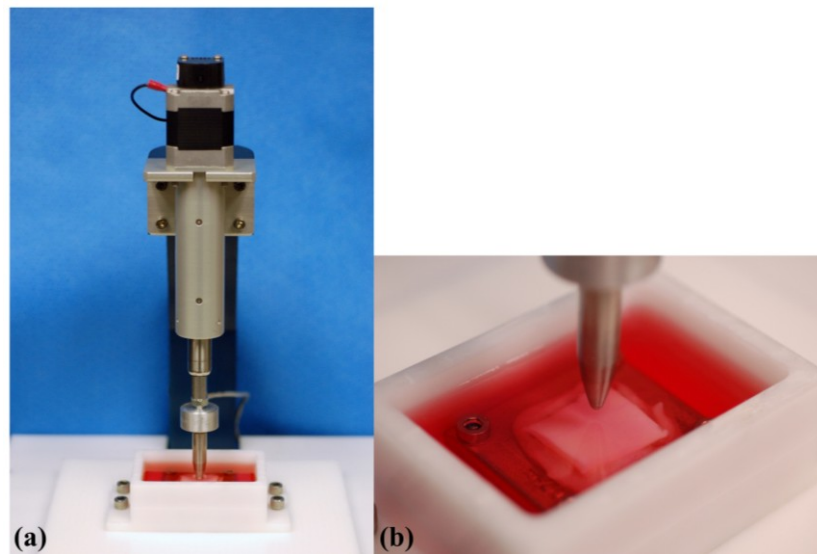


Figure 37. Mechanical indentation testing. (a) Indentor and (b) close-up of spherical indentation tip approaching cartilage osteochondral specimen.

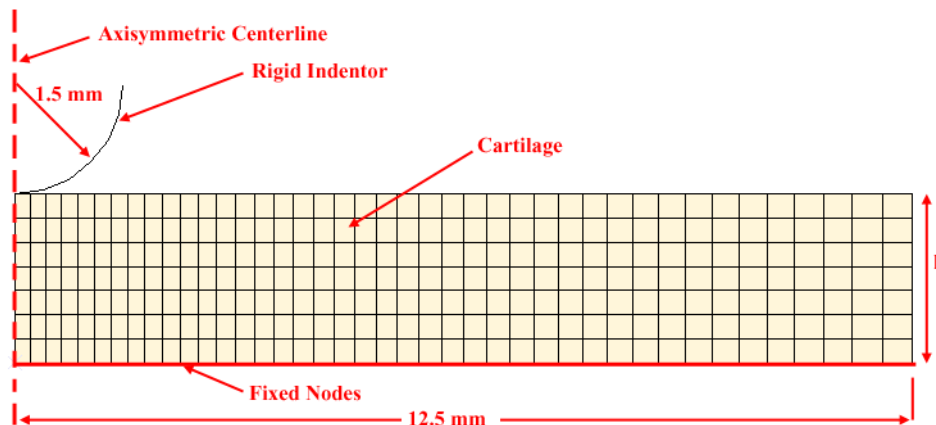


Figure 38. Axisymmetric finite element model of cartilage indentation.

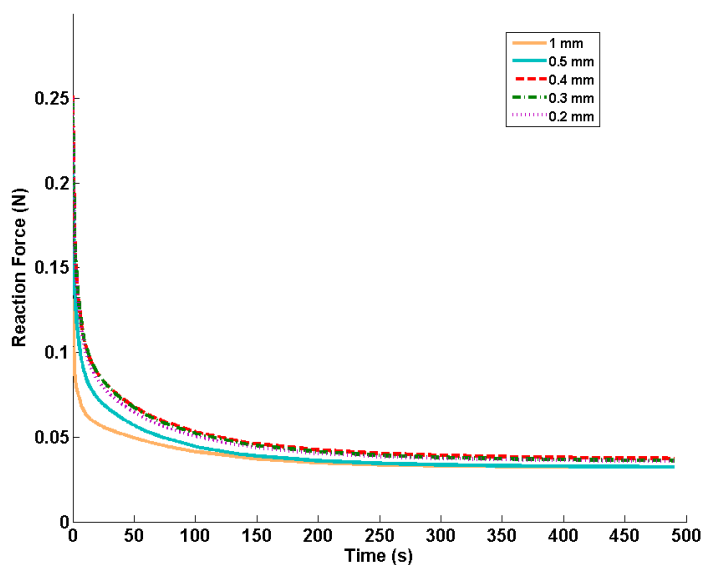


Figure 39. Convergence of the reaction force curve as the mesh resolution was increased.

The Matlab-driven optimization procedure is illustrated in Figure 40. The program *poroelasticProps* was the master optimization code, which included initial conditions and tolerances for the optimization procedure. This prompted the user to select the mechanical test result files, which include the reaction force curve and the

specimen thickness. The function *createMesh* was used to generate the finite element mesh, in the form of an Abaqus input file. The *lsqnonlin* function from Matlab's optimization toolbox was used to find a set of poroelastic material properties which minimized the error (between the computed vs. experimentally measured load versus time curve) returned by *evalMaterial*. The function *evalMaterial* was passed a set of material properties and the force relaxation curve from a mechanical indentation test. *evalMaterial* ran the Abaqus simulation and returned the error between the Abaqus force relaxation curve and the mechanical test. The Unix script *postProcess* extracted the force relaxation curve from text files output by Abaqus. Coincidentally, just as this phase of development was being completed, a technical report was published in the Journal of Biomechanics which detailed a nearly identical procedure [143].

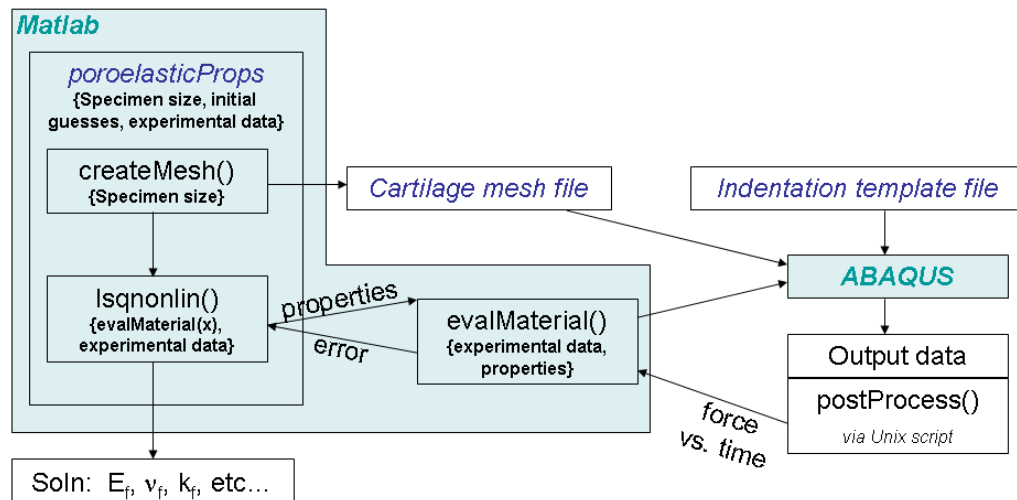


Figure 40. Optimization procedure for determination of cartilage properties from indentation results.

A visco-poroelastic material model similar in form to that shown to be effective by DiSilvestro and Suh [144, 145] was used for these tests. The viscoelastic relaxation

function g_R (both the shear and volumetric moduli were assumed to follow the same relaxation) was defined by a 3rd order Prony series expansion, such that

$$g_R(t) = 1 - \sum_{i=1}^3 g_i (1 - e^{-t/\tau_i}), \quad (4.5)$$

where g_i and t_i are material constants referred to as relaxation coefficients and time constants, respectively. Per DiSilvestro and Suh, all relaxation coefficients were set equal to g^* , and t_2 was set to logarithmic spacing between t_1 and t_3 , such that

$$2 \cdot \log t_2 = \log t_1 + \log t_3. \quad (4.6)$$

The Poisson's ratio was set to a low value of 0.05, representing the high compressibility of a drained cartilage matrix. Initial tests demonstrated that this five-parameter (E , k , g^* , t_1 , and t_2) model was very sensitive to the initial starting point, and that multiple combinations of property values could achieve equal-quality fits to the experimental data. An additional set of mechanical indentations were therefore performed, varying the ramp speed from 0.1 s to 30 s, from which it was apparent that values of t_1 less than 1 s resulted in a more accurate cartilage representation. Further testing revealed that t_1 could be set to a constant value of 0.25 s and that t_3 could be set to a constant value of 80 s, without sacrificing the quality of the final fit. This resulted in a final material model with three material properties needing to be determined via optimization. In terms of physical interpretation, the equilibrium modulus (E) is responsible for the final stress at the end of the indentation test. The relaxation coefficient (g^*) primarily governed the peak force and dominated the initial relaxation behavior, for the first few seconds. The permeability (k) also governed the relaxation, becoming the dominant term after the solid phase viscoelastic effect had dissipated.

To further improve the uniqueness of the final material model and the speed of optimization, the optimization algorithm was modified to be a two-stage procedure. In the first stage, the equilibrium modulus was determined independently of the other

properties by setting the permeability very high, setting the relaxation coefficient to 0, and comparing only the last 50 seconds of the experimental and finite element curves. Once the equilibrium modulus was determined, the second stage of the algorithm ran the optimization algorithm to determine the permeability and relaxation coefficients. The two-stage approach was critical to achieving unique final material fits, regardless of the initial starting point (Table 1). The final material model and optimization procedure used resulted in excellent quality fits (Figure 41) in approximately 10 minutes. A folder of mechanical test files can be selected and the optimization algorithm would determine material properties for all the tests, with no additional user intervention.

		Final Material Properties		
	Start Point	Modulus (MPa)	Permeability ($\times 10^{-16} \text{ m}^4/(\text{N}\cdot\text{s})$)	Relaxation Coefficient
Specimen #1	1	0.268	42.24	0.156
	2	0.268	41.71	0.156
	3	0.267	41.30	0.157
	4	0.267	40.95	0.156
Specimen #2	1	0.390	20.14	0.190
	2	0.388	19.36	0.190
	3	0.389	19.55	0.190
	4	0.390	20.06	0.190
Specimen #3	1	0.312	22.06	0.277
	2	0.309	21.66	0.277
	3	0.310	21.73	0.277
	4	0.312	21.78	0.277
Specimen #4	1	0.367	17.97	0.134
	2	0.368	18.03	0.134
	3	0.366	17.29	0.135
	4	0.363	16.01	0.134

Start Points (Modulus, Permeability, Relaxation Coefficient):

- 1: 0.7 MPa, $10 \times 10^{-16} \text{ m}^4/(\text{N}\cdot\text{s})$, 0.15
- 2: 1.4 MPa, $20 \times 10^{-16} \text{ m}^4/(\text{N}\cdot\text{s})$, 0.5
- 3: 2 MPa, $15 \times 10^{-16} \text{ m}^4/(\text{N}\cdot\text{s})$, 0.7
- 4: 0.33 MPa, $25 \times 10^{-16} \text{ m}^4/(\text{N}\cdot\text{s})$, 0.18

Table 1. Insensitivity of the indentation material property optimization algorithm to varying start points.

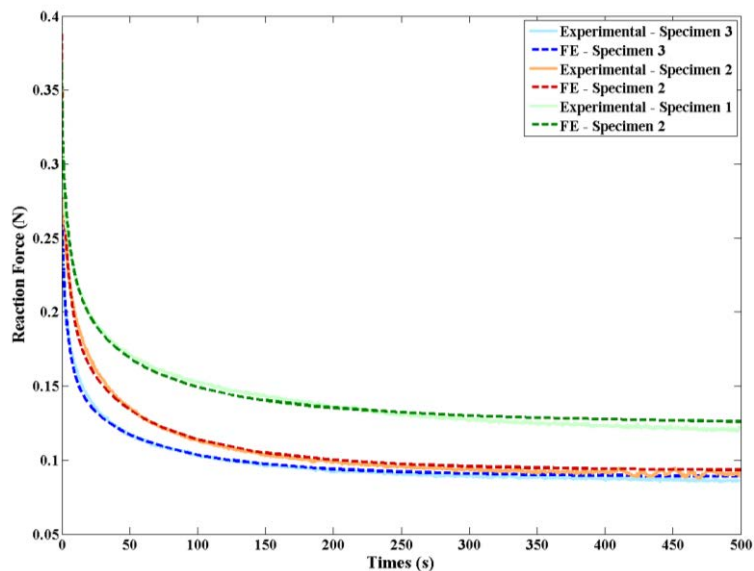


Figure 41. Examples of fit between experimental results (solid lines) and optimized finite element results (dashed lines).

Results

Impact and indentation testing was performed to determine the spatial and temporal progression of cartilage degradation following cartilage impact or repetitive loading. Figure 42 shows the relative change in cartilage thickness, equilibrium modulus, permeability, and relaxation coefficient following impact. All material properties are normalized to their same-specimen/same-location pre-impact value. The normalized values are shown in tabular form in Table 2. Figure 43 shows material property changes for a small ($n = 6$) set of unimpacted control specimens.

It is immediately clear from Figure 42 that the mechanical property changes occurred nearly exclusively within the impact zone (Location = 0 mm). While slight deviations from pre-impact values occurred 24 hours after impact at the 4 mm and 8 mm locations, these deviations resolved within one week and there was no indication of the degeneration “spreading” from the impact site. Cartilage thickness was unchanged throughout the experiments. Although a depression from the impact could be

(qualitatively) seen immediately after the impact (Figure 44), by the time of the 2-hour post-impact measurement there was no distinguishable change in thickness.

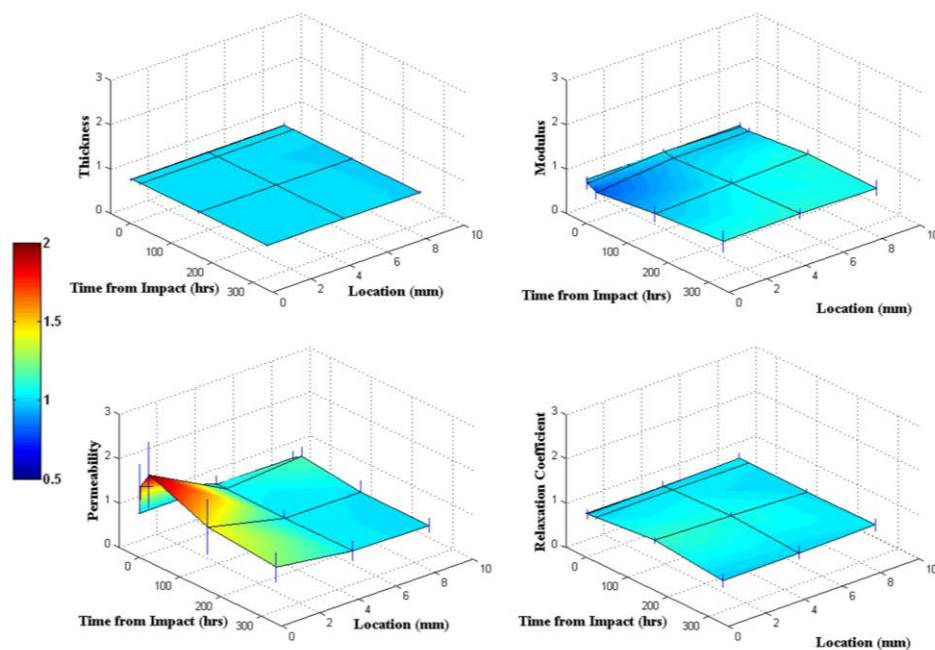


Figure 42. Normalized properties following impact with 2.18 J/cm^2 . Error bars show standard deviations.

Distance From Impact Center			
Thickness	0 mm	4 mm	8 mm
0	1 (0)	1 (0)	1 (0)
2	0.996 (0.024)	1.004 (0.021)	1.006 (0.046)
24	1.003 (0.035)	0.999 (0.007)	0.998 (0.02)
168	1.005 (0.028)	1.011 (0.029)	0.983 (0.038)
336	0.995 (0.025)	1.002 (0.017)	0.986 (0.022)

Distance From Impact Center			
Modulus	0 mm	4 mm	8 mm
0	1 (0)	1 (0)	1 (0)
2	0.917 (0.138)	1.018 (0.051)	0.967 (0.093)
24	0.806 (0.14)	0.966 (0.047)	0.971 (0.069)
168	0.96 (0.168)	1.042 (0.105)	1.099 (0.093)
336	1.09 (0.245)	1.106 (0.111)	1.078 (0.177)

Distance From Impact Center			
Permeability	0 mm	4 mm	8 mm
0	1 (0)	1 (0)	1 (0)
2	1.606 (0.494)	1.05 (0.194)	1.037 (0.148)
24	1.97 (0.735)	1.051 (0.042)	1.175 (0.197)
168	1.437 (0.619)	1.029 (0.155)	1.011 (0.25)
336	1.274 (0.323)	1.031 (0.224)	1.001 (0.158)

Distance From Impact Center			
Relaxation Coefficient	0 mm	4 mm	8 mm
0	1 (0)	1 (0)	1 (0)
2	0.98 (0.105)	1.001 (0.105)	1.03 (0.105)
24	1.006 (0.028)	1.02 (0.028)	1.016 (0.028)
168	1.131 (0.066)	1.086 (0.066)	1.008 (0.066)
336	0.971 (0.143)	0.996 (0.143)	1.013 (0.143)

Table 2. Normalized properties following impact with 2.18 J/cm^2 with standard deviations shown in parenthesis.

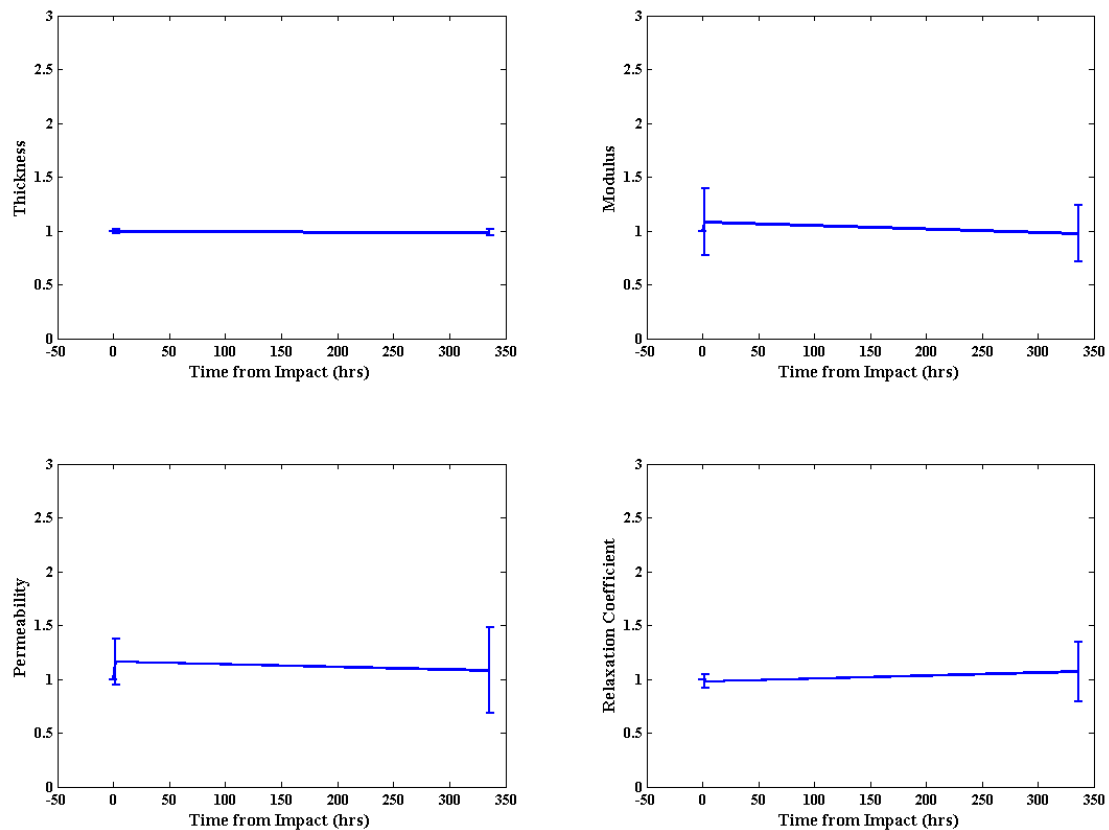


Figure 43. Normalized material properties at explant center in unimpacted control specimens. Vertical bars show standard deviations. No differences in material properties were statistically significant ($p < 0.05$).

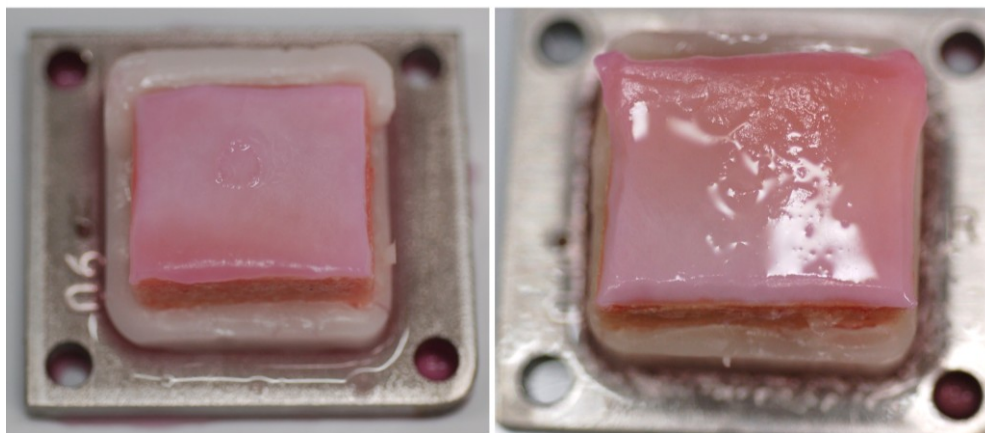


Figure 44. Typical examples of osteochondral specimens with depressed impacted region immediately after impact.

Figure 45 highlights the change in material properties at the impact center. An unexpected effect was found, with both modulus and permeability changing substantially within the first 24 hours, but then returning to nearly pre-impact values by 2 weeks. These results are somewhat surprising because the property change happens too quickly to be caused by altered chondrocyte biosynthesis and changes in material composition. Yet the recovery suggests that the property changes are not the result of frank tissue failure (to the author's knowledge, there is no reported evidence of cartilage cracks being healed). These results suggest a significant role of biochemical or electrochemical effects such as fixed charge density and osmolarity in material property changes, or a weakening, without failure, of collagen fibrils.

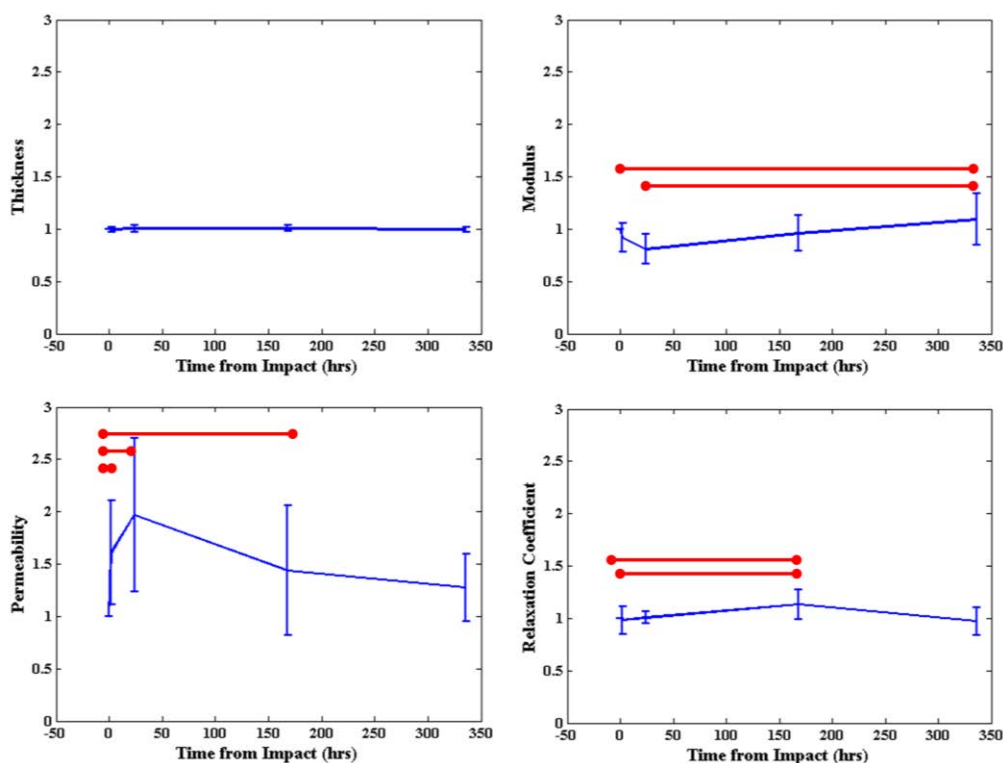


Figure 45. Normalized material properties at impact center. Vertical bars show standard deviations. Statistically significant differences ($p < 0.05$) are shown with horizontal bars.

Despite all impacts in the above set having the same delivered energy, there were difference in impact characteristics, due to differences in pre-impact material properties and cartilage thickness. Impacts were characterized in terms of maximum (nominal) stress, maximum stress rate of change, and high-frequency content. High frequency content was determined by performing a Fast Fourier Transform on the impact force trace, and calculating the percentage of the total signal that was above 2 KHz (a resonant peak around 5 KHz was filtered out). High frequency content is thought to be indicative of cartilage fracture. Correlating these impact properties to changes in material properties provided an opportunity to investigate the sensitivity of cartilage to impact severity. Focusing first on the impact characteristics, maximum stress and maximum stress rate of change were highly correlated to each other, and both depended on the cartilage thickness, with thinner cartilage resulting in higher stress and stress rates of change (Table 3). High frequency content, on the other hand, did not appear to correlate with any of the other metrics. The relationship between impact characteristics and thickness is plotted in Figure 46.

Correlation Coefficient	Max Stress	Max Stress Rate	High Freq. Content	Abs. Thickness
Max Stress	1	0.945291282	0.119287779	-0.767198284
Max Stress Rate	0.945291282	1	0.29973439	-0.794397422
High Freq. Content	0.119287779	0.29973439	1	-0.164142637
Abs. Thickness	-0.767198284	-0.794397422	-0.164142637	1
p-value	Max Stress	Max Stress Rate	High Freq. Content	Abs. Thickness
Max Stress	1	1.14599E-13	0.553428781	3.03022E-06
Max Stress Rate	1.14599E-13	1	0.128778158	7.52412E-07
High Freq. Content	0.553428781	0.128778158	1	0.413287221
Abs. Thickness	3.03022E-06	7.52412E-07	0.413287221	1

Note: Yellow highlights indicate statistical significance at a level of $p < 0.05$.

Table 3. Correlation of impact characteristics with cartilage thickness.

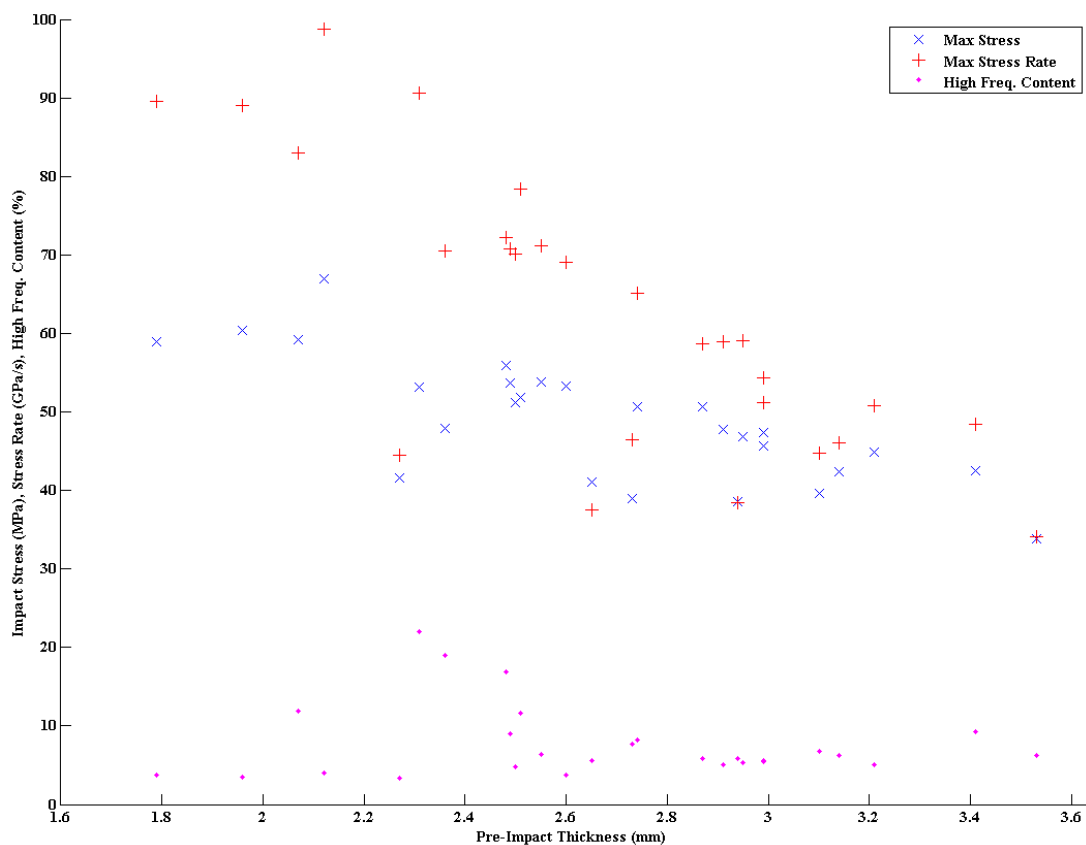


Figure 46. Effect of pre-impact cartilage thickness on resultant impact characteristics.

Table 4 shows the correlation of impact characteristics with material property changes at 1 week post-impact. (At this point in the project, there were not enough specimens with full impact and material property data at the one-day time-point to perform statistical correlation.) All impact characteristics significantly affected the change in permeability, while only stress rate of change and high-frequency content correlated with the change in modulus. The relaxation coefficient was not significantly affected by any impact characteristic. Figure 47 shows the dependences of material property change on maximum stress and stress rate of change.

Correlation Coefficient	Thickness	E	k	g
Max Stress	-0.336606393	-0.503967833	0.706495048	-0.459824191
Max Stress Rate	-0.700508811	-0.691112569	0.857406298	-0.268729228
High Freq. Content	-0.844637459	-0.764059466	0.65182037	0.089060463
Thickness	1	0.659956488	-0.784401403	-0.16969524
E	0.659956488	1	-0.687281956	0.047938957
k	-0.784401403	-0.687281956	1	-0.230830763
g	-0.16969524	0.047938957	-0.230830763	1
p-value	Thickness	E	k	g
Max Stress	0.311453168	0.11396287	0.015082632	0.154736193
Max Stress Rate	0.016359032	0.018516185	0.000740894	0.424272686
High Freq. Content	0.001068952	0.006187113	0.029770084	0.794555979
Thickness	1	0.02712441	0.00425681	0.617903478
E	0.02712441	1	0.019451334	0.888686801
k	0.00425681	0.019451334	1	0.49467581
g	0.617903478	0.888686801	0.49467581	1

Note: Yellow highlights indicate statistical significance at a level of $p < 0.05$.

Table 4. Correlation of material property changes at one week with impact characteristics.

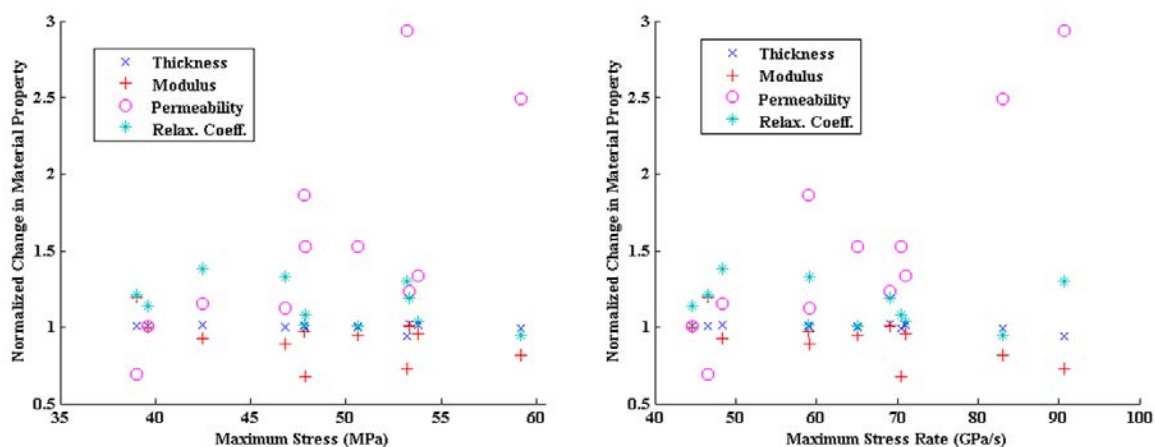


Figure 47. Change in material properties at one week versus maximum impact stress and stress rate of change.

An additional potential impact characterization comes from Burgin and Aspden, who calculated a “coefficient of energetic restitution” (CoER) [29]. Their CoER is the ratio of the energy returned in the rebound to the energy expended compressing the cartilage (Figure 48). It is also possible to calculate the energy dissipated as the difference between the compression energy and the returned (rebound) energy. Since all impacts in the set currently being discussed involved the same impact energy, CoER and energy dissipated were essentially identical metrics, although they will become different in later sections that discuss impacts at differing energy levels. (As a side note, it is worth noting that in every impact trace, the compression energy calculated from the force-displacement curve was within 0.1 mJ of the potential energy calculated from the mass and drop height, indicating a well-designed apparatus in which all energy was delivered to the cartilage.)

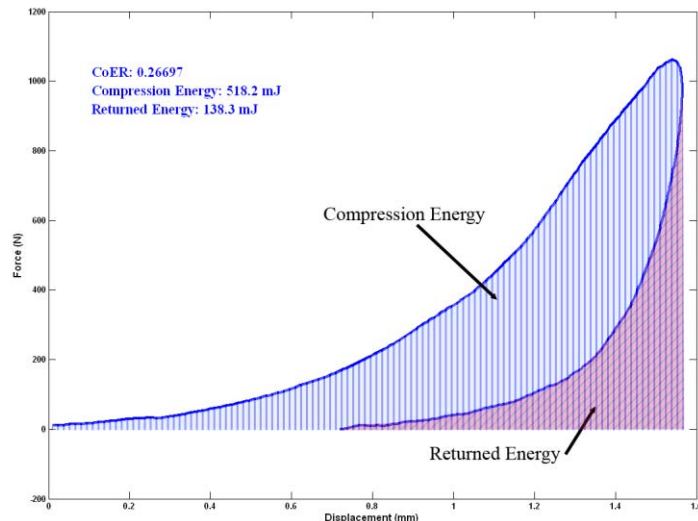


Figure 48. Illustration of coefficient of restitution.

Energy dissipated (or CoER) turned out not to have statistically significant correlation with changes in material properties at any timepoint. However, the timepoint

with the greatest changes in material properties (24 hours post-impact) had only six specimens. At this timepoint, a trend toward increasing permeability and decreasing modulus with increasing energy dissipated is seen (Figure 49). With p-values of 0.137 and 0.059 for the modulus and permeability, respectively, it seems likely that these trends could become significant with a larger sample size.

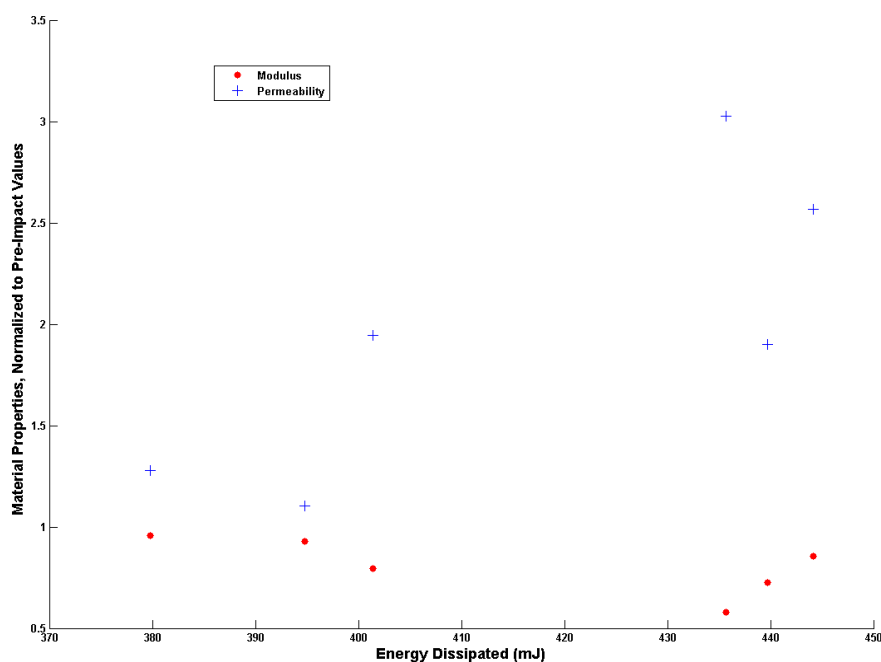


Figure 49. Change in material properties at 1 day post-impact versus the impact energy absorbed.

A separate series of impacts involved replacing the rigid metal impactor with an osteochondral plug, creating a cartilage-on-cartilage impact that may be more representative of physiologic impact conditions. This series involved both cartilage-on-cartilage and metal-on-cartilage impacts of 3.09 J/cm^2 (higher than the previously discussed metal-on-cartilage impacts of 2.18 J/cm^2). As shown in Figure 50, the cartilage-on-cartilage impacts had minimal influence on material properties, although a

slight, non-statistically significant increase in permeability and decrease in modulus was seen immediately after impact. At the time of this writing, only 6 specimens had been subjected to cartilage-on-cartilage impact and 10 specimens had been subjected to 3.09 J/cm² metal-on-cartilage impact. The 3.09 J/cm² metal-on-cartilage impacts resulted in a familiar trend of increased permeability, which decreased by 2 weeks. However the modulus was reduced both immediately post-impact and at 2 weeks (Figure 51). The increased permeability immediately post-impact was the only property change with statistical significance in this set. The relaxation coefficient increased immediately post-impact and at 2 weeks post-impact, but the large standard deviation precluded statistical significance. Although there appeared to be some additional changes at the 4 mm and 8 mm locations, none of these reached statistical significance. It is worth noting that the increased modulus at 2 weeks (336 hours) at 8 mm from the impact center was highly influenced by a single outlier.

Figure 52 plots the time-course of material property changes at the impact center for all three series discussed. It is particularly interesting to compare the results from the 2.18 J/cm² and 3.09 J/cm² metal-on-cartilage impacts. The permeability changes for the two series were nearly identical for both the immediate and 2 week post-impact timepoints. However, the changes in equilibrium modulus and relaxation coefficient were much greater under the 3.09 J/cm² impact than under the 2.18 J/cm² impact, especially at 2 weeks post-impact. This suggests that there may have been a dose-dependent component in the solid-matrix response to impact, while the permeability was relatively insensitive to impact energy. It appears that the higher-energy 3.09 J/cm² impact created permanent damage in the solid matrix, while the 2.18 J/cm² impact caused repairable damage. Increasing the sample numbers for the higher-energy impact as well as adding additional time-points for that series would be critical steps toward formalizing these observations.

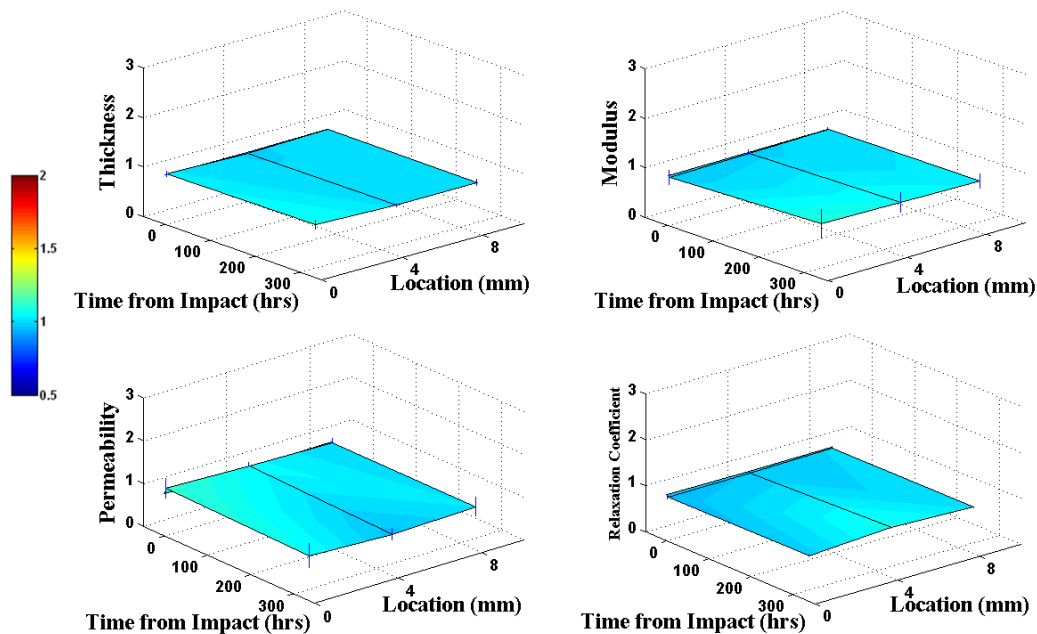


Figure 50. Normalized property surfaces from cartilage-on-cartilage impact of 3.09 J/cm^2 . Bars are standard deviations.

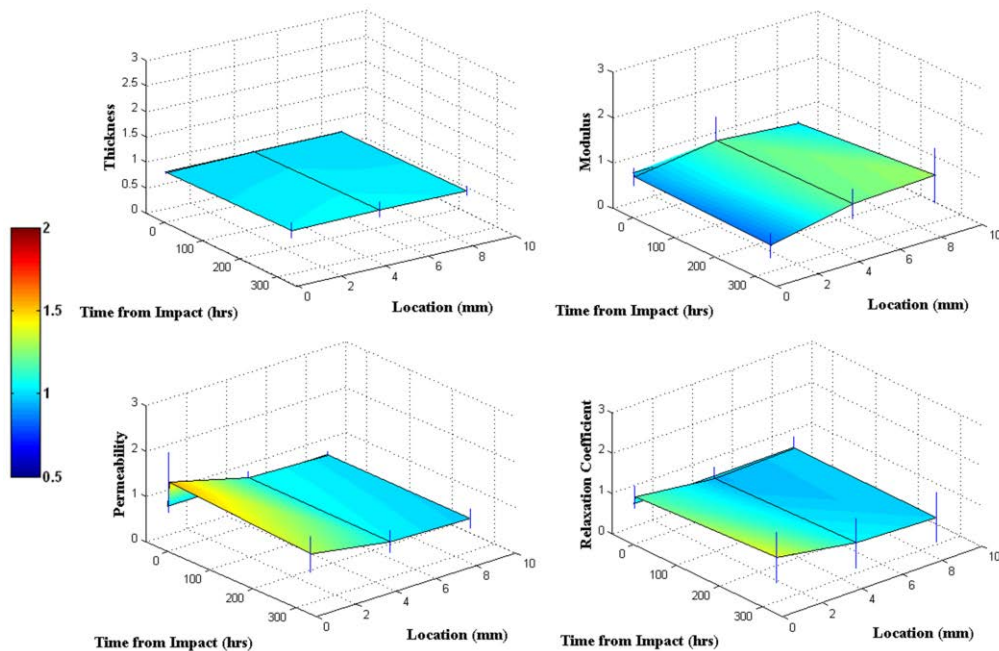


Figure 51. Normalized property surfaces from metal-on-cartilage impact of 3.09 J/cm^2 . Bars are standard deviations.

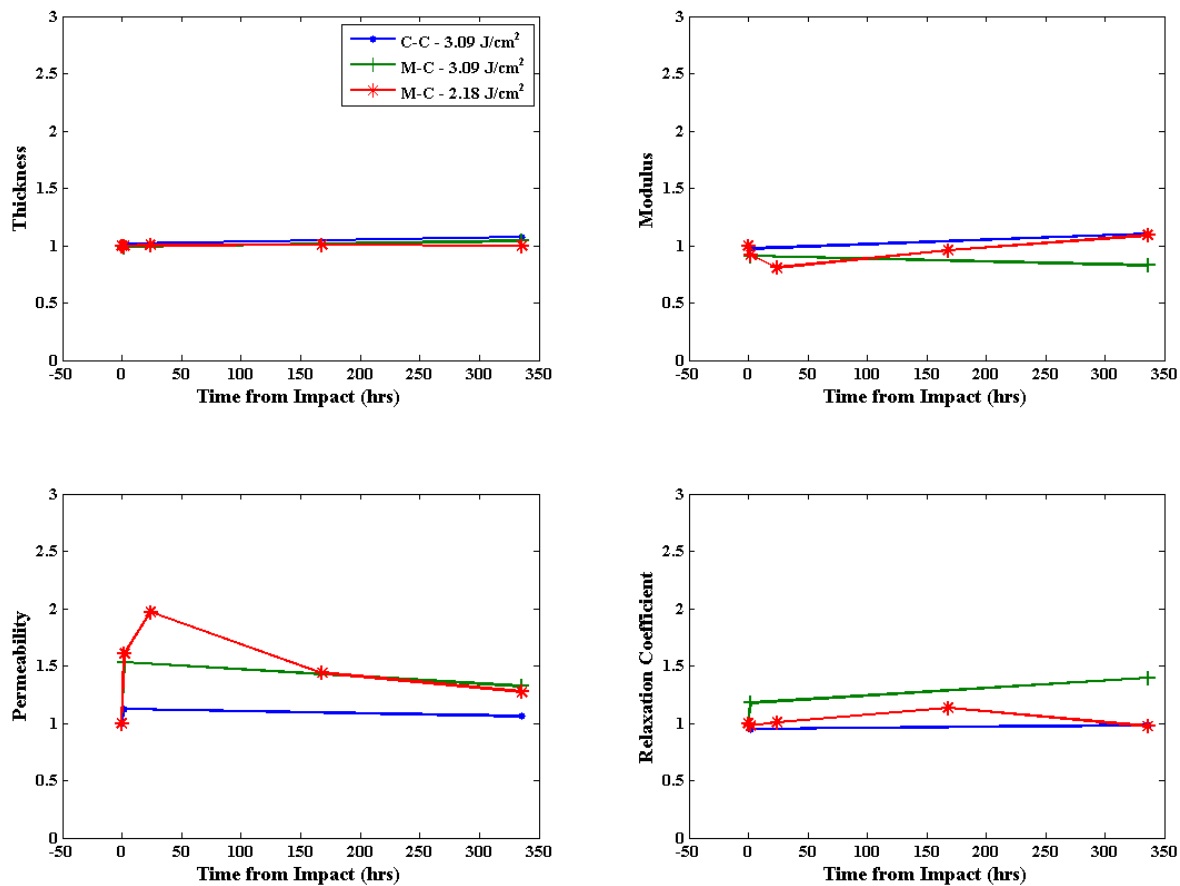


Figure 52. Changes in the material properties at impact center under three different loading conditions: 3.09 J/cm² cartilage-on-cartilage, 3.09 J/cm² metal-on-cartilage, and 2.18 J/cm² metal-on-cartilage.

CHAPTER 5. FINITE ELEMENT MODELING OF CARTILAGE CRACKS

As demonstrated in Chapter 2, cracks extending through a significant portion of the cartilage depth are a common feature in degenerating cartilage. That chapter discussed the importance of cartilage cracks as an indicator of the damage incurred in the cartilage matrix. Cracks may also play a direct, mechanical role in the propagation of cartilage degeneration. Repo and Finlay observed cell death concentrations around cartilage cracks [28], and Lewis et al. later reported similar findings [146]. It is likely that some of this damage occurs acutely, at the time of injury. However, the presence of a fissure may alter the local stress and strain environment, exposing chondrocytes within the immediate vicinity to deleterious loading and causing further injury. In this chapter, a physiologically-relevant cartilage material model was developed and applied in finite element models of cartilage cracks. A range of crack morphologies, based on the results of Chapter 2, were studied, to determine if any specific morphologic characteristics were more likely to result in damaging loads. Finally, a framework was developed to study mechanically-driven propagation of degeneration.

Development of a depth-dependent cartilage material model

Chapter 4 outlined the basic poroelastic material model and a modification to that model necessary to fully replicate the indentation experiment. Unfortunately, while indentation testing and the derived material properties are very useful tools in assessing osteoarthritis, the response of such a material model is not accurate under physiologic loads and load rates. In order to withstand higher loads, particularly in situations of unconfined compression, the effect of collagen fibril reinforcement has been incorporated into various poroelastic material models [119, 147, 148]. Furthermore, cartilage has a well-documented spatial heterogeneity, both across the articular surface and through the

cartilage depth. Generally speaking, the compressive and shear moduli increase through the cartilage thickness [149, 150], and the tensile modulus decreases [13]. A mathematically robust cartilage model should be accurate under loads ranging from very low to physiologic or even supra-physiologic, and spatial heterogeneity is important if conclusions are to be made based on local stress distributions. The use of a depth-dependent cartilage material model for the analysis of cartilage cracks is crucial, given the intent to report spatial distributions of stresses throughout the cartilage thickness.

Methods

To begin development of such a model, a meta-analysis was performed of depth-wise cartilage properties reported in literature (Appendix). Unsurprisingly, there was substantial difference in reported material properties. To begin to compare these properties, each property value was logged with its corresponding normalized depth, from 0 at the articular surface to 1 at the subchondral bone interface. Thus, if a study reported a property measured from cartilage separated into three equal layers, those values were logged at depths of 0.33, 0.66, and 1, respectively. As shown in Figure 53, trends are visible, with the compressive and shear moduli increasing with depth, and the tensile modulus decreasing with depth. However, the amount of variation in the material properties precludes any particularly precise description of these trends. The scatter of material properties results from biologic variability, as well as varying testing conditions.

More useful trends can be derived by subdividing the above charts according to the testing speeds, toe/linear region, and testing direction. Furthermore, to focus on *variation* through the depth rather than on specific property values, each series of properties (from a given study) was normalized to the maximum value of that series. This allowed for the comparisons of trends between series with different testing conditions. As the graphs in Figure 54 show, taking these steps resulted in stronger correlations.

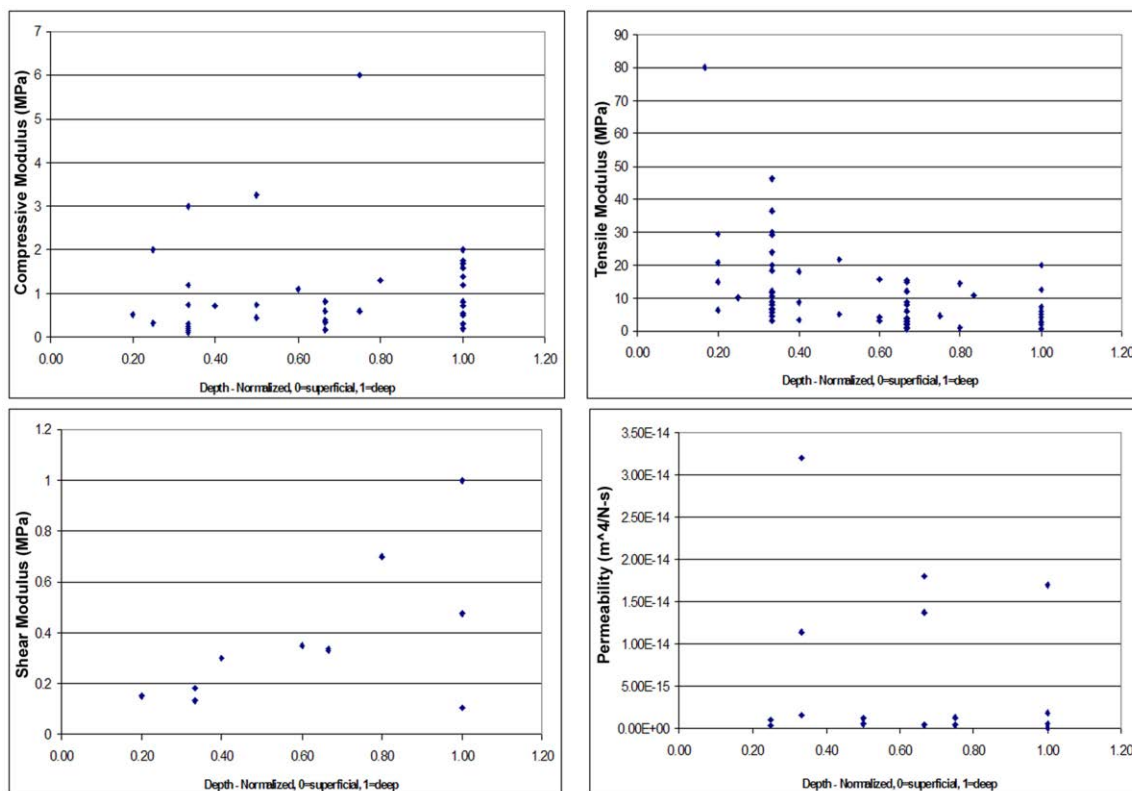


Figure 53. Variation of cartilage material properties through depth. Each data point's depth is normalized to the cartilage thickness.

Several outliers in the above graphs could be quickly explained through further investigation. Several compressive modulus data points having a y-value of '1' throughout the cartilage depth were from tests of the compressive modulus in which the load was applied parallel to the articular surface, rather than perpendicular as in the rest of the data points. No depth-wise variation of compressive modulus in this direction was found. The data point showing a normalized tensile modulus of 1 at the deepest point is actually 3 data points from testing by Verteramo and Seedhom, which found that the depth-dependence of the tensile modulus of cartilage disappeared at strain rates above normal physiologic levels, such as at 20, 50, and 70%/s [151]. Since the model being proposed here was intended for use at loads and loading rates up to and only modestly beyond physiologic levels, extremely high speed series of tensile moduli could be

disregarded. In addition, the compressive moduli in the direction parallel to the articular surface could be considered separately from those in the direction normal to the articular surface. If these exclusions were made, most outliers were removed, and very good trends emerged for the compressive and tensile moduli, as seen in Figure 55.

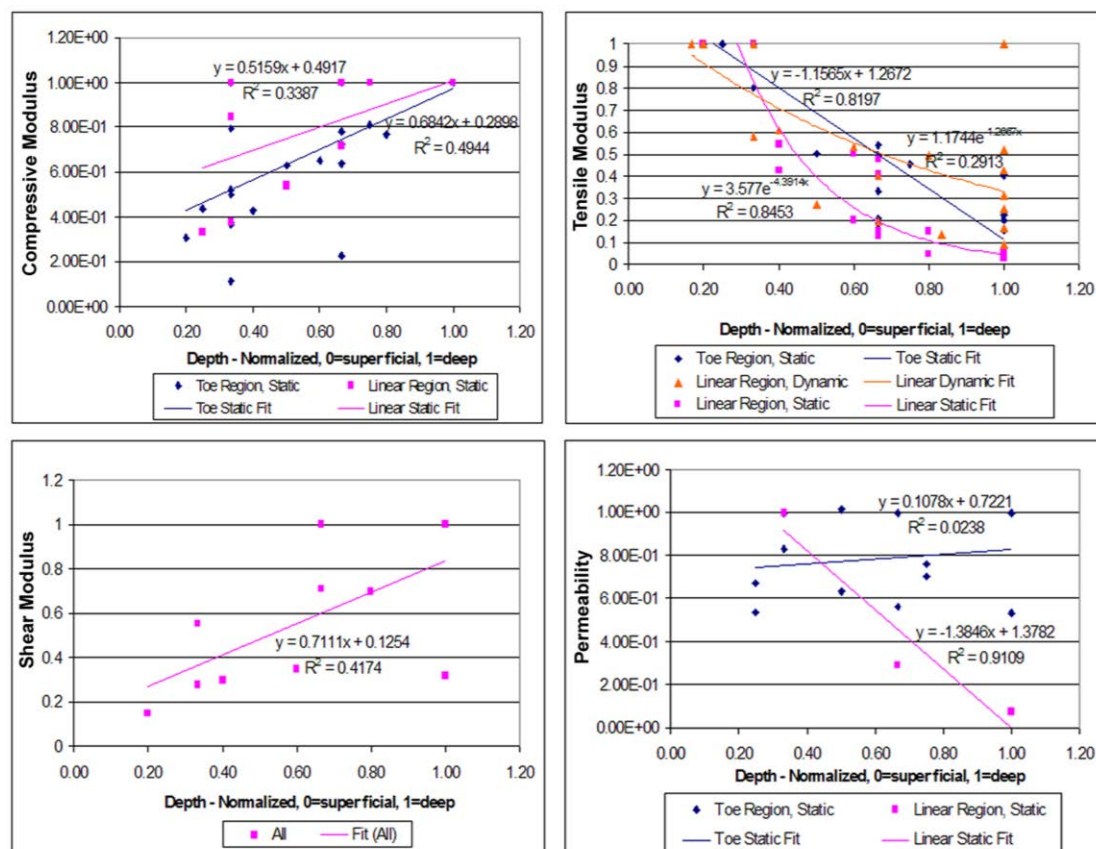


Figure 54. Depth-dependence of cartilage properties, separated by testing speed and strain region, and normalized to maximum series values.

The final material properties to consider were Poisson ratios. Poisson ratios are difficult to measure directly, usually requiring optical methods to determine lateral strain. Furthermore, Poisson ratios are not symmetric, that is, the Poisson ratio characterizing the lateral response to a load applied normal to the articular surface is not the same as that

characterizing the normal-direction response to a load applied in a lateral direction. Due to these circumstances, there are relatively few studies characterizing Poisson ratios as a function of depth. Furthermore, the formulation to be used in the material model would not make direct use of anisotropic Poisson ratios, as it only required an isotropic Poisson ratio for the non-fibrillar matrix. Therefore, only Poisson ratios coming from axial (normal to the articular surface) compression of cartilage were considered. These are used in Figure 56 to derive a linear relationship between Poisson ratio and cartilage depth.

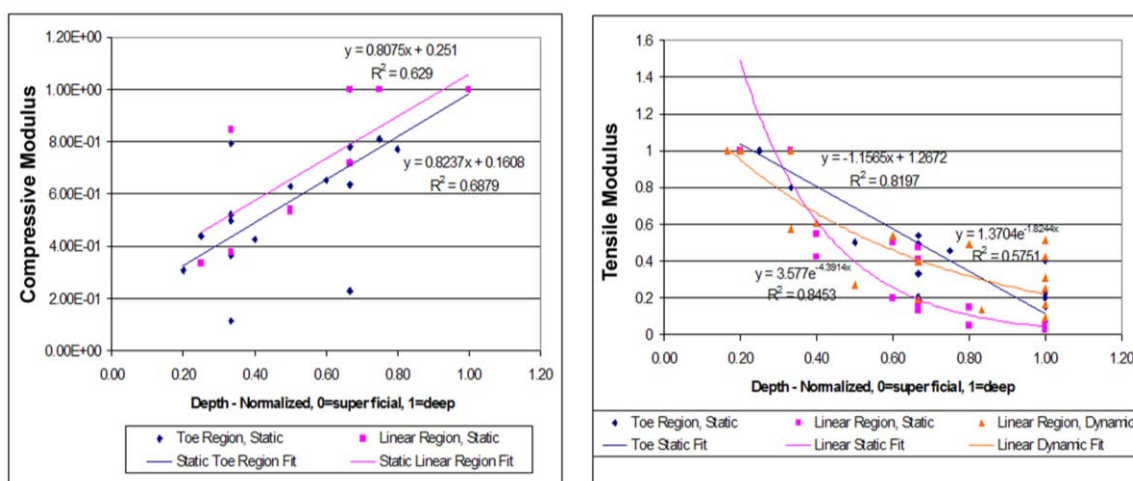


Figure 55. Compressive and tensile modulus variation with outliers removed.

The final material properties to consider were Poisson ratios. Poisson ratios are difficult to measure directly, usually requiring optical methods to determine lateral strain. Furthermore, Poisson ratios are not symmetric, that is, the Poisson ratio characterizing the lateral response to a load applied normal to the articular surface is not the same as that characterizing the normal-direction response to a load applied in a lateral direction. Due to these circumstances, there are relatively few studies characterizing Poisson ratios as a

function of depth. Furthermore, the formulation to be used in the material model would not make direct use of anisotropic Poisson ratios, as it only required an isotropic Poisson ratio for the non-fibrillar matrix. Therefore, only Poisson ratios coming from axial (normal to the articular surface) compression of cartilage were considered. These are used in Figure 56 to derive a linear relationship between Poisson ratio and cartilage depth.

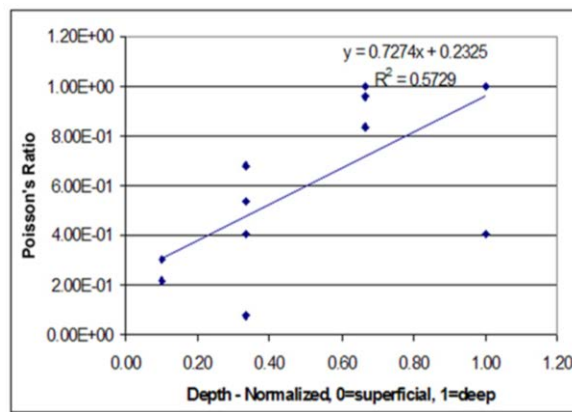


Figure 56. Variation of Poisson ratios, normalized to series maximum, with depth.

By fitting curves to the dual-normalized graphs shown in Figures 55 and 56, the following trends were established. First, the compressive modulus (E_c) in the toe region

$$\frac{E_c(d)}{E_c(1)} = 1.824 * d + 1.161, \quad (5.1)$$

and linear region

$$\frac{E_c(d)}{E_c(1)} = 1.808 * d + 1.251. \quad (5.2)$$

Also the dynamic tensile modulus (E_t)

$$\frac{E_t(d)}{E_t(0)} = 1.37e^{-1.824 * d}, \quad (5.3)$$

and the Poisson's ratio (ν)

$$\frac{\nu(d)}{\nu(1)} = 1.727 \cdot d + 1.2325. \quad (5.4)$$

Permeability was not found to have any consistent trend through the depth, and therefore was considered constant.

This depth-wise variation of cartilage properties was implemented into a poroelastic material model in FEBio, an open-source finite element package developed at the University of Utah. FEBio carries the advantage of being the only openly available finite element package to fully support poroelastic contact, with the biphasic “jump” or “sealed-at-contact” contact conditions implemented [152]. (Although poroelastic contact has been implemented in Abaqus through the use of subroutines, as described in the previous chapter, experience has shown that such implementations are very temperamental, particularly for irregular or complex geometries. Very recently, contacts at Simulia have indicated that the newest version of Abaqus treats poroelastic contact as desired without subroutines, but as of the time of this writing this version has not been distributed to our institution.) In addition, FEBio includes several material models specifically designed for biologic tissue, in particular several fiber-reinforced variants.

For this application, FEBio's *Ellipsoidal Fiber Distribution Neo-Hookean Poroelastic* model was used. In this model, the fluid and solid stresses are separated as described in Chapter 4 for the basic poroelastic model. The solid stress is then further subdivided into a contribution from the matrix ground substance (σ_{NH}), and a contribution from fibers (σ_f):

$$\sigma = \sigma_{NH} + \sigma_f. \quad (5.5)$$

The matrix ground substance is represented by a Neo-Hookean formulation, with the strain energy formulation

$$W = \frac{\mu}{2}(J_1 - 3) - \mu \ln J + \frac{\lambda}{2}(\ln J)^2, \quad (5.6)$$

where μ and λ are material properties, I_1 is the first invariant of the right Cauchy-Green deformation tensor, \mathbf{C} , and J is the determinant of the deformation gradient tensor.

The fiber contribution to the stress is a spherical integration of fiber stresses, σ_n , in all directions, according to

$$\sigma_f = \int_0^{2\pi} \int_0^\pi H(I_n - 1) \sigma_n(n) \sin(\varphi) d\varphi d\theta, \quad (5.7)$$

where \mathbf{n} is a unit vector along the fiber axis direction (θ, φ) , and $I_n = \lambda_n^2 = \mathbf{n} \cdot \mathbf{C} \cdot \mathbf{n}$ is an invariant related to the fiber stretch, λ_n^2 . $H(\cdot)$ is the unit step function, and enforces a tension-only contribution by the fibers. Finally, the fiber stress is defined in a fiber strain energy equation

$$\sigma_n = \frac{2}{J} F \cdot \frac{\partial \Psi}{\partial \mathbf{F}} F^T = \frac{2I_n}{J} \frac{\partial \Psi}{\partial \lambda_n} \mathbf{n} \otimes \mathbf{n}, \quad (5.8)$$

where

$$\Psi(\lambda_n, I_n) = \xi (I_n - 1)^\beta, \quad (5.9)$$

and ξ and β are material properties. In general, ξ and β are functions of \mathbf{n} , that is, they can vary with direction to model a non-uniform fiber distribution and the resultant anisotropy. However, for initial development ξ and β were treated as constants. This resulted in a material model with 5 constants: an elastic modulus (E), Poisson's ratio (ν), permeability (k), fiber-law scalar (ξ) and fiber-law exponential (β).

To incorporate the depth-wise variation derived above into this material model, the elastic modulus of the matrix ground substance was assumed to represent the compressive modulus in the toe region (Equation 5.1), and ξ was assumed to vary with the same trend as the tensile modulus in dynamic loading (Equation 5.3). The Poisson's ratio of the ground matrix was set to vary according to Equation 5.4, and permeability was constant through the depth. To prescribe the material properties, each property was

specified at its highest value, at the subchondral bone interface for elastic modulus and Poisson's ratio, and at the articular surface for ξ .

Results

The deep elastic modulus, deep Poisson's ratio, and superficial permeability were set as median values from all of the studies in the literature survey: 0.995 MPa, 0.194, and 0.00191 mm⁴/(N-s), respectively. The fiber stress law in Equation 5.8 and 5.9 could be differentiated with respect to strain to determine the fiber modulus (E_f) as a function of fiber stretch (λ_n), β , and, ξ :

$$E_f = \frac{4 \cdot \lambda}{J} \cdot \beta \cdot \xi \cdot (\lambda^2 - 1)^{\beta-1} + \frac{2 \cdot \lambda^2}{J} \cdot \beta \cdot \xi \cdot (\beta - 1) \cdot (\lambda^2 - 1)^{\beta-2} \cdot 2 \cdot \lambda \quad (5.10)$$

Following initial testing, it was determined that setting β to 2.5 (unitless) resulted in appropriate nonlinearity in the stress-strain behavior of the cartilage model. The median dynamic, linear-region tensile modulus from the literature review was 32.2 MPa. Using this modulus and a 5% strain ($\lambda_n = 1.05$) resulted in $\xi = 3.155$ MPa. In FEBio, a model was created replicating the multi-rate unconfined compression of Park et al. [21]. This model consisted of a quarter-model of a cartilage plug, with a rigid platen applying a compressive load (Figure 57). In the experimental setup, the cartilage was shaved from its subchondral plate, so the bottom surface of the FE model was given freedom to slide in the radial direction. The cartilage plug consisted of 10 layers of elements, with each layer assigned appropriate depth-dependent properties. The plug was compressed to a nominal stress of 5.67 MPa (40 N) at speeds of 0.1, 1, 10, and 40 Hz. The nominal stress-strain curves from the finite element model displayed reasonable agreement with the experimental results (Figure 58). The final material properties and their depth-wise variation are shown in Figure 59.

Several studies in literature investigate the depth-wise variation of strain or displacement in compression of cartilage plugs. With the material model set as in the

previous paragraph, two of these studies were simulated in FEBio to test the accuracy of the material model. In all cases, the geometry of the test was very similar to that of the Park et al. test, except for some variations in specimen size and loading protocol. Zheng et al. [153] performed stress relaxation experiments (two steps of a ramp displacement, followed by time for the tissue to relax) and measured the resulting dynamic displacement at discrete points through the thickness using ultrasound. As shown in Figure 60, the depth-dependent model developed here reasonably captured the magnitude of the displacements and the relaxation behavior.

Neu et al. performed unconfined compression of cartilage and calculated three-dimensional depth-dependent strains using a specialized MRI technique [154]. In replicating that model, the magnitude and trends of the axial and radial strains agreed very well. The computed shear strains were slightly low, but still showed agreement with the general trend. The experimental and finite element results are shown in Figure 61.

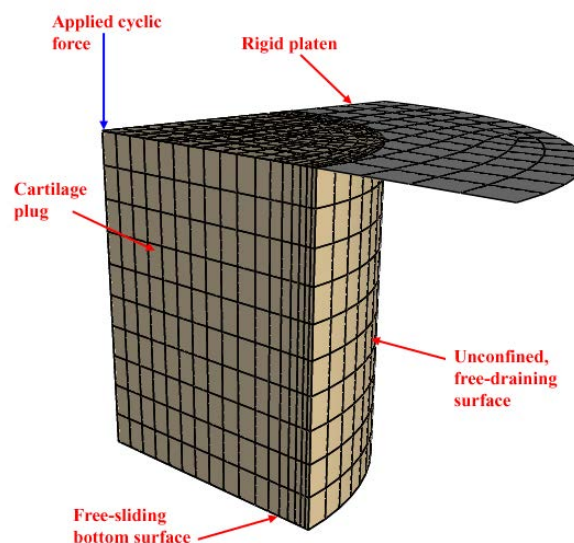


Figure 57. Finite element model of unconfined compression, using two planes of symmetry.

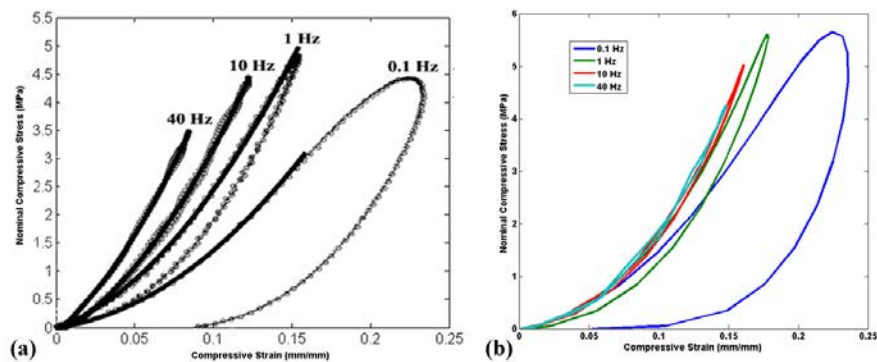


Figure 58. Unconfined compression of cartilage from (a) experimental, and (b) depth-dependent finite element analysis.

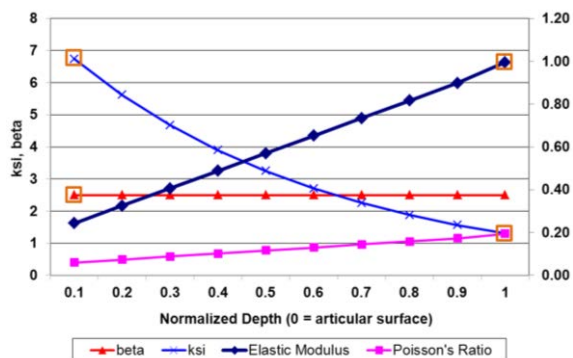


Figure 59. Depth-wise variation of cartilage material properties. Orange boxes indicate the four independent properties values that need to be specified.

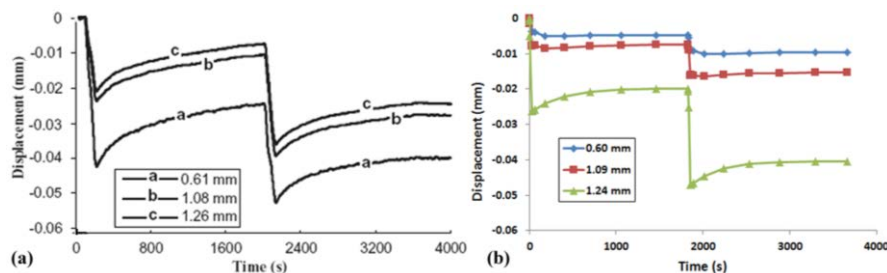


Figure 60. Comparison of depth-dependent displacements from (a) physical tests, and (b) corresponding finite element simulations. Each line follows a single point at the specified depth from the articular surface.

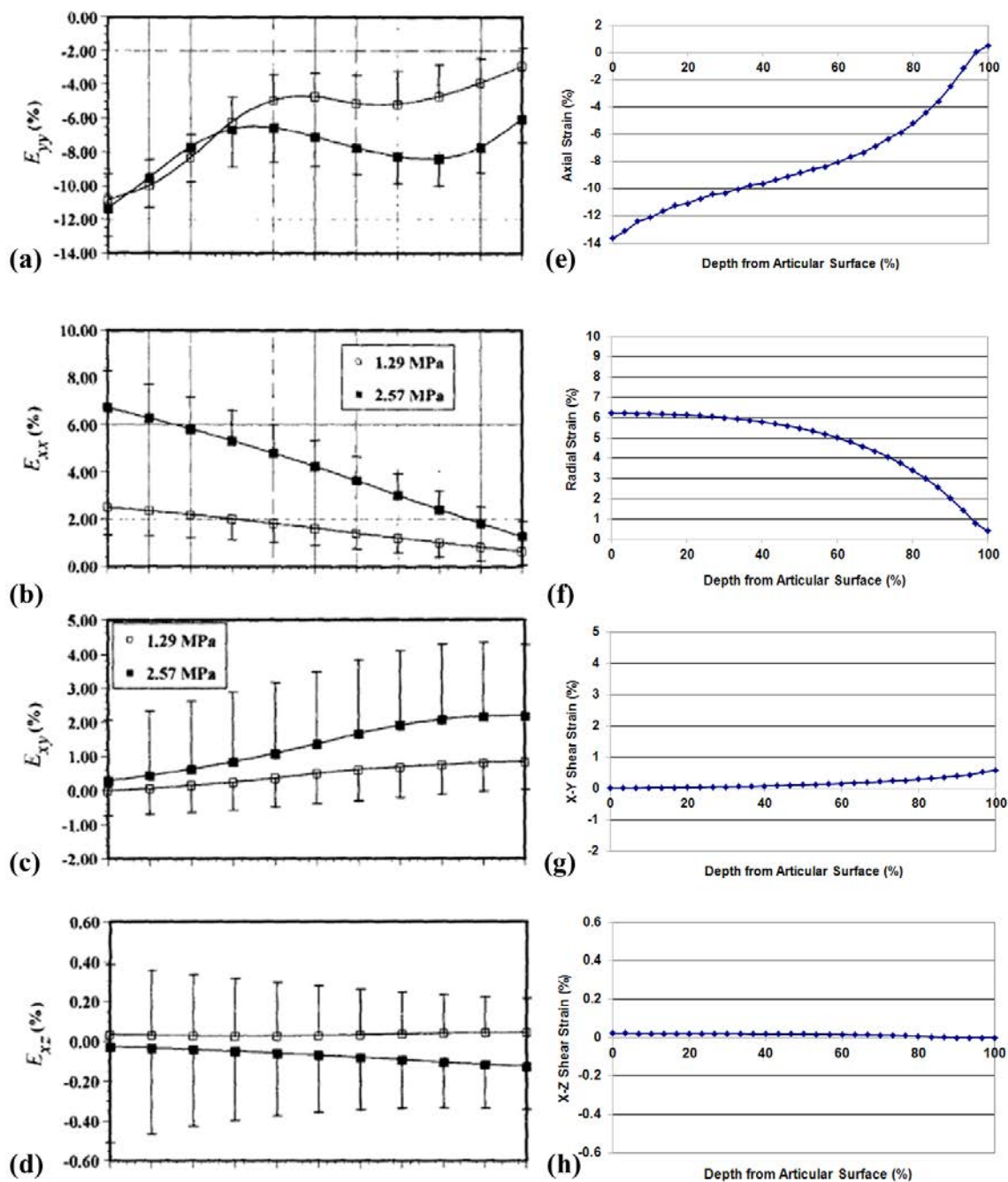


Figure 61. Comparison of (a-d) through-thickness cartilage strains from MRI testing with (e-h) corresponding finite element simulations. FE simulations replicated the 2.57 MPa physical tests.

Finite element modeling of the local stress environment
around cartilage cracks

Methods

Finite element models of cartilage cracks were created using the depth-dependent material model that was developed and validated in the previous section. Two cartilage layers representative of the cartilage of the rabbit tibio-femoral joint were created (Figure 62). The femoral cartilage had a radius of curvature of 7 mm, based on measurements by Borrelli [155], while the tibial cartilage had a radius of curvature of 12 mm. The geometry for this series of models was based on the histology results of Chapter 3, which provided no information about the out-of-plane shape of the cracks. Based on the results of Flachsmann et al. [141, 142], it is not unreasonable to assume that cracks are long relative to their cross-sectional width, so the cartilage crack was simulated with a plane-strain model. FEBio is strictly a three-dimensional finite element software package, so the cartilage layers were modeled with just a single out-of-plane element (0.5 mm thick), constrained to enforce plane-strain behavior.

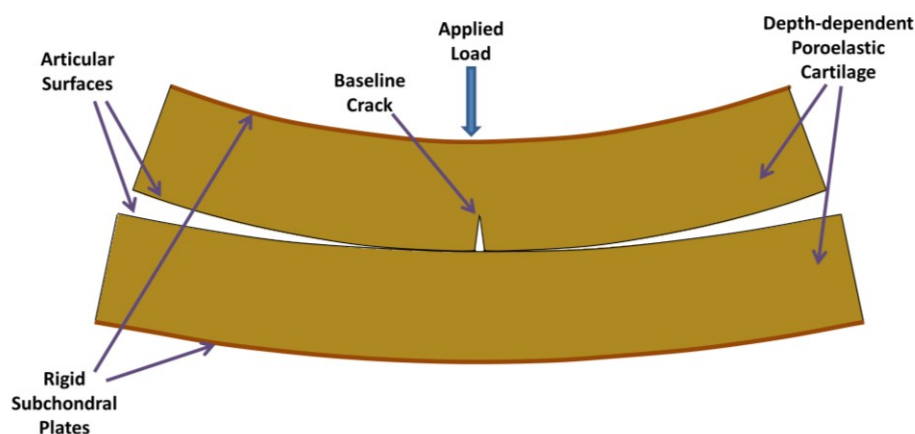


Figure 62. Finite element model of cracked cartilage. The full model was extruded one element deep in the out-of-plane direction.

The models created included a normal, uncracked geometry, a baseline crack model, and several perturbations of the baseline crack. All simulations used uniform cartilage thickness of 0.76 mm, the average cartilage thickness from the results in Chapter 3. The baseline crack geometry was determined from the average surface cracks identified in Chapter 3. This resulted in an idealized triangular crack with a width of 69 μm , extending through 37% of the cartilage thickness, at an angle perpendicular to the articular surface (the average crack was actually at 78 degrees to the articular surface, but for simplicity of perturbations, a perpendicular crack was used as the baseline, and the 78 degree crack was included as one of the variations). The crack was placed in the center of the femoral cartilage. 0.025 mm edge rounds were applied at the crack opening corners to avoid element distortion.

Contact was defined between the two articular surfaces as well as between the opposing crack faces. Poroelastic contact in FEBio includes the so-called ‘biphasic jump’ condition, whereby nodes not in contact are free-draining (zero pore pressure) and fluid flux continuity is maintained across surfaces in contact. The subchondral plates were considered rigid. The inferior subchondral plate was constrained in all directions. A vertical load of 3 N, corresponding to approximately 3 MPa contact pressure, was applied to the femoral subchondral plate, and all remaining degrees of freedom for that rigid body were constrained. The cartilage layers were meshed with 8-node hexadral elements except within 0.1 mm of the crack, where 6-node wedge elements were used to allow greater localized mesh refinement. A two-stage mesh convergence study was performed to determine the necessary element size. A global mesh with 0.025 mm element edge lengths was found to be convergent everywhere except in the immediate vicinity of the crack, where a refined mesh of 0.0075 mm demonstrated convergence (Figures 63 and 64). The final crack mesh is shown in Figure 65.

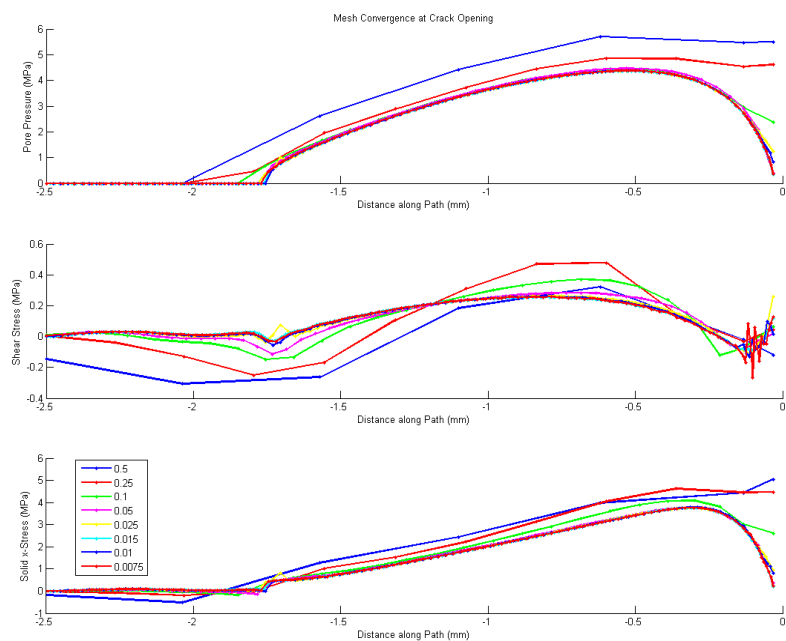


Figure 63. Mesh convergence approaching the crack opening. Element sizes 0.5 down to 0.015 represent global criteria, while 0.01 and 0.0075 are local refinements.

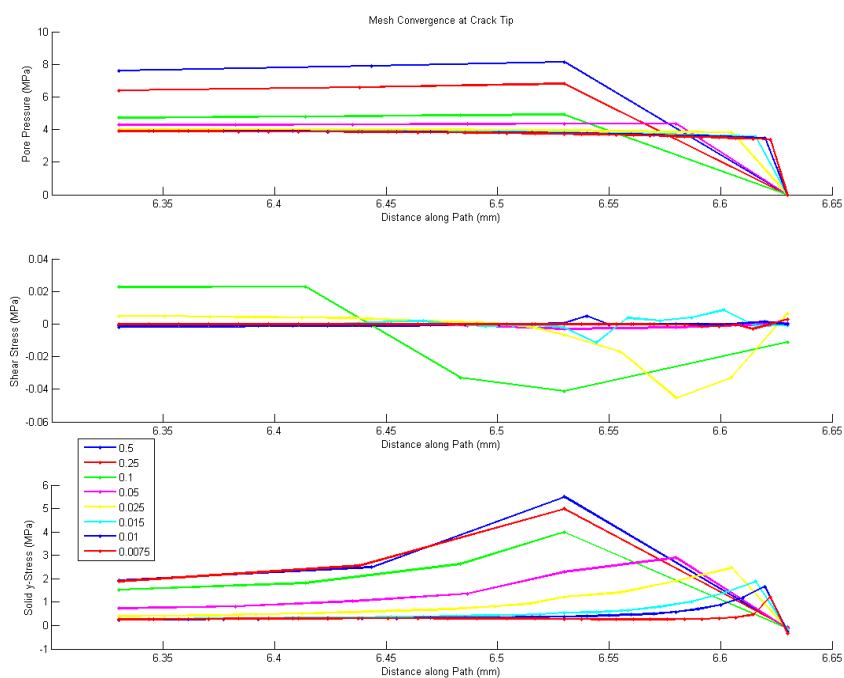


Figure 64. Mesh convergence approaching the tip. Element sizes 0.5 down to 0.015 represent global criteria, while 0.01 and 0.0075 are local refinements.

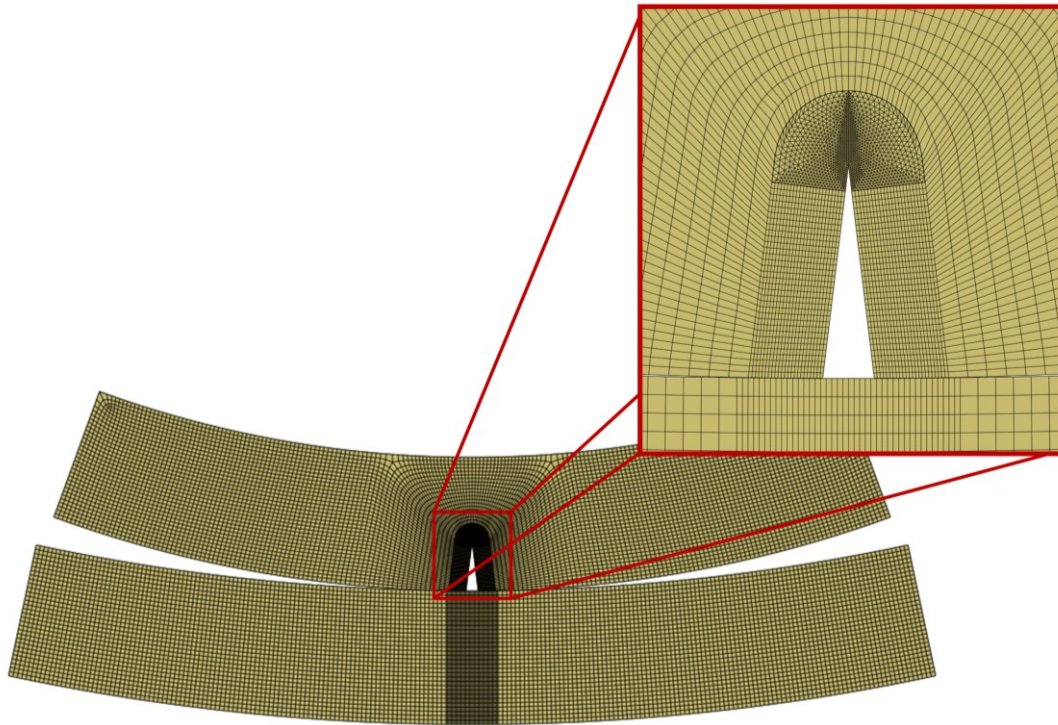


Figure 65. Final mesh for the baseline crack model.

Following creation of the uncracked and baseline crack models, 18 perturbations of the baseline crack were created, as illustrated in Figure 66. The width of the crack was decreased by half, and increased by a factor of 2, 3, and 4. The depth of the crack was reduced by half, and doubled. The angle of the crack relative to the articular surface was altered to 78 degrees (the average from Chapter 3) and to 20 degrees. A thin ($4\ \mu\text{m}$) vertical crack was created through the transitional zone. In order to test the ability of a hydrogel or other material to provide mechanical stabilization and restore cartilage stresses around a crack to near-normal conditions, a model was created in which the baseline crack was filled with a single-phase material with a compressive modulus of 2 MPa and a Poisson ratio of 0.45. Finally, to investigate the possible synergistic effects of multiple cracks in close proximity, a series of models were created in which the baseline

crack geometry was used for two cracks separated by distances varying from 0.25 mm to 2 mm.

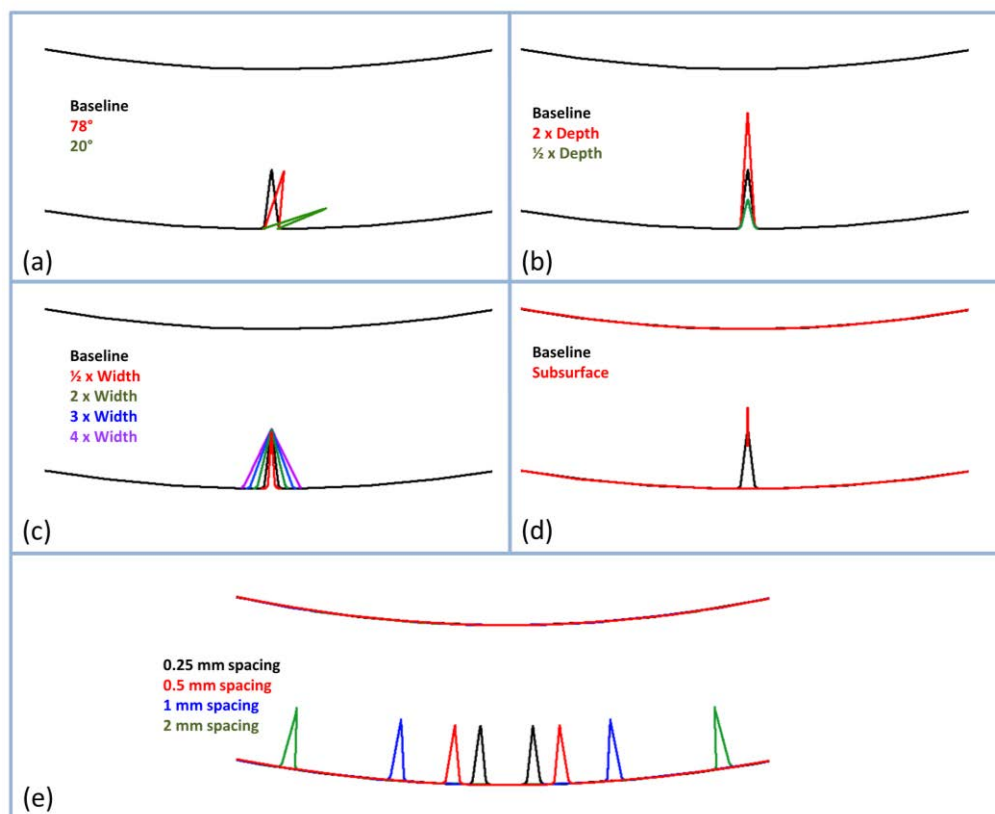


Figure 66. Perturbations to the crack geometry included altering the (a) crack angle relative to the local articular surface, (b) crack depth, and (c) crack width. (d) A hairline subsurface crack was created and (e) a series of geometries with two cracks of varying spacing was generated.

Results

Figure 67 shows the pore (fluid) pressure and strain distributions from the normal, uncracked model and the baseline crack. It is immediately obvious that a small, single crack dramatically undermines the fluid load support in the vicinity of the crack and throughout the cartilage depth. Shear strain is increased around the crack, although the most pronounced increase is near the crack tip, while little shear strain is seen along the

crack faces where increased chondrocyte death has been reported [146]. The magnitude of the compressive strain, on the other hand, is greatly increased along the crack face, relative to the uncracked model. Tensile strain is reduced approaching the crack faces and directly below the crack tip, although it is slightly increased in the other regions.

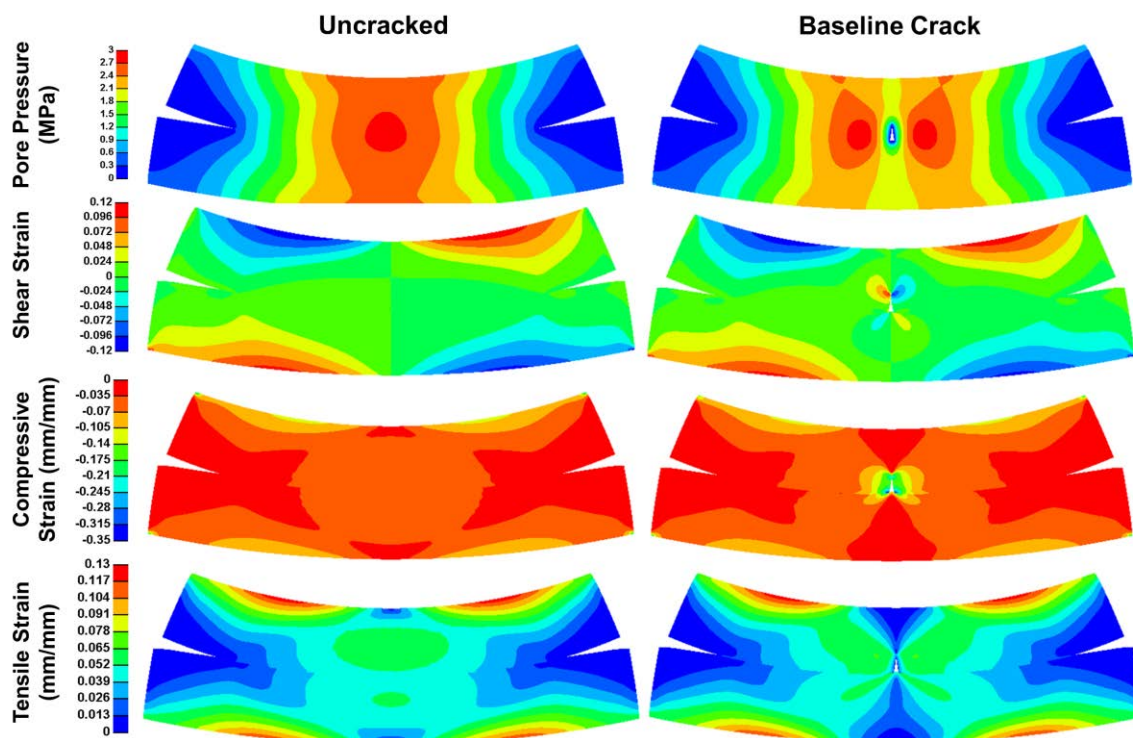


Figure 67. Fluid pressure and strain distributions in the uncracked and baseline crack finite element models.

The increase in compressive strain near the crack face is due to the loss of fluid load support in that region. As fluid drains from the free-draining crack faces, the soft matrix is significantly compressed, much as happens in *in vitro* tests of cartilage during unconfined compression. Figure 68 shows the substantial localized deformation that occurs in the cracked cartilage mesh compared to that occurring in the uncracked cartilage.

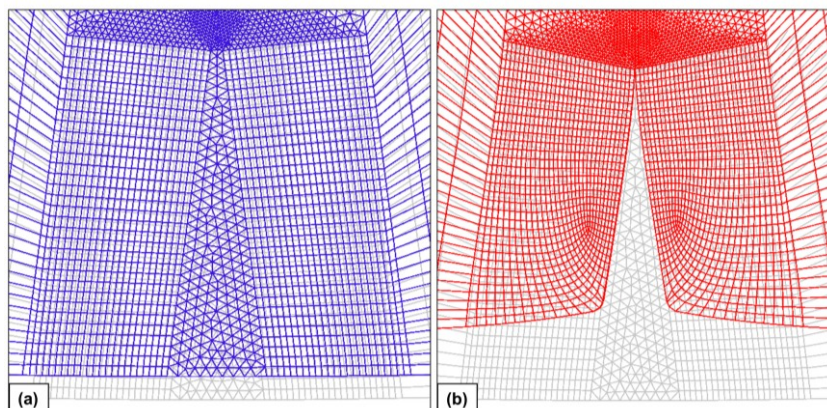


Figure 68. Deformed meshes of the (a) uncracked, and (b) baseline crack FE models, both overlaid on the undeformed mesh of the uncracked model.

In order to more directly compare the uncracked model results to the various crack perturbation results, line plots were extracted from paths parallel to the femoral articular surface, as shown in Figure 69. Figures 70 and 71 show the pore pressure and strains for the uncracked and baseline crack models at several depths from 10% to 90% of the cartilage thickness. The largest differences between the baseline crack model and the uncracked model were in the superficial zone. As this was also the case for other crack perturbations, the results in this section will focus on line plots extracted along a path 100 μm below the articular surface.

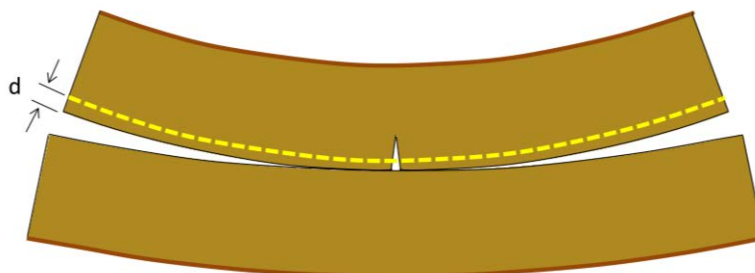


Figure 69. Line plots of the strain and pore pressure output were extracted along a path at depth 'd' parallel to the tibial articular surface, as shown.

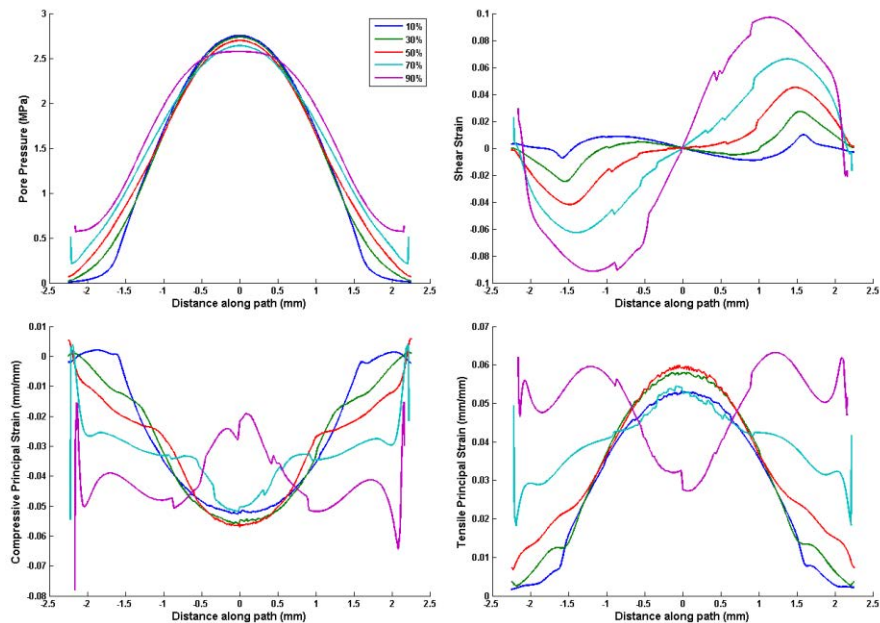


Figure 70. Fluid pressure and strains at various relative depths from the articular surface in the uncracked model.

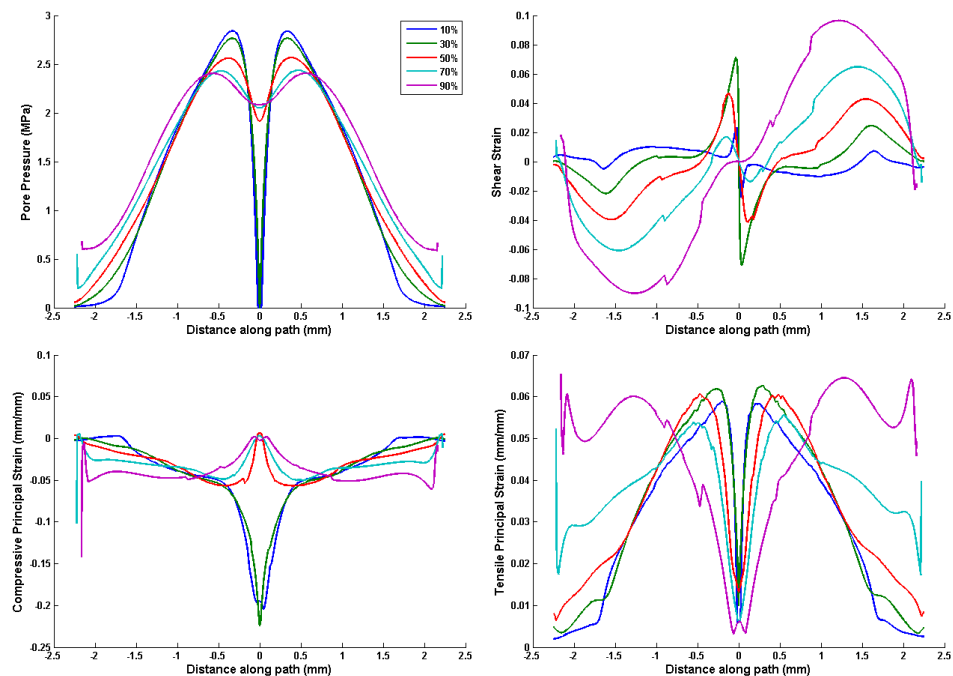


Figure 71. Fluid pressure and strains at various depths from the articular surface in the baseline crack model.

Figure 72 shows the change in the pore pressure and strain along the 100 μm deep pathline as the width of the crack is altered. The maximum fluid pressure increases slightly with increasing width, although even at 4 times the baseline crack width, the increase in peak fluid pressure is less than 0.5 MPa. Tensile strain increases slightly and then drops off suddenly close to the crack face, and the magnitude of the peak tensile strain is independent of the crack width. The most significant effect of the cracks is again in the compressive strain. Narrower cracks actually experience slightly higher peak compressive strains, likely because the edges of the crack are still within the highest-load portion of the cartilage (due to the curved nature of the contacting surfaces, the load is always concentrated at the center of the model). Regardless of the crack width, the altered compressive strains span a distance of about 1 mm around the crack (0.5 mm on each side of the crack centerline), outside of which the compressive strains mirror those in the uncracked model.

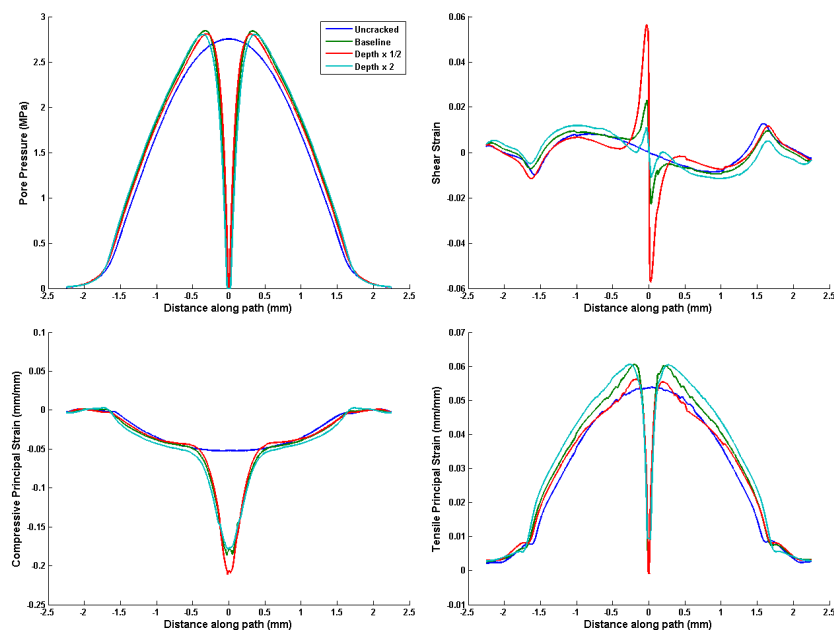


Figure 72. Fluid pressure and strains 100 μm below the articular surface as the crack width is altered.

Altering the crack depth had little influence on the resulting pore pressure or strains, as shown in Figure 73. The crack faces near the tip in the deeper cracks come into contact early in the simulation, allowing fluid pressure to be restored. The results of the crack depth and crack width perturbations suggest that the final fluid pressure and strain states are largely dominated by the amount of the crack faces which are not in contact. The deeper cracks do have a slightly increased tensile strain in the superficial zone, with the deepest crack having a peak tensile strain approximately 20% higher than the uncracked model and 10% higher than the shallowest crack.

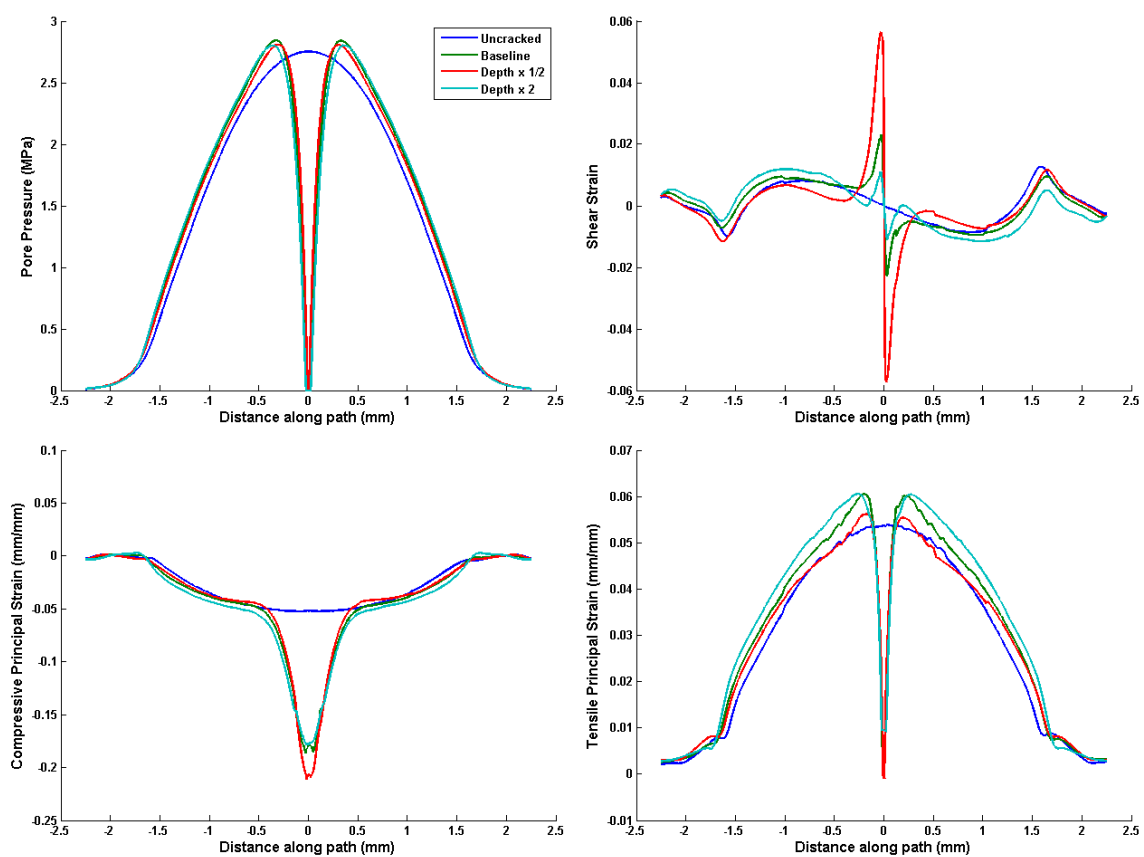


Figure 73. Fluid pressure and strains 100 μm below the articular surface as the crack depth is altered.

Altering the angle of the crack from the baseline (90 degrees) to 78 degrees had virtually no effect on the pore pressure, compressive strain or tensile strain. As Figure 74 shows, the shear strain does change slightly, although the magnitudes do not change dramatically. When the crack angle is adjusted to 20 degrees, the crack is virtually completely closed (Figure 75), and the reduction in fluid pressure is much less than in the baseline crack. The magnitude of the alterations to the compressive strain is not as large in the 20° model.

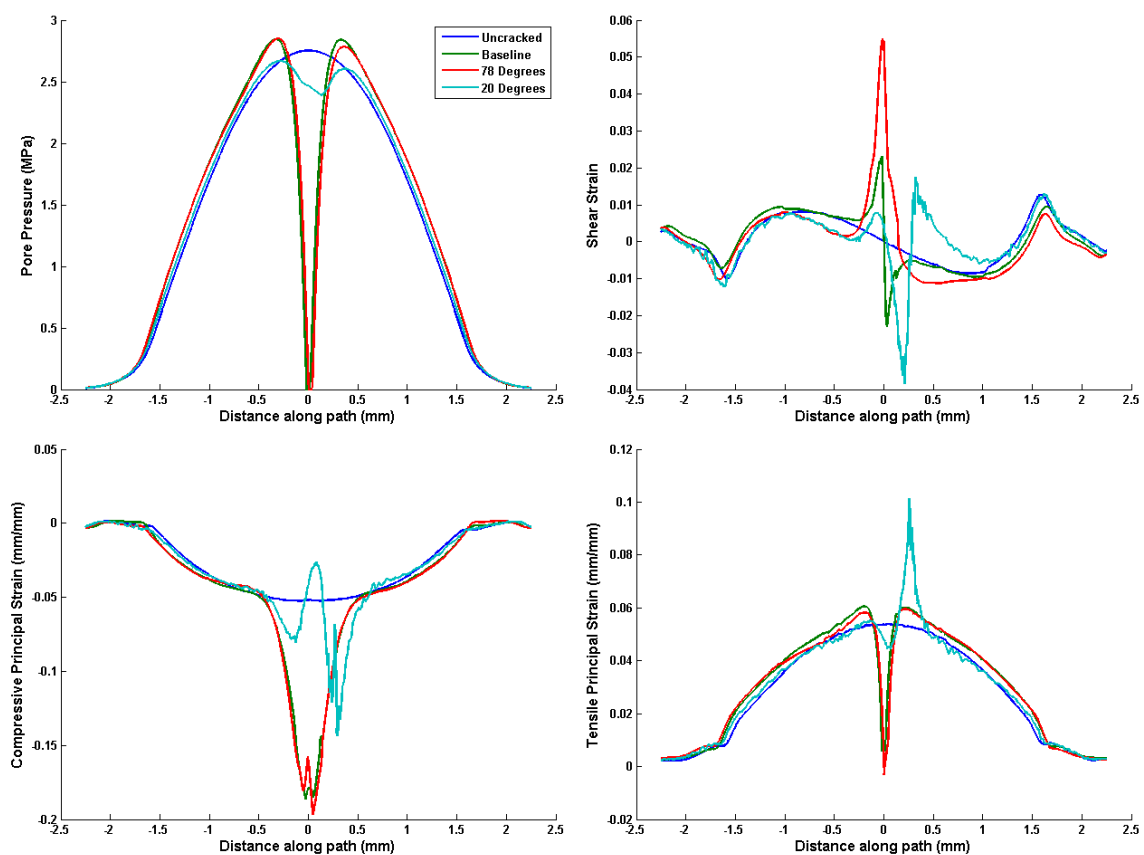


Figure 74. Fluid pressure and strains 100 μm below the articular surface as the crack angle is altered.

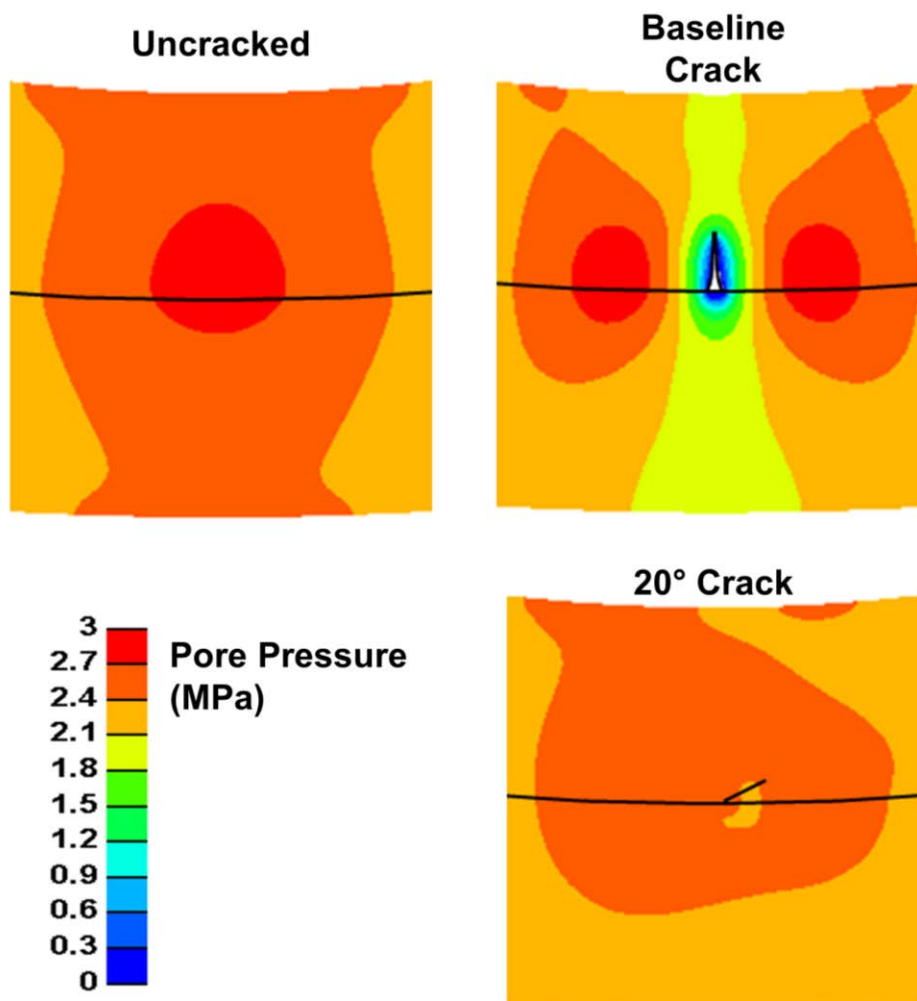


Figure 75. Comparison of the pore pressure in the uncracked, baseline crack, and 20° angle cracks.

Figure 76 shows the pore pressure and strains for a small, thin, subsurface crack, representative of the subsurface cracks found in Chapter 3. For this model, the output was extracted from a path 300 μm below the articular surface, which bisects the crack. In the subsurface crack, only slightly decreased fluid load support is again seen near the crack faces, largely because the crack is so thin that it closes quickly, before much of the fluid phase can be forced out of the tissue.

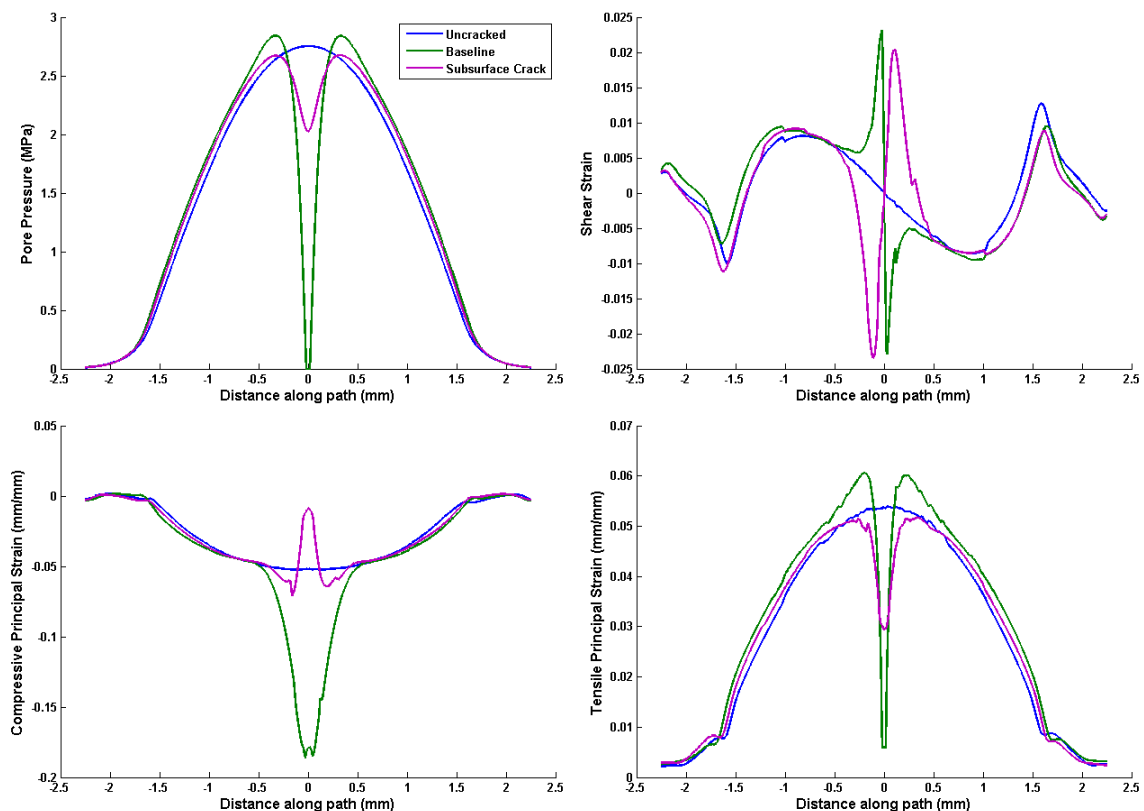


Figure 76. Fluid pressure and strains 300 μm below the articular surface in the subsurface model.

Figure 77 shows the results when the baseline crack is filled with a single phase material with a compressive modulus of 2 MPa. The filled crack is restored nearly to the uncracked levels. This reinforces previous observations that the degree of crack closure (how quickly and completely the crack faces come into contact and stop fluid exudation) is the key determinant of the alteration of the local strain field. This analysis shows that a crack filling material could potentially be successful at restoring the local strain environment. More testing is needed to determine the optimal material properties needed, in terms of stiffness and strength, although it appears that the ability to seal the crack is of more critical importance than tensile strength or bonding.

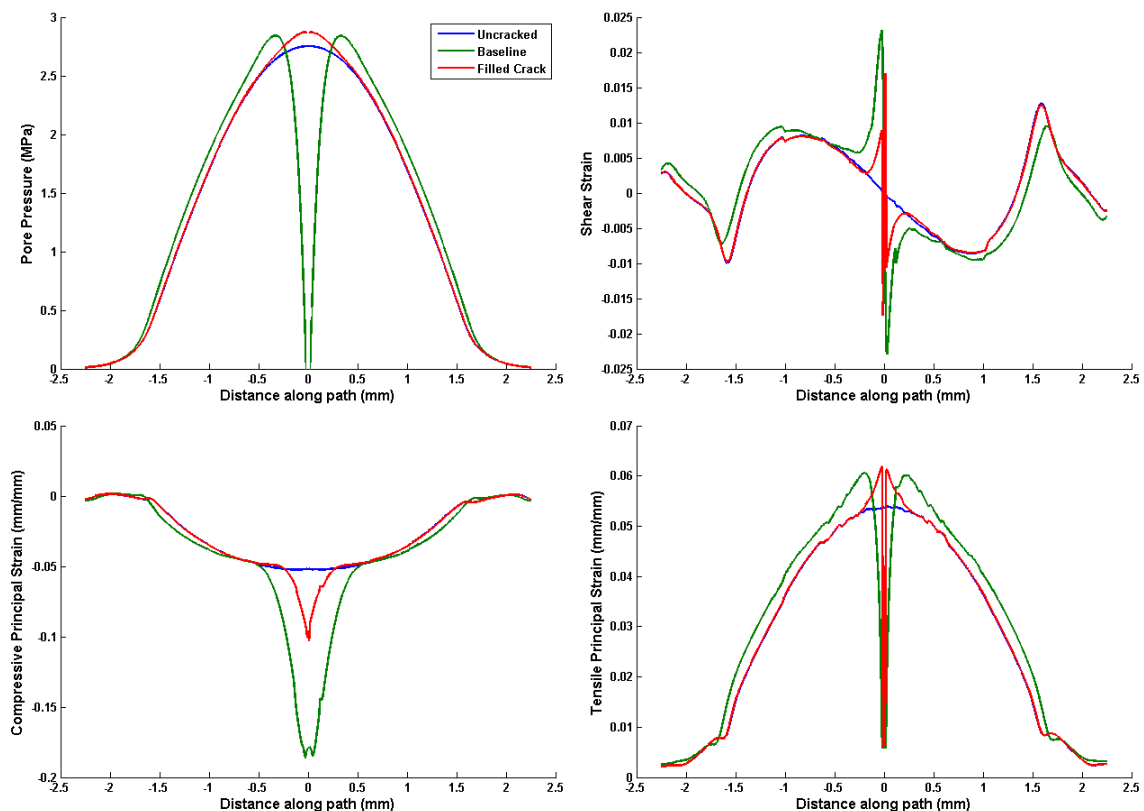


Figure 77. Fluid pressure and strains 100 μm below the articular surface in the filled crack model.

The analysis to this point has focused on the effects of a single crack. Figure 78 shows the effect of two cracks on the local pore pressure and strain environment, as the distance between the cracks is varied. As was the case for all crack simulations, only modest differences in pore pressure were seen. Also as seen before, increased compressive strains were apparent. When the cracks were separated by 1 mm or more, they functioned as independent cracks, with fluid pressures and strains similar to the single baseline crack. However, when the cracks were placed in closer proximity, the area between the cracks was subjected to increasingly high strains. The thin strip of cartilage between two cracks separated by 0.25 mm experienced compressive strains exceeding 0.25 mm/mm, which is 20% higher than in any individual crack model. In

fact, the simulation with 0.25 mm spacing could not run quite to completion, due to the instability of the thin strip of cartilage (Figure 79). Thus, the 0.25 mm/mm strains reported occur at only 90% of the load of the other simulations discussed. Such closely spaced, discrete cracks are seen in cartilage histology (Figure 80). Local quantification of proteoglycan content as performed by Moussavi-Harami et al. [112] and cell counting measurements would provide quantitative information about cartilage health, to compare to the strain distributions documented here.

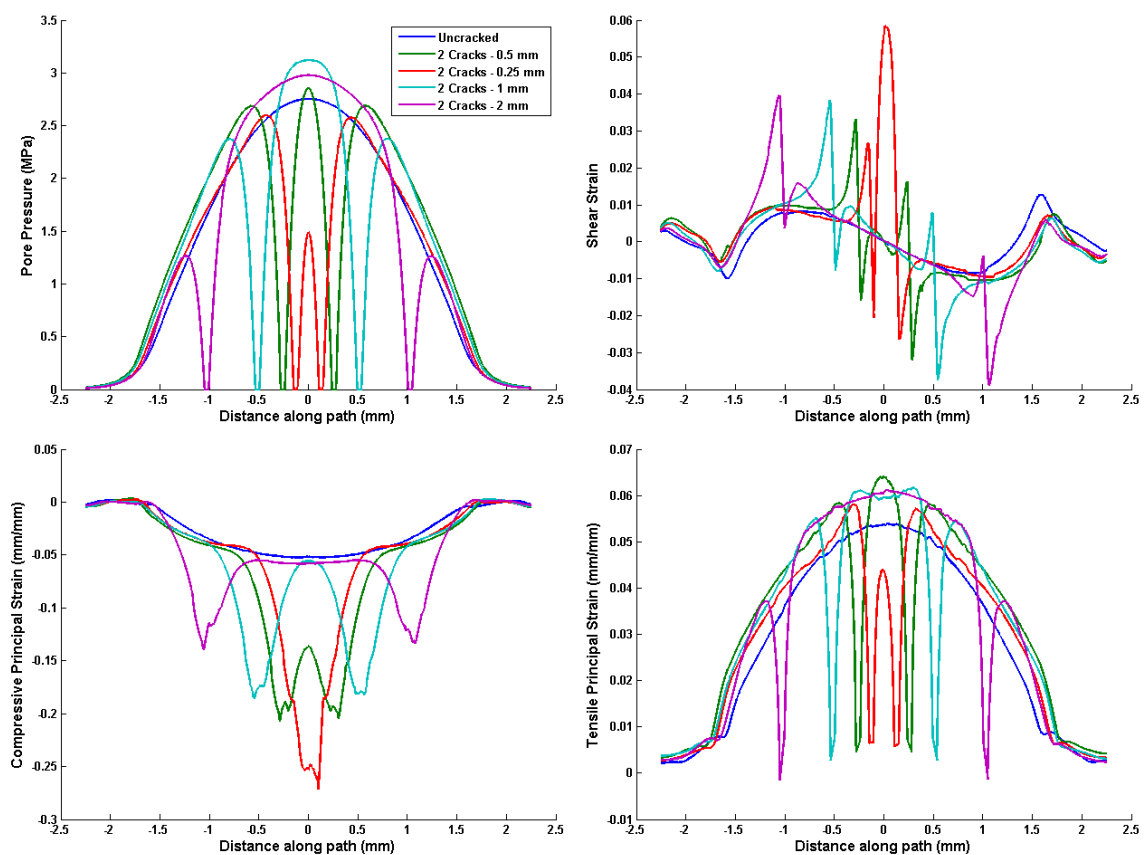


Figure 78. Fluid pressure and strains 100 μm below the articular surface, as the proximity of two cracks is adjusted.

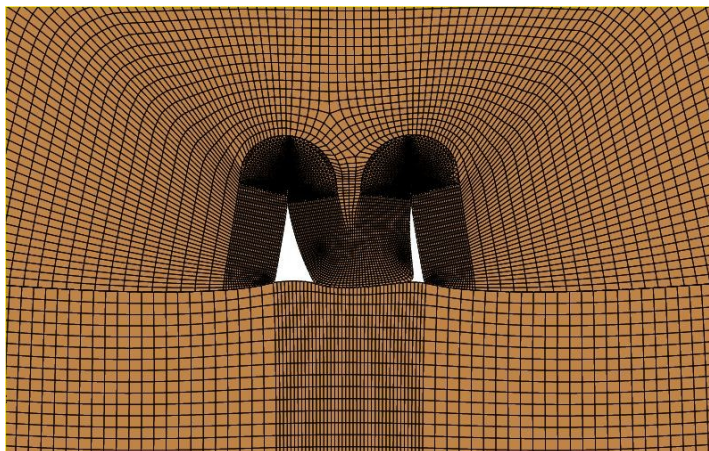


Figure 79. Deformed mesh for two cracks separated by 0.25 mm. The thin strip of cartilage between the cracks is unstable due to being underconstrained, which causes premature termination of the analysis.

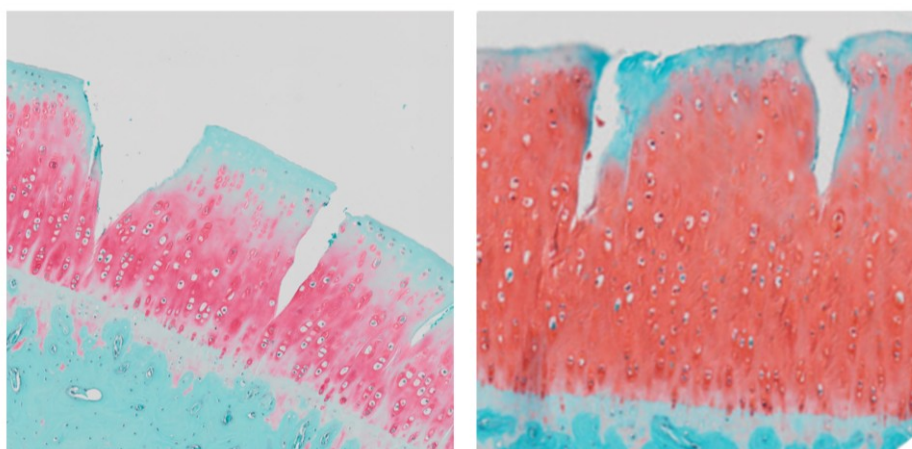


Figure 80. Examples of multiple cracks in cartilage histology.

A finite element model of cascading degradation in
structurally-damaged cartilage

In the previous section, the effect of cartilage cracks on the local fluid pressure and strain environment was investigated. Those studies indicated substantial alterations to the strain field surrounding a crack. However, it is difficult to assess what the long-

term chronic effects of these strain alterations would be. In this section, a framework was developed through which a theoretical cartilage damage law could be proposed, and computational simulations were used to determine whether that damage law would cause propagation of cartilage degeneration from a local abnormality to more wide-spread degradation.

Methods

The master degeneration program was written in Matlab. The key concept of this framework was a damage law, consisting of a damage criterion and a damage effect. The user defined a damage criterion by selecting the variable of interest, which could be a strain or stress component (or invariant) or the pore pressure, and a damage threshold. The effect of the damage was specified as a percentage change in material properties. An example of a complete damage law might be “compressive principle strain greater than 0.1 mm/mm causes a reduction in elastic modulus and increase in permeability of 10%”.

The degeneration program, called DEGEN and illustrated in Figure 81, started with the function `AbaqusReader`. This function read the model geometry, including the nodes, elements, sets, and surfaces from an Abaqus input file and stored it to the Matlab structure `feData`. (Although there is a preprocessing software package associated with FEBio, at this point Abaqus CAE remains a much more versatile and reliable platform for mesh creation.) Next, the `Analysis` function was called. This function operated on the `feData` structure. Upon its first call, it calculated the depth-varying material properties for each element. The `Analysis` function contained the complete FE simulation parameters, and modified `feData` to include the desired contact interfaces, boundary conditions, and time-step definitions. Analysis finished by calling `WriteFEB`, which wrote the text file FEBio would read as input (`febFile`), and returning the modified `feData` structure to DEGEN. DEGEN then called FEBio, which performed the analysis in `febFile`.

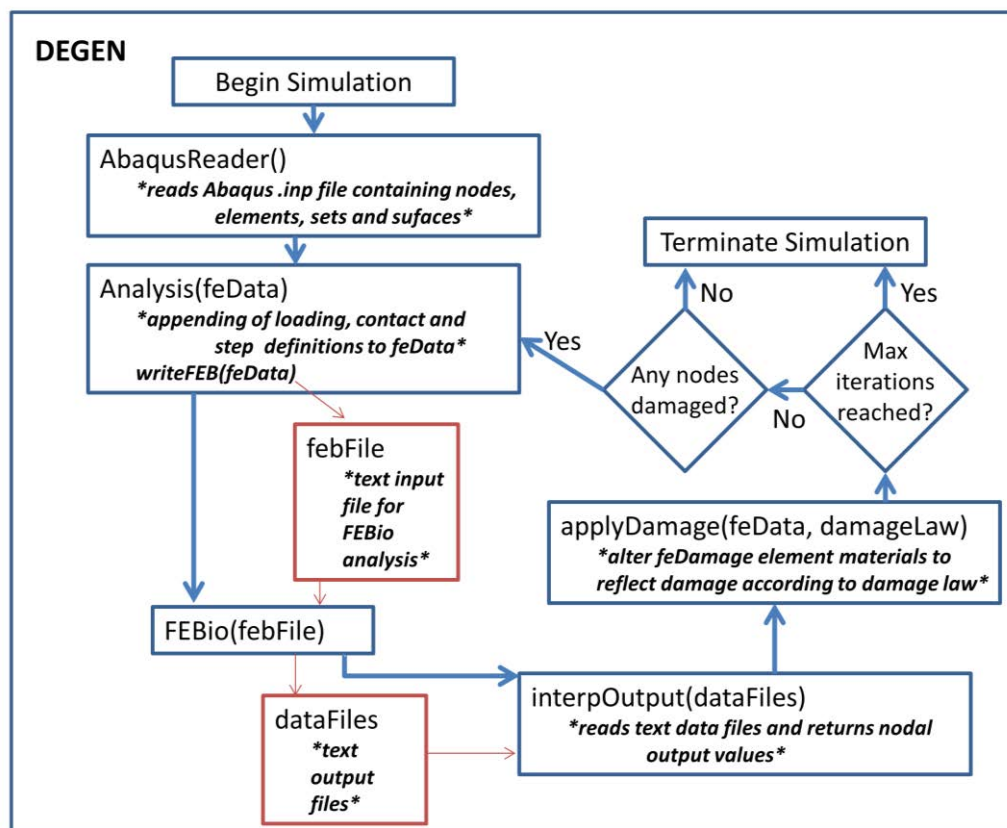


Figure 81. Flowchart illustrating the functionality of the degeneration simulation algorithm, DEGEN.

In addition to FEBio's standard output format of *.plt database files, a flag was set in FEBfile which instructed FEBio to write all strain, stress, and pore pressure data to easily accessible text files. The function interpOutput read the text file containing the variable cited in the damage law, and DEGEN determined which nodes exceeded the damage criterion. The damaged nodes were then fed into applyDamage. applyDamage identified all of the material models affiliated with the damaged nodes and created new copies of those material models, with material properties altered as defined in the damage effect portion of the damage law. All elements containing damaged nodes were remapped to the new, altered material properties and feData, with damaged elements, was returned to DEGEN. The iterative portion of DEGEN then began, with a new analysis

performed with the damaged material properties. This iterative loop continued for as many iterations as the user specified, or could be set to terminate if an analysis resulted in no additional damaged nodes.

Two different crack geometries were tested in the degeneration simulation, using two different damage laws. The geometries used were the baseline crack from the previous section and the model with two cracks separated by 0.5 mm. The first damage law consisted of a damage threshold of 0.1 mm/mm compressive strain, with the effect of 10% decreased modulus and 10% increased permeability. The 0.1 mm/mm damage threshold was approximately twice the magnitude of the highest compressive strains seen in the uncracked model and the 10% change in material properties is a reasonable (even conservative) change based on the on the material property changes seen in Chapter 3. The second damage law was identical to the first, except that shear strain was used as the variable of interest, instead of compressive strain. In order to more easily track material property changes and verify that the algorithms were operating as intended, only 10 depth-wise layers of cartilage properties were used in these simulations.

Results

Ten iterations of the single baseline crack model were run under both the shear and compressive strain damage laws. Figure 82 shows the damage accumulated over the course of the 10 iterations, in terms of the reduction in material stiffness. Under identical loading, with identical cracks, dramatically different damage patterns occurred. The shear strain damage law resulted in minimal damage in the vicinity of the crack, with the damage concentrated near the subchondral plate. Under the shear law, damage would be likely to occur in the same location in an uncracked model, as the shear strains are equally high. This illustrates that it may be more realistic to define future damage laws in terms of a change in strain relative to an uncracked model. Under the compressive strain law, a very plausible damage pattern occurred. Damage was concentrated along the

crack faces and spread slowly away from the crack. The localization of the damage along the entire crack faces, versus concentration at the crack tip, is consistent with cell death patterns reported around cracks [146].

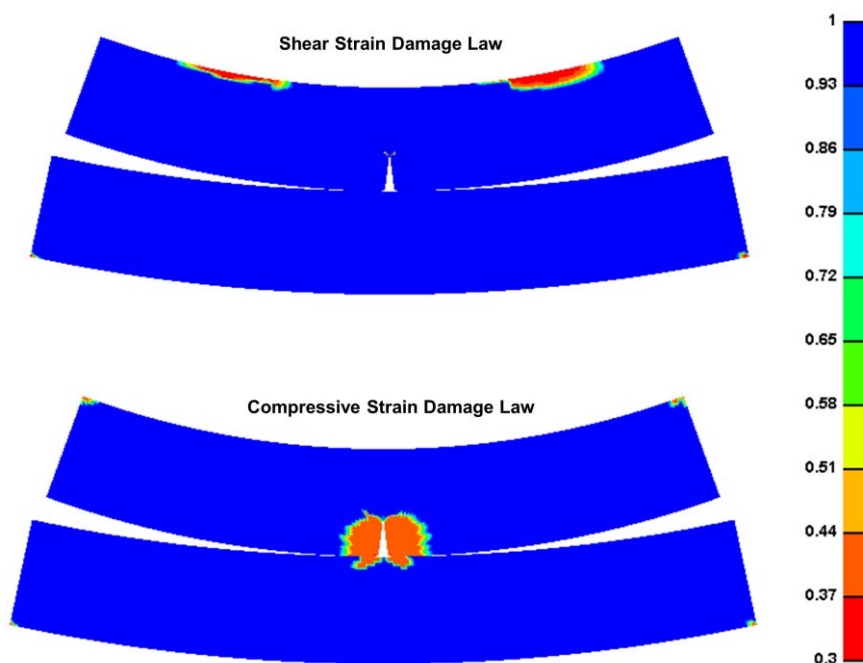


Figure 82. Damage distributions for baseline crack under a shear strain damage law and a compressive strain damage law, after 10 iterations. 1 = normal cartilage, 0.75 = material property stiffness reduced to 75% of normal.

Figure 83 shows the change in the compressive and tensile strain fields along a path 100 μm below the articular surface of the femur. Pore pressure and shear strain were effectively unchanged between iteration 1 and iteration 10 under both damage laws, and are therefore not plotted. Virtually no change in the strain fields was seen under the shear damage law, which is consistent with the absence of damage along the crack faces in that model. The damage accumulated under the compressive strain law invoked significant changes in the local strain field. The region of high compressive strain

became slightly wider as the damage progressed, and, more strikingly, the peak compressive strain increased approximately 40%. A localized 50% increase in tensile strains occurred following damage propagation under the compressive strain law. Figure 84 shows the tensile strain distributions in the 1st and 10th iteration of the model, highlighting the dramatic difference the damage propagation could inflict.

The degeneration simulations with two cracks result in outcomes very similar to the single baseline cracks (Figure 85). Again, the shear strain damage law resulted in very little degeneration near the cracks, and none along the crack face. Under the compressive strain law, damage occurred along the entire crack face, and the entire area between the crack experienced significant damage over 5 iterations. It is interesting to note that the damage filled in between the cracks and extended outward, but did not extend any deeper into the cartilage than the crack tips. There was again a marked increase in compressive and tensile strains 100 μm below the articular surface (Figure 86).

The damage laws used in this section are simple examples used to test the degeneration algorithm and demonstrate its capabilities. The results of this testing suggest additional changes to be considered in hypothesizing new damage laws. As previously mentioned, defining the damage law with a threshold relative to an uncracked model takes into account cartilage's potential susceptibility to altered loads due to the crack, rather than simply to absolute strain magnitude. Other reasonable considerations would include relating the damage effect magnitude to the strain magnitude (i.e. perhaps a 0.2 mm/mm strain causes more damage than a 0.15 mm/mm strain), or setting a lower floor that represents the "most degenerated" state cartilage is allowed to reach. As more complicated loading is added, it may be reasonable to add an exposure term to the damage law, such that nodes that experience damaging loading over a longer period register more damage than those only briefly overloaded.

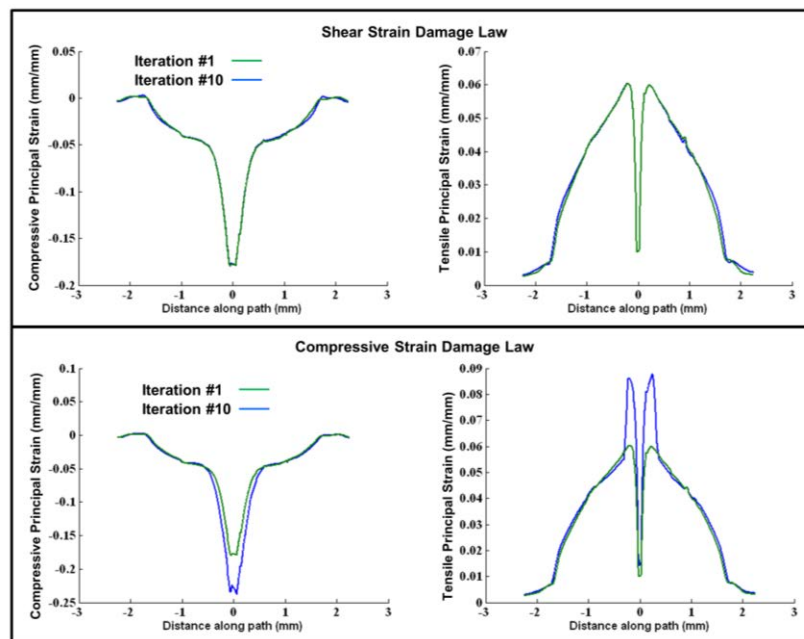


Figure 83. Comparison of compressive strains and tensile strains following 10 damage propagation cycles under shear and compressive strain damage laws. Line plots are extracted from path 100 μm below the articular surface.

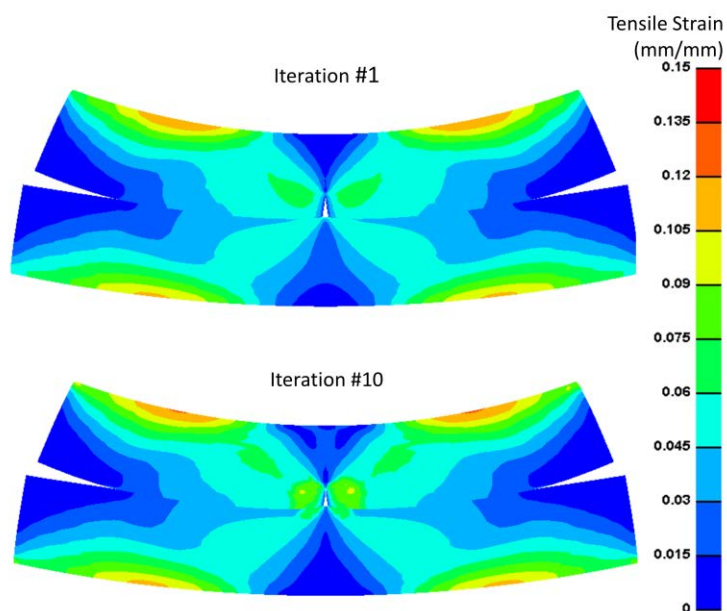


Figure 84. Tensile strains before and after 10 iterations of degeneration simulation under the compressive damage law.

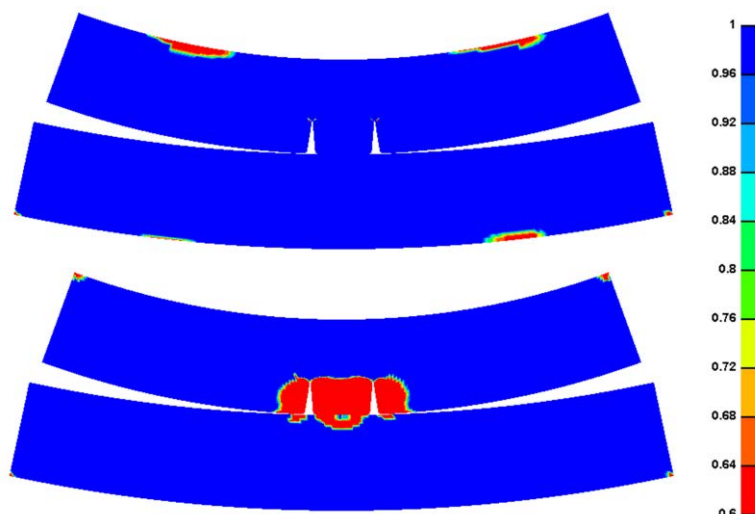


Figure 85. Damage distributions for two baseline cracks separated by 0.5 mm under a shear strain damage law and a compressive strain damage law, following 5 iterations. 1 = normal cartilage, 0.75 = material property stiffness reduced to 75% of normal.

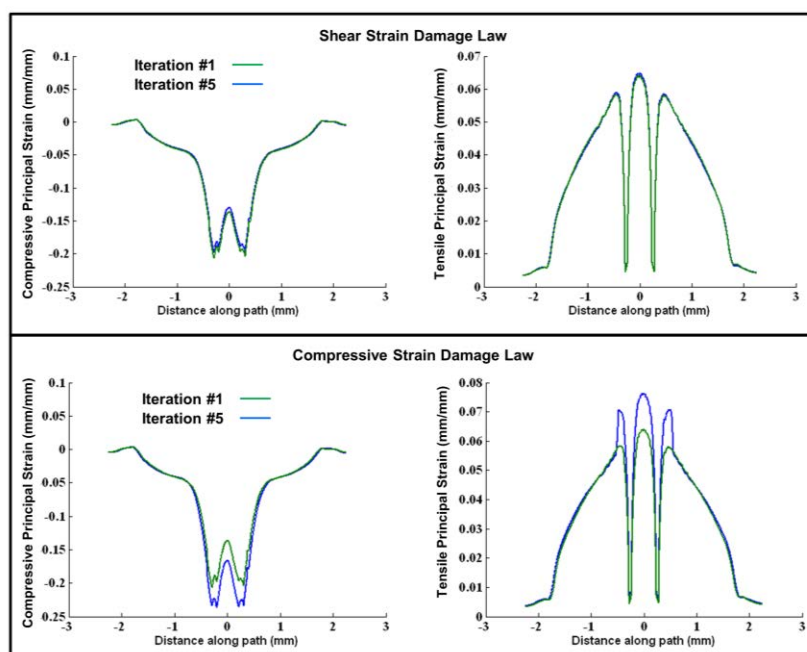


Figure 86. Comparison of compressive and tensile strains following 10 damage propagation cycles under shear and compressive strain damage laws. Line plots are extracted from path 100 μm below the articular surface.

CHAPTER 6. DISCUSSION

This dissertation work involved developing a variety of computational tools to complement a multi-disciplinary approach to post-traumatic osteoarthritis research. The tools developed have been used to guide experimental procedure, to analyse and interpret experimental output, and to provide insight into PTOA development through stress and strain distributions that could not be measured experimentally.

The impact models represent, to the author's best knowledge, the first finite element models of cartilage impact based on and validated by experimental results. A pair of papers from Garcia et al. purports to derive elastic properties for cartilage impact from indentation tests, but the reported stresses range from 0.33 to 5 MPa, which is obviously far below the loads defined as impacts by Aspden et al. [23]. Similarly, Donzelli et al. developed a finite element model of biphasic cartilage contact to investigate correlations between stresses and tissue failure [156]. Again, however, the peak stresses reported in that paper never exceed 600 *kPa*. This is obviously far below even normal physiologic loading, and therefore the relevance of that material model to true impact loading is questionable.

Atkinson et al. reported finite element modeling of drop-tower cartilage impacts similar to the experiments described in Chapter 2 [157]. They used an incompressible linear elastic material model with a modulus of 20 MPa to simulate impacts with three different sizes of spherical impactors. No validation of this material model was reported. Elastic moduli based on the stress-strain curves in Figure 7 would range from 70 MPa to 150 MPa, although the work in Chapter 2 involved higher impact energies than that of Atkinson et al. Following their experimental and computational impacts, Atkinson et al. took the interesting step of performing logistical regression between a variety of stress and strain measures and the incidence of cartilage fracture. They found that shear stress had the highest predictive capability for fracture; however, principal stress and strain,

mean stress, and cohesive strength also had statistically significant predictive capabilities. This highlights the difficulty of separating the mechanical signals that may drive cartilage degradation. Nonetheless, the current impact material model, combined with continued ongoing impact testing, provides an ideal data set to perform similar analysis on a larger scale. Since the thickness of each impact is routinely recorded from ultrasound measurements, specimen-specific impact models could be performed and the resultant stress and strain fields could be compared with the histologically apparent structural damage.

The careful assessment of cartilage structural damage represents an as-yet-untapped resource of information related to the degradation of cartilage. For instance, the results of the rabbit PTOA model assessment presented in Chapter 3 provide compelling quantitative evidence that cartilage structural damage does not evolve or change significantly between 8 weeks and 16 weeks in that model. The comparisons between PTOA models demonstrate the differences in damage that would be expected from the lower intensity instability injury versus a highly focused and more overtly damaging defect injury. Comparing the structural damage resulting from various PTOA models could be an important application of the crack morphology program in the future. Studies of osteoarthritis in literature include rabbit [60], mouse [158], porcine [67], canine [159], ovine [160], feline [161], equine [162], and hamster models [163]. Just as biologic similarity should be established before extrapolating animal model results to human expectations, the similarity of the occurrence and progression of mechanical damage should be verified. In particular, factors such as cartilage thickness, collagen composition and orientation, and water content vary between species and may affect the resulting mechanical damage. Similarly, a vast array of experimental protocols has been used to invoke cartilage degeneration. Even within impact models, procedures have included drop-towers and pendulums, have involved direct contact on exposed cartilage and indirect contact through adjacent bone, and have used widely varying impact

energies. Current methods to evaluate mechanical damage in cartilage involve highly subjective ‘spot-checking’ of histology slides. The automated quantification of crack morphology provides an objective means to evaluate the actual amount of damage invoked in the cartilage.

Further applications of the crack morphology program as more histology from impacted specimens becomes available will be informative. The initial rounds of histology from the study were complicated by trephine cuts related to obtaining tissue for biochemical assessment. The protocol has since been changed so that histology is free of such cuts. Folding the structural damage characteristics into the dataset presented in Chapter 4 will be very informative. As discussed in that chapter, the mechanism behind the changes in poroelastic material properties is not clear. Objective quantification of the structural damage in those specimens will establish whether the material property changes are intrinsic changes in the tissue, or the results of structural weakening due to the formation of cartilage cracks. Furthermore, as (recently begun) repetitive loading tests of the bovine explants are completed, structural damage assessment will establish how cartilage cracks evolve following two weeks under a variety of dynamic loading conditions.

The results determined thus far from the indentation of impacted cartilage already yield interesting insight. The time-course of material properties changes, spanning the timeframe from immediately post-impact to two weeks post-impact is unreported in literature. Blumberg et al. demonstrated significantly decreased modulus at 1 and 2 weeks post-impact, and increased permeability at 2 weeks post-impact, but there are no immediate post-impact time-points [164]. Haut et al. found reduced shear moduli in impacted rabbit knees, but found no difference between rabbits that were tested at 1, 3, 6, or 14 days, although this was likely hindered by having only 3 specimens per timepoint [165]. Borrelli et al. demonstrated a time-course of cartilage softening 1 month after impact, then regaining some stiffness by 6 months [60]. In a blunt impact rabbit survival

model, Isaac et al. demonstrated an increase in cartilage stiffness (increased modulus and decreased permeability) from 6 months to 12 months [62]. Relative to these studies, the results from this study demonstrate early-stage changes in cartilage following impact.

The array of studies presented above (as well as many others not specifically discussed here) does not paint a particularly coherent picture of the progression of degeneration. Some studies demonstrated cartilage softening while others result in stiffening, and the time-points are scattered from days to months. A variety of different mechanisms are likely at work in these studies. For instance, the cartilage softening and re-stiffening reported by Borrelli et al. is likely well into a cartilage-remodeling phase and may represent a different mechanism than that observed in more acute timeframe studied in Chapter 4. This highlights the importance of correlating mechanical property changes with biochemical outcomes as well as compositional changes. Half of the specimens impacted are routed through biochemical analysis (the other half go to histology), in which proteoglycan (PG) and proline content are measured. Figure 87 shows the results of these biochemical assays. Although the number of specimens is currently low, the results suggest little change in PG content within the first two weeks. This is consistent with histology results in which little difference in safranin O staining is seen between unimpacted specimens and 1 week and 2 week specimens (Figure 88). Proline content, however, appears to increase substantially by 1 week post-impact, and then decrease slightly by 2 weeks. Proline is primarily responsible for collagen content. The increased proline content at 1 week post-impact may then indicate that repair of damaged collagen is occurring, which would explain the recovering elastic modulus around the same timepoint (Figure 87c). The non-recovery of modulus following the higher energy (3.09 J/cm^2) metal-on-cartilage impacts, as previously shown in Figure 52, may indicate that collagen fibrils are broken, or at least strained beyond repair, in these impacts. Of the three high-energy impact specimens that have had histology preparations so far, all of them display cartilage fracture (Figure 89). Unfortunately, at the time of this

writing, no biochemistry was available for the 1 day specimens, where the largest change in material properties was seen.

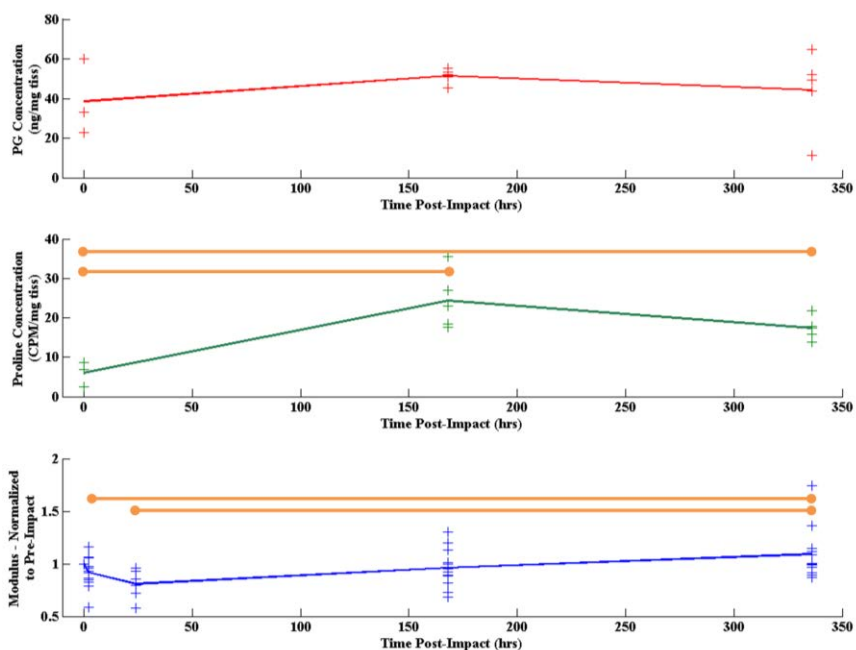


Figure 87. Time course of proteoglycan and proline content compared to that of elastic modulus following 2.18 J/cm^2 metal-on-cartilage impact. Horizontal bars show statistically significant differences ($p < 0.05$).

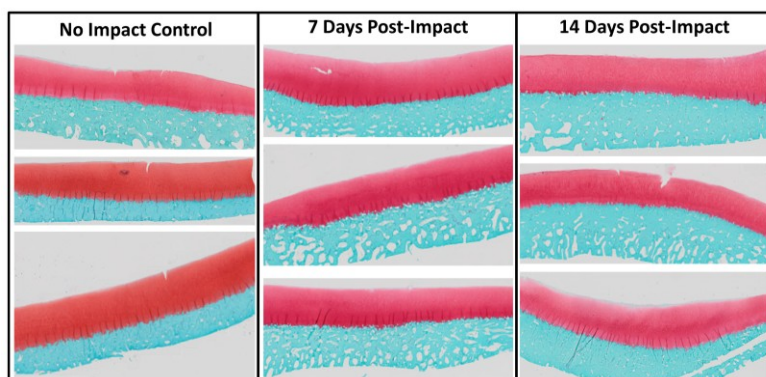


Figure 88. Representative histology from unimpacted control specimens and 7 days and 14 days following impact with 2.18 J/cm^2 .

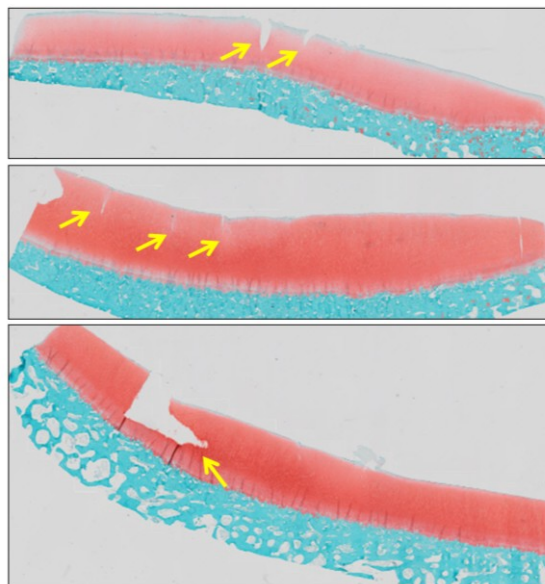


Figure 89. Histology of specimens impacted with 3.09 J/cm^2 . Arrows highlight structural damage.

Much of the discussion to this point has focused on the effects of acute cartilage damage, that is, cartilage change inflicted by a single impact. Of course, in a clinical setting, PTOA develops in response to both an acute injury (ACL rupture, intra-articular fracture, etc) and subsequent normal and abnormal loading during normal activities. Both the intensity of the initial injury [87, 88] and residual abnormal stresses following the injury [73, 98, 99] have been implicated in PTOA development, although the exact mechanisms driving this process are not fully understood. The cartilage crack models were developed to investigate the possibility that cartilage cracks serve as nucleation points, around which localized chondrocyte death occurs and begins to spread. The results of those models demonstrated that the presence of a crack had a substantial effect on the local strain environment, causing peak strains to rise from 5% to well over 15%. This is higher than the 10% strains shown to invoke cartilage degeneration by both Thibault et al. and Torizilli et al [51, 55]. The size or depth of the crack had relatively little influence on the strain fields; however, the presence of multiple cracks in close

proximity had an additive effect. This supports the possibility of a threshold of structural damage below which cartilage may be able to stabilize and remain healthy. Cartilage subjected to more than this threshold of damage would then be disposed to degenerate and wear quickly.

One of the major challenges in finite element modeling is interpreting the true physiologic relevance of stress and strain output. To date, there are no unifying theories defining what levels of stress or strain are damaging to cartilage, so finite element models are limited to generalizations such as “condition B is worse than condition A”. The iterative degeneration model attempts to begin to bridge that shortcoming, by providing a framework in which cartilage damage theories could be tested. The concept is not without precedence, as Duda et al. attempted to determine the effects of mechanical conditions on defect healing using adaptive material properties [166]. There does not appear to be significant follow-up to that paper in literature. A similar procedure has also been used to model bone resorption and adaptation [167], and the present iterative algorithm is inspired in part by adaptive meshing implant wear modeling [168-170].

The initial tests completed with the degeneration model demonstrate its capabilities. If cartilage degeneration does spread from local cartilage cracks (admittedly, this has not been proven and is only theoretical at this point), shear strain would not appear to be the likely candidate driving that propagation, as alterations in material properties do not match known cartilage damage patterns. On the other hand, compressive strain may be very significantly involved, as compressive strains are localized in the more superficial layers of cartilage, and the damage propagates out from the crack faces to encompass progressively larger areas of cartilage. In the two-crack models, compressive strain is again strongly implicated. Damage accumulates very quickly in the area between the two cracks.

Limitations

As with all finite element studies, as well as with reductionist experimental studies, there are a variety of limitations which must be addressed. Most of the experimental portion, with the exception of the rabbit histology slides used in Chapter 3, is based on cartilage explants. This has advantages over survival animal models, including reduced cost, easier storage, and greatly improved experimental control. However, working with explants ignores some of the systemic effects that may play a role in degeneration, and requires simplification of the loading regimes compared to physiologic loading. Also, as addressed in Chapter 2, most of the impacts are performed with metal platen impactors, differing from the cartilage-on-cartilage contact of actual joints. However, since the cartilage-on-cartilage impact requires cutting a new impact platen for each impact, the metal platen saves significant time in experimental set-up and eliminates one source of variability (material properties of the cartilage platen).

An additional shortcoming related to the laboratory experiments is data sparsity. While a large amount of very valuable data has been generated, there are key points where an as-yet-uncompleted experiments prevent more thorough analysis. The primary example of this is the previously-mentioned lack of biochemistry in the one day post-impact specimens. In addition, increasing the number of no-impact biochemistry results would allow for robust statistical analysis, and adding biochemistry at the immediate post-impact timepoint would allow for a comparison of complete time-courses in both biochemistry and mechanical properties. Confocal data (showing chondrocyte function in the superficial layers) are being collected, but have not been integrated into the current dataset. Table 5 shows the current specimen counts for the datapoints being collected, and highlights opportunities for high-yield results from relatively few additional specimens. In addition to the tests highlighted below, analysis of additional specimens impacted at the higher energy (3.09 J/cm²), including indentation and biochemistry at one

day post-impact, would strengthen conclusions regarding the impact and repair threshold process of cartilage.

	Pre-Impact	2 hrs Post-Impact	1 Day Post-Impact	1 Week Post-Impact	2 Weeks Post-Impact
Impact	--	--	6	11	10
Mechanical	32	14	6	14	12
Biochem	3	0	0	5	5
Confocal	*	*	*	*	*
Histology	6	3	6	8	6

Impact = Max. stress, stress rate, etc.

Mechanical = Modulus, permeability, etc.

Biochem = PG and Proline

Confocal = Cell viability measures

Histology = Safranin O and MMP 3

Notes: Impact data are categorized according to the timepoint at which the specimen was sent to biochem or histology.

Some confocal data have been collected, but have not been added to the master database of results. Yellow boxes highlight locations where ~5 additional specimens may yield new insight or strengthen existing analysis.

Table 5. Current specimens counts for cartilage explant impact series.

Limitations also exist relevant specifically to the finite element models presented here. Obvious questions arise about the need for three separate material models. Ideally, using the same material models for all three types of simulations would allow for more direct comparison of results between the simulations. Unfortunately, several factors discourage this. The dynamic explicit formulation used in the impact model is necessary given the high deformation and extremely short time-scale (< 5 ms) of the analysis. However, poroelastic analysis is not available in Abaqus Explicit (or in any explicit formulation), and the assumptions relating the pressure stress term to the pore pressure are valid only for short-term loading. Therefore the indentation and crack models must be performed in different analysis environments. It would be theoretically possible to perform the indentation analysis using the depth-dependent material model developed for

the cartilage contact models. However, the cartilage-on-cartilage contact models must be performed in FEBio, as that package is the only one currently available which properly handles the interface between two poroelastic materials. FEBio is strictly three-dimensional modeling software, so to port the indentation models to FEBio would require the optimization algorithm to work on quarter-models involving thousands of 8-node elements. Material properties have been determined for over 600 indentation tests to date, with 50+ model evaluations performed for each optimization, resulting in a (conservative) estimate of 30,000 finite element model evaluations. This has proven to be reasonably feasible for the axisymmetric indentation models, which run on the order of 30 seconds each. But, extending the model to a three-dimensional simulation would make the process intractably time-consuming. Finally, for the purposes of comparing indentation data with other published data, it was attractive to maintain a model relatively close to the basic poroelastic model, despite that model's documented shortcomings (including the inability to support physiologic-level loads).

Despite the considerable effort expended developing a depth-dependent cartilage model in Chapter 4, the impact model developed did not include depth-dependent properties. This choice is made due to the lack of data about depth-wise variation of material properties *at impact speeds*. A substantial discontinuity exists between cartilage behavior at physiologic loading rates and its behavior at impact loading rates, as evidenced by the nearly linear stress-strain curves in Park's 40 hz loading rate data and the highly non-linear stress-strain curves observed in Chapter 2 (Figure 1 and Figure 4, respectively). Because of this, it seems tenuous at best to extrapolate physiologic-rate depth-dependence to impact-rate loading conditions. Furthermore, the single study that evaluated depth dependence of material properties under very high loading rates actually found no depth-wise variation at 200%/s strain [151]. Unfortunately, validating the through-thickness strain fields of the impact model seems nearly impossible.

An additional limitation of this project involving validation is the lack of validation for the crack model. The depth-dependent material model has been validated versus various results available in literature, but the strains within the actual crack model have not been validated, nor has the crack closure behavior. This problem is seemingly surmountable, through the use of a scalpel-created idealized ‘crack’ and arthroscopic imaging under loading. Flourescent-labeling of the surface would allow visualization of the crack closure mechanism, while labeling of chondrocytes may provide enough resolution to approximate strain fields local to the crack. In fact, the procedure used by Stok and Oloyede to study cartilage crack growth would be almost perfectly suited to validation of the crack model [171].

The damage laws tested in the degeneration model, while seemingly reasonable, are not explicitly grounded in any experimental testing. While this is a limitation, it is also an opportunity. Given the vast array of measures that may dictate cartilage degeneration (stress and strain components and invariants, stress and strain rates, fluid pressure and flow, etc.), the degeneration model provides a method to evaluate whether a theoretical damage law would be likely to cause propagating damage in experimental loading, before conducting the actual experiments.

The assessments of mechanical damage performed in Chapter 3 have a series of limitations due to their base in histology. The histology slides represent only a single slice through each compartment, so the slide may not reflect the damage across the entire joint surface. To minimize missing important damage, the location of the slice was chosen to be through the weightbearing regions, where the most damage would be expected. In addition, no information is known about the out-of-plane shape of the cracks. Both of these factors should affect all specimens equally, minimizing their influence in the conclusions drawn, and both are drawbacks common to all histologic assessment. Finally, there are concerns with histology artifact. In some slides, obvious folding or tearing of the section is visible, raising the possibility that some of the

quantified 'cracks' may be less-obvious tears created during processing. Histology sections are also prone to swelling and bending, which may compromise the absolute crack morphologic parameters assessed. Chapter 8 will detail ongoing work attempting to quantify the effect of these limitations. Despite these limitations, the program returns more detailed and objective information than was previously available through subjective viewing of histology.

CHAPTER 7. CONCLUSIONS

A suite of computational tools have been developed to further research into post-traumatic osteoarthritis. These tools help to clarify the mechanisms involved in initiating and propagating cartilage degeneration.

A finite element model for cartilage impact has been created and validated under different impact conditions. These models have verified that cartilage-on-cartilage and metal-on-cartilage vary only in the magnitude of the resulting strain, not in the distribution. The impact finite element models also provide the opportunity to compare strain distributions to cell death patterns. Shear strain and tensile strain both appear to correlate with the non-uniform percentage of cell death seen under the impactor. There is now also the possibility of comparing cartilage cracks with the corresponding impact strains.

An image-processing program was written to quantify the morphology of structural damage in cartilage histology. The program was demonstrated to have good inter- and intra-operator reliability. Differences in cartilage damage between different rabbit PTOA models were detected, with the more acute osteochondral defect insult resulting in more numerous and more severe cartilage cracks than an ACL rupture. Interestingly, no progression of structural damage was identified between 8 weeks and 16 weeks. Future work should focus on comparing the mechanical damage in impacted versus repetitively loaded osteochondral defects. This will help elucidate whether structural cracks observed in histology of osteoarthritic cartilage are representative of the amount of damage done in the acute injury, or of the accumulated damage following daily abnormal loading. This program represents a substantial advance in histology assessment compared to the prevailing standard of qualitative observations.

A Matlab- and Abaqus-based optimization algorithm was developed to determine cartilage poroelastic material properties from indentation tests. Careful modifications

were made so that the algorithm returns unique material properties regardless of the optimization starting point. Impacting cartilage with 2.18 J/cm^2 through a metal impactor caused an immediate increase in permeability and decrease in modulus, both of which recover to nearly pre-impact levels within two weeks. Biologic testing suggests that the modulus changes were due to collagen fibril damage that is then repaired. Impacting with higher energy caused material softening that did not return to normal, suggesting an impact injury threshold below which cartilage had some ability to repair itself.

A cartilage material model was developed which reflects the depth-dependence of cartilage material properties, and which is accurate at a range of loading conditions over the span of normal and elevated joint loading. This depth-dependent material model was then used to model the effect of several different crack geometries on the surrounding strain and pore pressure distributions. The presence of a single crack was highly disruptive to the strain fields, but the particular shape or size of that crack had little effect. The most detrimental perturbations included two cracks within close proximity. Once two cracks are within 0.5 mm of one another, the strain field between them increases in an additive fashion, suggesting a threshold for the amount of structural damage cartilage can withstand without being severely overloaded.

Finally, the crack finite element models were incorporated into an iterative simulation of cartilage degeneration. Testing under two different hypothetical damage laws demonstrated a higher likelihood for compressive strain to cause cartilage degeneration consistent with published reports of cell death. In the presence of two cracks, the propensity for damage due to compressive strain is very high in the isolated region between the cracks, but the damage does not extend deeper into the cartilage than the crack tips.

An overall mechanism of cartilage damage and degeneration can be hypothesized from the individual observations of these four (sometimes seemingly disparate) sub-projects. During sufficiently high-energy impact, collagen fibrils are strained beyond

cartilage's ability to repair them, some even to the point of gross cartilage fracture. Under repetitive loading, these cartilage cracks may not progress any deeper into the cartilage; however, their presence may sufficiently undermine the local fluid load support that excessive matrix strains occur, causing additional chondrocyte dysfunction. As the chondrocytes cease production of proteoglycans, cartilage loses more of its stiffness, exposing more chondrocytes to deleterious loads and allowing the spread of cartilage degeneration to a full-joint phenomenon. Of course, the preceding statements involve significant conjecture, but the programs and simulations developed in this Ph.D. project provide the tools to test, refine, and eventually validate such conjecture.

CHAPTER 8. ONGOING AND FUTURE WORK

The majority of this Ph.D. project focused on developing computational tools related to post-traumatic osteoarthritis research. The results of initial applications of all of these tools have been presented, but many additional uses are planned. This section highlights additional projects which are in progress, planned for the near future, or that warrant consideration for future grant submissions.

Impact and indentation

The impact and indentation testing is an ongoing work-in-progress. The largest set of data so far, as discussed in Chapters 2 and 4, involves impacting cartilage and performing a variety of tests over the following 1 to 14 days. A second set involving repetitive loading has only recently gotten underway. In that set, the cartilage is not impacted, but is subjected to one of three repetitive loading regimes, representing normal, unstable, or incongruous joints. Indentation testing and biologic and histologic assessment will be performed at similar intervals to the impact loaded tests, which will provide insight into the effects of chronic, versus acute, injury on cartilage degeneration. A third data set will involve both impact loading and repetitive loading, to determine possible synergistic effects. In this third set, one interesting outcome will be whether the repetitive loading prevents the recovery of properties seen following the 2.18 J/cm^2 impact.

In addition, as more histology becomes available from the impacted and repetitively loaded specimens, the structural damage in these specimens can be assessed using the program developed in Chapter 3. This will provide more objective information about the severity of the impacts, how that relates to mechanical and biologic changes, and the progression of damage under repetitive loading.

Structural Cartilage Damage

Histology artifact

As discussed in the Limitations section of Chapter 6, there are concerns regarding the effect of artifacts from histology processing on the accuracy of the derived structural damage metrics. Ongoing work is piloting methods to quantify the amount of histologically-apparent damage that may actually be processing artifact. In this pilot work, wheat germ agglutinin (WGA) is used to stain the surface of a cartilage explant after impact, but before histology is begun. WGA is a large molecule that will not penetrate far into the cartilage, so it can serve to highlight the surfaces it is applied to. WGA also binds to proteoglycans, so there is not a risk of it washing off during processing, unlike India ink, which was also considered. The WGA itself is not visible, so it is labeled with one of several chemicals that will be apparent in histology. By staining the exposed surface after impact but before histology, it should be possible to identify cracks created during processing as those without WGA staining.

Initial tests of the WGA were performed on two cartilage specimens impacted similarly to the procedure in Chapter 2. Before committing to the more labor-intensive histologic preparation, half of each specimen was cryosectioned. The resulting slides (Figure 90a) demonstrated promising results, and so the remaining halves of the specimens were sent through normal histologic preparation. These slides (Figure 90b) again demonstrated reasonable results, with the articular surface highlighted by a thin black line and with evidence of free-surfaces unstained by WGA, which were presumably created during histology processing. In the cryo-sectioned slides, there are large areas of the cartilage free surfaces with WGA labeling, indicating impact-induced damage. An additional opportunity to test WGA came from the cartilage-on-cartilage impacts described in Chapter 2. The cartilage plugs from those impacts were coated with WGA and processed for histology (Figure 90c). Histology on the impacting plugs was

discontinued after 2 impacts (it was felt that the information gained from histology of the plugs was not substantive enough to justify the time and labor necessary to process the slides). Recently, two more cartilage osteochondral explants have been harvested and impacted exactly as in Chapter 2, except that WGA was applied prior to histology. These specimens are currently in-process.

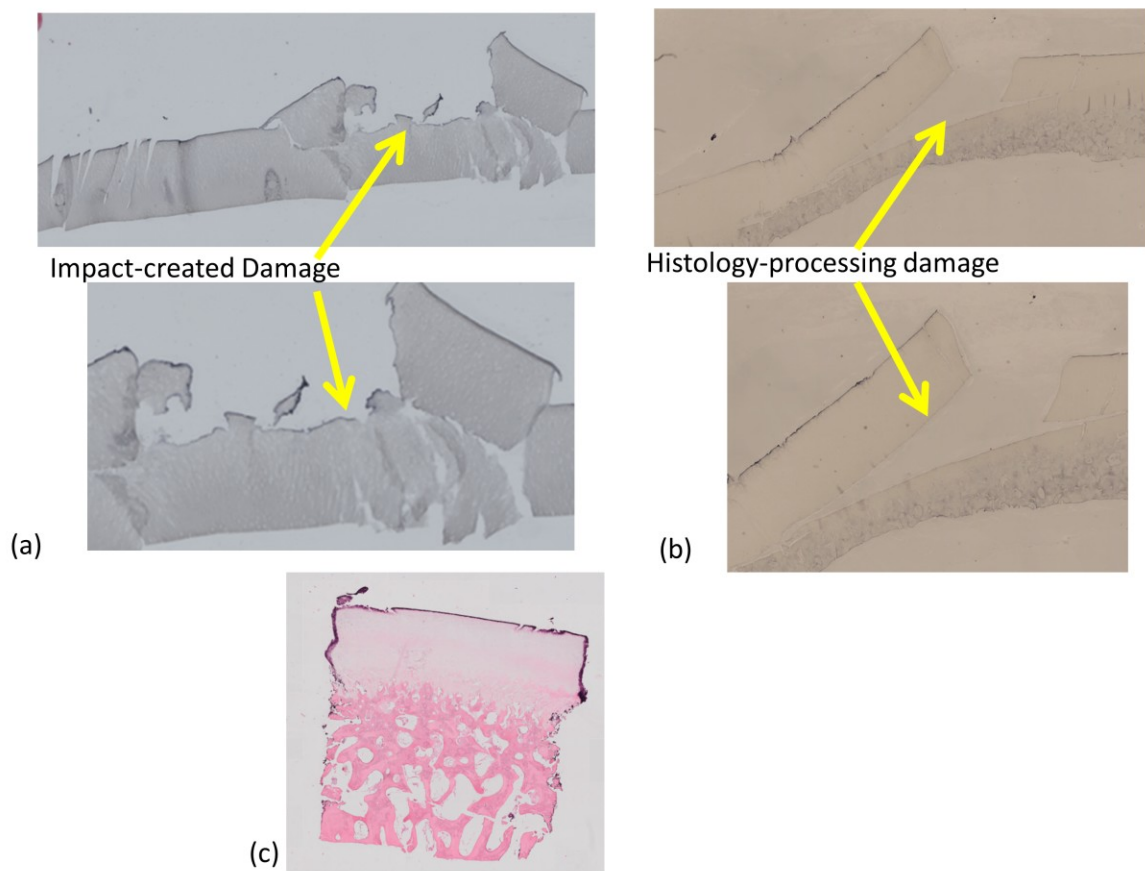


Figure 90. Sample of WGA staining of impacted cartilage. WGA outline suggests impact-induced damage in (a), while the unstained edges in (b) suggest post-stain histology processing damage. (c) Cartilage plug with no significant damage shows visibility of WGA versus a counter-stain.

Additional database sources

One of the stated goals of the structural damage assessment was to develop a database of crack morphology for the purposes of comparing damage from various *in vitro* models, animal models, and clinical histology. The data presented in Chapter 3 represent two variants of an animal model. The ongoing impact and repetitive loading studies will provide data for *in vitro* models, as that histology becomes available. Recently, colleagues at the Cleveland Clinic provided approximately 70 histology slides from their rabbit impact models, which will be a valuable complement to the rabbit PTOA and osteochondral defect models developed in-house. Finally, a small (~9 at present) set of slides are available from amputation and arthroplasty patients. Processing the structural damage in all of these slides remains a high priority.

Crack modeling and degeneration simulation

As discussed in the Limitations section, the crack finite element models require experimental validation to increase confidence in their behavior. In addition, the value of these models will increase when coupled with more rigorous assessment of matching histology. There have been discussions regarding calculating the change in cell density visible in histology in the vicinity of cracks. This would allow for the direct, objective comparison of altered stress and strain environments with abnormal cell density. Performing this analysis on both the repetitively loaded specimens and the impact-only specimens would clarify the contribution of acute and chronic loading to cell death around cracks.

The iterative degeneration simulation algorithm provides a generalized framework for future studies of cartilage degeneration. The program is not specific to the crack finite element models and could just as easily be applied to any arbitrary geometry and loading (within the ability of FEBio to model such loading). Several potential alternatives to the damage laws tested have already been proposed. Validation of a

damage law would be performed under more controlled loading of cartilage explants. This would ideally be an iterative process with finite element modeling identifying loading modes that would isolate, to the extent possible, certain stress or strain parameters, followed by experimental testing including monitoring of cell death and indentation testing, and finally degeneration simulations to replicate the observed cartilage changes. Furthermore, it is conceivable that biologic effects, such as drug treatments, could be incorporated into this simulation algorithm, with proper mathematical modeling. The recent integration of the solute transport theories developed by Ateshian et al. into FEBio makes combined mechanical and biologic modeling very tractable and attractive.[172, 173]

APPENDIX. DEPTH-DEPENDENT MATERIAL PROPERTIES

Symbols**Properties:**

Et - tensile modulus, Ec - compressive modulus, ν - Poisson's Ratio, G - shear modulus, k - permeability, t - thickness

Orientation:

* Where relevant, directions are in reference to excised cartilage plugs.

* Pairs of directions, such as 'rz', refer to anisotropic Poisson's ratios, where the first direction refers to the direction of the applied stress and the second gives the direction of the resulting strain.

z - normal to articular surface, r - parallel to articular surface in radial direction, theta - parallel to articular surface in circumferential direction, par - parallel to split lines (parallel to articular surface), perp - perpendicular to split lines (parallel to articular surface)

Highlighted entries are included in final depth-wise trends

Studies were excluded from the final trends for the following reasons:

(P): Tested property not used in material model

(S): Testing speed outside of range of interest

(D): Testing direction not of interest

Paper	Property	Orientation	s-e region	Speed	Position	Value
{Authors; Journal; Year}	{Et, Ec, v, G, k, t}	{z, r, theta, par, perp, r-theta, rz, zr...}	{toe, linear}	{static, dynamic, high-speed}	{0...1}	
Elliot et al.; J Biomech; 2002	Et	r	toe	static	0.33	5.81
Elliot et al.; J Biomech; 2003	Et	r	toe	static	0.67	1.92
Elliot et al.; J Biomech; 2004	Et	r	linear	static	0.33	23.92
Elliot et al.; J Biomech; 2005	Et	r	linear	static	0.67	3.18
Elliot et al.; J Biomech; 2006 (D)	ν	r-theta		static	0.33	2.38
Elliot et al.; J Biomech; 2007 (D)	ν	r-theta		static	0.67	0.7
Huang et al; J Biomech; 2005	Et	par	toe	static	0.33	6.57
Huang et al; J Biomech; 2006	Et	par	toe	static	0.67	3.55
Huang et al; J Biomech; 2007	Et	par	linear	static	0.33	36.53
Huang et al; J Biomech; 2008	Et	par	linear	static	0.67	14.89
Huang et al; J Biomech; 2009	Et	perp	toe	static	0.33	4.55
Huang et al; J Biomech; 2010	Et	perp	toe	static	0.67	2.24
Huang et al; J Biomech; 2011	Et	perp	linear	static	0.33	18.35
Huang et al; J Biomech; 2012	Et	perp	linear	static	0.67	8.71
Huang et al; J Biomech; 2013	Ec	z	toe	static	0.33	0.127
Huang et al; J Biomech; 2014	Ec	z	toe	static	0.67	0.16
Huang et al; J Biomech; 2015	Ec	z	linear	static	0.33	0.16
Huang et al; J Biomech; 2016	Ec	z	linear	static	0.67	0.189
Huang et al; J Biomech; 2017	k	z		static	0.33	1.14E-14
Huang et al; J Biomech; 2018	k	z		static	0.67	1.37E-14
Klein et al; J Biomech; 2007	Ec	z	toe	static	0.33	0.2
Klein et al; J Biomech; 2008	Ec	z	toe	static	0.67	0.35
Klein et al; J Biomech; 2009	Ec	z	toe	static	1.00	0.55
Laasanen et al; Biorheology; 2003	Ec	z	toe	static	0.33	0.2

Laasanen et al; Biorheology; 2004	Ec	z	toe	static	0.67	0.4
Laasanen et al; Biorheology; 2005	Ec	z	toe	static	1.00	1.75
Laasanen et al; Biorheology; 2006	v	rz		static	0.33	0.15
Laasanen et al; Biorheology; 2007	v	rz		static	0.67	0.37
Laasanen et al; Biorheology; 2008	v	rz		static	1.00	0.15
Tomkoria et al; Medical Engineering and Physics; 2004	Ec	z	toe	static	0.20	0.52
Tomkoria et al; Medical Engineering and Physics; 2005	Ec	z	toe	static	0.40	0.72
Tomkoria et al; Medical Engineering and Physics; 2006	Ec	z	toe	static	0.60	1.1
Tomkoria et al; Medical Engineering and Physics; 2007	Ec	z	toe	static	0.80	1.3
Tomkoria et al; Medical Engineering and Physics; 2008	Ec	z	toe	static	1.00	1.69
Akizuki et al; JOR; 1986	Et	par	linear	static	0.20	6.22
Akizuki et al; JOR; 1987	Et	par	linear	static	0.40	3.4
Akizuki et al; JOR; 1988	Et	par	linear	static	0.60	3.12
Akizuki et al; JOR; 1989	Et	par	linear	static	0.80	0.93
Akizuki et al; JOR; 1990	Et	par	linear	static	0.20	20.67
Akizuki et al; JOR; 1991	Et	par	linear	static	0.40	8.77
Akizuki et al; JOR; 1992	Et	par	linear	static	0.60	4.14
Akizuki et al; JOR; 1993	Et	par	linear	static	0.80	1.01
Kempson et al; Biochimica et Biophysica Acta; 1973	Et	par	linear	dynamic	0.17	80
Kempson et al; Biochimica et Biophysica Acta; 1974	Et	par	linear	dynamic	0.33	46.25
Kempson et al; Biochimica et Biophysica Acta; 1975	Et	par	linear	dynamic	0.50	21.65
Kempson et al; Biochimica et Biophysica Acta; 1976	Et	par	linear	dynamic	0.67	15.55
Kempson et al; Biochimica et Biophysica Acta; 1977	Et	par	linear	dynamic	0.83	10.9
Kempson et al; Biochimica et Biophysica Acta; 1978	Et	par	linear	dynamic	1.00	7.3
Kempson et al; Biochimica et Biophysica Acta; 1979	Et	perp	linear	dynamic	0.20	29.5
Kempson et al; Biochimica et Biophysica Acta; 1980	Et	perp	linear	dynamic	0.40	18
Kempson et al; Biochimica et Biophysica Acta; 1981	Et	perp	linear	dynamic	0.60	15.75
Kempson et al; Biochimica et Biophysica Acta; 1982	Et	perp	linear	dynamic	0.80	14.5
Kempson et al; Biochimica et Biophysica Acta; 1983	Et	perp	linear	dynamic	1.00	12.5
Roth & Mow; JBJS; 1980	Et	par	toe	static	0.33	10.63
Roth & Mow; JBJS; 1980	Et	par	toe	static	0.67	2.01

Roth & Mow; JBJS; 1980	Et	par	toe	static	1.00	0.75
Roth & Mow; JBJS; 1980	Et	par	linear	static	0.33	29.13
Roth & Mow; JBJS; 1980	Et	par	linear	static	0.67	3.75
Roth & Mow; JBJS; 1980	Et	par	linear	static	1.00	0.75
Roth & Mow; JBJS; 1980	Et	perp	toe	static	0.33	3.22
Roth & Mow; JBJS; 1980	Et	perp	toe	static	0.67	0.665
Roth & Mow; JBJS; 1980	Et	perp	toe	static	1.00	0.5
Roth & Mow; JBJS; 1980	Et	perp	linear	static	0.33	6.64
Roth & Mow; JBJS; 1980	Et	perp	linear	static	0.67	1
Roth & Mow; JBJS; 1980	Et	perp	linear	static	1.00	0.375
Boschetti et al; Biorheology; 2004	Ha	z	toe	static	0.33	0.26
Boschetti et al; Biorheology; 2005	Ha	z	toe	static	0.67	0.39
Boschetti et al; Biorheology; 2006	Ha	z	toe	static	1.00	0.5
Boschetti et al; Biorheology; 2007	v	rz		static	0.33	0.17
Boschetti et al; Biorheology; 2008	v	rz		static	0.67	0.24
Boschetti et al; Biorheology; 2009	v	rz		static	1.00	0.25
Boschetti et al; Biorheology; 2010	k	z		static	0.33	3.20E-14
Boschetti et al; Biorheology; 2011	k	z		static	0.67	1.80E-14
Boschetti et al; Biorheology; 2012	k	z		static	1.00	1.70E-14
Boschetti et al; Biorheology; 2013	E	z	toe	static	0.33	2.50E-01
Boschetti et al; Biorheology; 2014	E	z	toe	static	0.67	3.60E-01
Boschetti et al; Biorheology; 2015	E	z	toe	static	1.00	5.00E-01
Verteramo & Seedhom; Biorheology; 2004	Et	par	linear	dynamic	0.33	11.6
Verteramo & Seedhom; Biorheology; 2005	Et	par	linear	dynamic	1.00	6
Verteramo & Seedhom; Biorheology; 2006	Et	perp	linear	dynamic	0.33	8
Verteramo & Seedhom; Biorheology; 2007	Et	perp	linear	dynamic	1.00	2.5
Verteramo & Seedhom; Biorheology; 2008 (S)	Et	par	linear	dynamic	0.33	20
Verteramo & Seedhom; Biorheology; 2009 (S)	Et	par	linear	dynamic	1.00	20
Verteramo & Seedhom; Biorheology; 2010 (S)	Et	par	linear	high-speed	0.33	20
Verteramo & Seedhom; Biorheology; 2011 (S)	Et	par	linear	high-speed	1.00	20
Verteramo & Seedhom; Biorheology; 2012 (S)	Et	par	linear	high-speed	0.33	20
Verteramo & Seedhom; Biorheology; 2013 (S)	Et	par	linear	high-speed	1.00	20
Guilak et al; JOR; 1994	Et	par	toe	static	0.20	15
LeRoux et al; JOR; 2000 (P)	t	z			0.33	118.3
LeRoux et al; JOR; 2001 (P)	t	z			0.67	80
LeRoux et al; JOR; 2002 (P)	t	z			1.00	939
Buckley et al; J Biomech; 2008	G	zr	toe	static	0.20	0.15

Buckley et al; J Biomech; 2008	G	zr	toe	static	0.40	0.3
Buckley et al; J Biomech; 2008	G	zr	toe	static	0.60	0.35
Buckley et al; J Biomech; 2008	G	zr	toe	static	0.80	0.7
Buckley et al; J Biomech; 2008	G	zr	toe	static	1.00	1
Bae et al; OA & Cartilage; 2008	Et	par	linear	dynamic	0.33	30
Bae et al; OA & Cartilage; 2008	Et	par	linear	dynamic	0.67	12
Bae et al; OA & Cartilage; 2008	Et	par	linear	dynamic	1.00	5
Bae et al; OA & Cartilage; 2008	Et	perp	linear	dynamic	0.33	20
Bae et al; OA & Cartilage; 2008	Et	perp	linear	dynamic	0.67	8
Bae et al; OA & Cartilage; 2008	Et	perp	linear	dynamic	1.00	5
Bae et al; OA & Cartilage; 2008	Et	par	toe	static	0.33	12
Bae et al; OA & Cartilage; 2008	Et	par	toe	static	0.67	6
Bae et al; OA & Cartilage; 2008	Et	par	toe	static	1.00	3
Bae et al; OA & Cartilage; 2008	Et	perp	toe	static	0.33	9
Bae et al; OA & Cartilage; 2008	Et	perp	toe	static	0.67	3
Bae et al; OA & Cartilage; 2008	Et	perp	toe	static	1.00	2
Federico et al; J Biomech; 2005	E	z			1.40	0.722193
Federico et al; J Biomech; 2005	E	z			0.33	0.719417
Federico et al; J Biomech; 2005	E	z			0.67	0.716642
Federico et al; J Biomech; 2005 (D)	E	r			1.00	0.730519
Federico et al; J Biomech; 2005 (D)	E	r			1.13	0.727744
Federico et al; J Biomech; 2005 (D)	E	r			1.27	0.724968
Federico et al; J Biomech; 2005	v	rz			0.33	0.021
Federico et al; J Biomech; 2005	v	rz			0.67	0.23
Federico et al; J Biomech; 2005	v	rz			1.00	0.275
Federico et al; J Biomech; 2005	v	r-theta			0.33	0.146
Federico et al; J Biomech; 2005	v	r-theta			0.67	0.218
Federico et al; J Biomech; 2005	v	r-theta			1.00	0.275
Federico et al; J Biomech; 2005	v	z-theta			0.33	0.215
Federico et al; J Biomech; 2005	v	z-theta			0.67	0.218
Federico et al; J Biomech; 2005	v	z-theta			1.00	0.035
Federico et al; J Biomech; 2005	G	zr			0.33	0.182
Federico et al; J Biomech; 2005	G	zr			0.67	0.33
Federico et al; J Biomech; 2005	G	zr			1.00	0.105
Federico et al; J Biomech; 2005	G	r-theta			0.33	0.132
Federico et al; J Biomech; 2005	G	r-theta			0.67	0.338
Federico et al; J Biomech; 2005	G	r-theta			1.00	0.476
Chahine et al; J Biomech; 2004 (D)	Ec	par	toe	static	0.33	0.3
Chahine et al; J Biomech; 2004 (D)	Ec	par	linear	static	0.33	0.2
Chahine et al; J Biomech; 2004 (D)	Ec	perp	toe	static	0.33	1.2
Chahine et al; J Biomech; 2004 (D)	Ec	perp	linear	static	0.33	0.2
Chahine et al; J Biomech; 2004 (D)	Ec	par	toe	static	1.00	0.3
Chahine et al; J Biomech; 2004 (D)	Ec	par	linear	static	1.00	0.2
Chahine et al; J Biomech; 2004 (D)	Ec	perp	toe	static	1.00	1.2

Chahine et al; J Biomech; 2004 (D)	Ec	perp	linear	static	1.00	0.2
Chahine et al; J Biomech; 2004	Ec	z	toe	static	0.33	0.75
Chahine et al; J Biomech; 2004	Ec	z	toe	static	1.00	2
Chahine et al; J Biomech; 2004 (D)	Ec	z	linear	static	0.33	0.1
Chahine et al; J Biomech; 2004 (D)	Ec	z	linear	static	0.33	0.2
Chahine et al; J Biomech; 2004 (D)	v	par-perp	toe	static	0.33	0.21
Chahine et al; J Biomech; 2004 (D)	v	par-perp	linear	static	0.33	0.03
Chahine et al; J Biomech; 2004 (D)	v	perp-par	toe	static	0.33	0.12
Chahine et al; J Biomech; 2004 (D)	v	perp-par	linear	static	0.33	0.02
Chahine et al; J Biomech; 2004	v	zr	toe	static	0.33	0.1
Chahine et al; J Biomech; 2004	v	zr	toe	static	1.00	0.2
Chahine et al; J Biomech; 2004	v	rz	linear	static	0.33	0.035
Chahine et al; J Biomech; 2004	v	rz	linear	static	1.00	0.065
Krishnan et al; J Biomech; 2003	Hac	z	toe	static	0.25	0.32
Krishnan et al; J Biomech; 2003	Hac	z	toe	static	0.50	0.46
Krishnan et al; J Biomech; 2003	Hac	z	toe	static	0.75	0.59
Krishnan et al; J Biomech; 2003	Hac	z	toe	static	1.00	0.73
Krishnan et al; J Biomech; 2003	Hat	z	toe	static	0.25	10.1
Krishnan et al; J Biomech; 2003	Hat	z	toe	static	0.50	5.07
Krishnan et al; J Biomech; 2003	Hat	z	toe	static	0.75	4.61
Krishnan et al; J Biomech; 2003	Hat	z	toe	static	1.00	4.07
Krishnan et al; J Biomech; 2003	k	z	toe	static	0.25	3.90E-16
Krishnan et al; J Biomech; 2003	k	z	toe	static	0.50	5.90E-16
Krishnan et al; J Biomech; 2003	k	z	toe	static	0.75	4.40E-16
Krishnan et al; J Biomech; 2003	k	z	toe	static	1.00	5.80E-16
Krishnan et al; J Biomech; 2003	k	r	toe	static	0.25	1.00E-15
Krishnan et al; J Biomech; 2003	k	r	toe	static	0.50	1.18E-15
Krishnan et al; J Biomech; 2003	k	r	toe	static	0.75	1.31E-15
Krishnan et al; J Biomech; 2003	k	r	toe	static	1.00	1.86E-15
Krishnan et al; J Biomech; 2003 (P)	lambda		toe	static	0.25	1.70E-01
Krishnan et al; J Biomech; 2003 (P)	lambda		toe	static	0.50	2.60E-01
Krishnan et al; J Biomech; 2003 (P)	lambda		toe	static	0.75	3.20E-01
Krishnan et al; J Biomech; 2003 (P)	lambda		toe	static	1.00	2.90E-01
Chen et al; OA and Cartilage; 2001	Ha	z	linear	static	0.25	2.00E+00
Chen et al; OA and Cartilage; 2001	Ha	z	linear	static	0.50	3.25E+00
Chen et al; OA and Cartilage; 2001	Ha	z	linear	static	0.75	6.00E+00
Chen et al; OA and Cartilage; 2001 (P)	K-bulk	z	linear	static	0.25	9.00E-01
Chen et al; OA and Cartilage; 2001 (P)	K-bulk	z	linear	static	0.50	1.25E+00
Chen et al; OA and Cartilage; 2001 (P)	K-bulk	z	linear	static	0.75	1.75E+00

Chen et al; OA and Cartilage; 2001 (P)	FCD	z	linear	static	0.25	1.60E-01
Chen et al; OA and Cartilage; 2001 (P)	FCD	z	linear	static	0.50	2.20E-01
Chen et al; OA and Cartilage; 2001 (P)	FCD	z	linear	static	0.75	2.50E-01
Chen et al; J Biomech; 2004	Ha	z	linear	static	0.33	3.10E-01
Chen et al; J Biomech; 2004	Ha	z	linear	static	0.67	5.90E-01
Chen et al; J Biomech; 2004	Ha	z	linear	static	1.00	8.20E-01
Chen et al; J Biomech; 2004	k	z	linear	static	0.33	1.56E-15
Chen et al; J Biomech; 2004	k	z	linear	static	0.67	4.50E-16
Chen et al; J Biomech; 2004	k	z	linear	static	1.00	1.20E-16
Treppo et al; JOR; 2000	Ha	z	linear	static	0.50	7.50E-01
Treppo et al; JOR; 2000	Ha	z	linear	static	1.00	1.40E+00
Jurvelin et al; J Biomech; 1997	v	rz	linear	static	0.10	6.80E-02
Jurvelin et al; J Biomech; 1997	v	rz	linear	static	1.00	2.25E-01
Jurvelin et al; J Biomech; 1997	v	rz	linear	dynamic	0.10	1.29E-01
Jurvelin et al; J Biomech; 1997	v	rz	linear	dynamic	1.00	5.93E-01

REFERENCES

1. Venn M, Maroudas A. Chemical composition and swelling of normal and osteoarthrotic femoral head cartilage. I. Chemical composition. *Ann Rheum Dis.* 1977; 36(2): 121-129.
2. Maroudas A, Bayliss MT, Venn MF. Further studies on the composition of human femoral head cartilage. *Ann Rheum Dis.* 1980; 39(5): 514-523.
3. Shen ZL, Dodge MR, Kahn H, Ballarini R, Eppell SJ. Stress-strain experiments on individual collagen fibrils. *Biophys J.* 2008; 95(8): 3956-3963.
4. Mow VC, Guo XE. Mechano-electrochemical properties of articular cartilage: their inhomogeneities and anisotropies. *Annu Rev Biomed Eng.* 2002; 4: 175-209.
5. Li LP, Soulhat J, Buschmann MD, Shirazi-Adl A. Nonlinear analysis of cartilage in unconfined ramp compression using a fibril reinforced poroelastic model. *Clin Biomech.* 1999; 14(9): 673-682.
6. Mow VC, Kuei SC, Lai WM, Armstrong CG. Biphasic creep and stress relaxation of articular cartilage in compression? Theory and experiments. *J Biomech Eng.* 1980; 102(1): 73-84.
7. Pawaskar SS, Ingham E, Fisher J, Jin Z. Fluid load support and contact mechanics of hemiarthroplasty in the natural hip joint. *Med Eng Phys.* 2011; 33(1): 96-105.
8. Soltz MA, Ateshian GA. Interstitial fluid pressurization during confined compression cyclical loading of articular cartilage. *Ann Biomed Eng.* 2000; 28(2): 150-159.
9. Clark JM. Variation of collagen fiber alignment in a joint surface: a scanning electron microscope study of the tibial plateau in dog, rabbit, and man. *J Orthop Res.* 1991; 9(2): 246-257.
10. Clarke IC. Articular cartilage: a review and scanning electron microscope study. 1. The interterritorial fibrillar architecture. *J Bone Joint Surg Br.* 1971; 53(4): 732-750.
11. Bisson L, Brahmabhatt V, Marzo J. Split-line orientation of the talar dome articular cartilage. *Arthroscopy.* 2005; 21(5): 570-573.
12. Leo BM, Turner MA, Diduch DR. Split-line pattern and histologic analysis of a human osteochondral plug graft. *Arthroscopy.* 2004; 20 Suppl 2: 39-45.
13. Bae WC, Wong VW, Hwang J, Antonacci JM, Nugent-Derfus GE, Blewis ME, Temple-Wong MM, Sah RL. Wear-lines and split-lines of human patellar cartilage: relation to tensile biomechanical properties. *Osteoarthritis Cartilage.* 2008; 16(7): 841-845.

14. Saarakkala S, Julkunen P, Kiviranta P, Makitalo J, Jurvelin JS, Korhonen RK. Depth-wise progression of osteoarthritis in human articular cartilage: investigation of composition, structure and biomechanics. *Osteoarthritis Cartilage*. 2010; 18(1): 73-81.
15. Appleyard RC, Burkhardt D, Ghosh P, Read R, Cake M, Swain MV, Murrell GA. Topographical analysis of the structural, biochemical and dynamic biomechanical properties of cartilage in an ovine model of osteoarthritis. *Osteoarthritis Cartilage*. 2003; 11(1): 65-77.
16. Barker MK, Seedhom BB. The relationship of the compressive modulus of articular cartilage with its deformation response to cyclic loading: does cartilage optimize its modulus so as to minimize the strains arising in it due to the prevalent loading regime? *Rheumatology*. 2001; 40(3): 274-284.
17. Boschetti F, Pennati G, Gervaso F, Peretti GM, Dubini G. Biomechanical properties of human articular cartilage under compressive loads. *Biorheology*. 2004; 41(3-4): 159-166.
18. Boschetti F, Gervaso F, Pennati G, Peretti GM, Vena P, Dubini G. Poroelastic numerical modelling of natural and engineered cartilage based on in vitro tests. *Biorheology*. 2006; 43(3-4): 235-247.
19. Julkunen P, Harjula T, Iivarinen J, Marjanen J, Seppanen K, Narhi T, Arokoski J, Lammi MJ, Brama PA, Jurvelin JS, Helminen HJ. Biomechanical, biochemical and structural correlations in immature and mature rabbit articular cartilage. *Osteoarthritis Cartilage*. 2009; 17(12): 1628-1638.
20. Jin H, Lewis JL. Determination of Poisson's ratio of articular cartilage by indentation using different-sized indenters. *J Biomech Eng*. 2004; 126(2): 138-145.
21. Park S, Hung CT, Ateshian GA. Mechanical response of bovine articular cartilage under dynamic unconfined compression loading at physiological stress levels. *Osteoarthritis Cartilage*. 2004; 12(1): 65-73.
22. Li LP, Korhonen RK, Iivarinen J, Jurvelin JS, Herzog W. Fluid pressure driven fibril reinforcement in creep and relaxation tests of articular cartilage. *Med Eng Phys*. 2008; 30(2): 182-189.
23. Aspden RM, Jeffrey JE, Burgin LV. Impact loading of articular cartilage. *Osteoarthritis Cartilage*. 2002; 10(7): 588-9.
24. Finlay JB, Repo RU. Energy absorbing ability of articular cartilage during impact. *Med Biol Eng Comput*. 1979; 17(3): 397-403.
25. Finlay JB, Repo RU. Cartilage impact in vitro: effect of bone and cement. *J Biomech*. 1978; 11(8-9): 379-388.

26. Finlay JB, Repo RU. Impact characteristics of articular cartilage. *ISA Trans.* 1978; 17(1): 29-34.
27. Finlay JB, Repo RU. Impact characteristics of articular cartilage. *Biomed Sci Instrum.* 1977; 13: 47-50.
28. Repo RU, Finlay JB. Survival of articular cartilage after controlled impact. *J Bone Joint Surg Am.* 1977; 59(8): 1068-1076.
29. Burgin LV, Aspden RM. Impact testing to determine the mechanical properties of articular cartilage in isolation and on bone. *J Mater Sci Mater Med.* 2008; 19(2): 703-711.
30. Burgin LV, Aspden RM. A drop tower for controlled impact testing of biological tissues. *Med Eng Phys.* 2007; 29(4): 525-530.
31. Martin JA, Brown TD, Heiner AD, Buckwalter JA. Chondrocyte senescence, joint loading and osteoarthritis. *Clin Orthop Relat Res.* 2004(427 Suppl): S96-103.
32. Kamiya T, Tanimoto K, Tanne Y, Lin YY, Kunimatsu R, Yoshioka M, Tanaka N, Tanaka E, Tanne K. Effects of mechanical stimuli on the synthesis of superficial zone protein in chondrocytes. *J Biomed Mater Res A.* 2009; 92(2): 801-5.
33. Gavenis K, Andereya S, Schmidt-Rohlfing B, Mueller-Rath R, Silny J, Schneider U. Millicurrent stimulation of human articular chondrocytes cultivated in a collagen type-I gel and of human osteochondral explants. *BMC Complement Altern Med.* 2010; 10: 43.
34. Brighton CT, Wang W, Clark CC. The effect of electrical fields on gene and protein expression in human osteoarthritic cartilage explants. *J Bone Joint Surg Am.* 2008; 90(4): 833-848.
35. Parkkinen JJ, Lammi MJ, Helminen HJ, Tammi M. Local stimulation of proteoglycan synthesis in articular cartilage explants by dynamic compression in vitro. *J Orthop Res.* 1992; 10(5): 610-620.
36. Valhmu WB, Stazzone EJ, Bachrach NM, Saed-Nejad F, Fischer SG, Mow VC, Ratcliffe A. Load-controlled compression of articular cartilage induces a transient stimulation of aggrecan gene expression. *Arch Biochem Biophys.* 1998; 353(1): 29-36.
37. Guilak F, Ratcliffe A, Mow VC. Chondrocyte deformation and local tissue strain in articular cartilage: a confocal microscopy study. *J Orthop Res.* 1995; 13(3): 410-421.
38. Palmer GD, Chao Ph PH, Raia F, Mauck RL, Valhmu WB, Hung CT. Time-dependent aggrecan gene expression of articular chondrocytes in response to hyperosmotic loading. *Osteoarthritis Cartilage.* 2001; 9(8): 761-770.

39. Jin M, Frank EH, Quinn TM, Hunziker EB, Grodzinsky AJ. Tissue shear deformation stimulates proteoglycan and protein biosynthesis in bovine cartilage explants. *Arch Biochem Biophys*. 2001; 395(1): 41-48.
40. Frank EH, Jin M, Loening AM, Levenston ME, Grodzinsky AJ. A versatile shear and compression apparatus for mechanical stimulation of tissue culture explants. *J Biomech*. 2000; 33(11): 1523-1527.
41. Fioravanti A, Collodel G, Petraglia A, Nerucci F, Moretti E, Galeazzi M. Effect of hydrostatic pressure of various magnitudes on osteoarthritic chondrocytes exposed to IL-1beta. *Indian J Med Res*. 2010; 132: 209-217.
42. Knight MM, Toyoda T, Lee DA, Bader DL. Mechanical compression and hydrostatic pressure induce reversible changes in actin cytoskeletal organisation in chondrocytes in agarose. *J Biomech*. 2006; 39(8): 1547-1551.
43. Juang YM, Lee CY, Hsu WY, Lin CT, Lai CC, Tsai FJ. Proteomic analysis of chondrocytes exposed to pressure. *Biomed Chromatogr*. 2010; 24(12): 1273-1282.
44. Buschmann MD, Kim YJ, Wong M, Frank E, Hunziker EB, Grodzinsky AJ. Stimulation of aggrecan synthesis in cartilage explants by cyclic loading is localized to regions of high interstitial fluid flow. *Arch Biochem Biophys*. 1999; 366(1): 1-7.
45. Huang CY, Gu WY. Effects of tension-compression nonlinearity on solute transport in charged hydrated fibrous tissues under dynamic unconfined compression. *J Biomech Eng*. 2007; 129(3): 423-429.
46. Malaviya P, Nerem RM. Fluid-induced shear stress stimulates chondrocyte proliferation partially mediated via TGF-beta1. *Tissue Eng*. 2002; 8(4): 581-590.
47. Smith RL, Donlon BS, Gupta MK, Mohtai M, Das P, Carter DR, Cooke J, Gibbons G, Hutchinson N, Schurman DJ. Effects of fluid-induced shear on articular chondrocyte morphology and metabolism in vitro. *J Orthop Res*. 1995; 13(6): 824-831.
48. Sun HB. Mechanical loading, cartilage degradation, and arthritis. *Ann N Y Acad Sci*. 2010; 1211: 37-50.
49. Borrelli J, Jr, Zhu Y, Burns M, Sandell L, Silva MJ. Cartilage tolerates single impact loads of as much as half the joint fracture threshold. *Clin Orthop Relat Res*. 2004(426): 266-273.
50. Flachsmann R, Broom ND, Hardy AE. Deformation and rupture of the articular surface under dynamic and static compression. *J Orthop Res*. 2001; 19(6): 1131-1139.
51. Torzilli PA, Deng XH, Ramcharan M. Effect of compressive strain on cell viability in statically loaded articular cartilage. *Biomech Model Mechanobiol*. 2006; 5(2-3): 123-132.

52. Burton-Wurster N, Vernier-Singer M, Farquhar T, Lust G. Effect of compressive loading and unloading on the synthesis of total protein, proteoglycan, and fibronectin by canine cartilage explants. *J Orthop Res.* 1993; 11(5): 717-729.
53. Gray ML, Pizzanelli AM, Grodzinsky AJ, Lee RC. Mechanical and physiochemical determinants of the chondrocyte biosynthetic response. *J Orthop Res.* 1988; 6(6): 777-792.
54. Quinn TM, Kocian P, Meister JJ. Static compression is associated with decreased diffusivity of dextrans in cartilage explants. *Arch Biochem Biophys.* 2000; 384(2): 327-334.
55. Thibault M, Poole AR, Buschmann MD. Cyclic compression of cartilage/bone explants in vitro leads to physical weakening, mechanical breakdown of collagen and release of matrix fragments. *J Orthop Res.* 2002; 20(6): 1265-1273.
56. Burton-Wurster N, Vernier-Singer M, Farquhar T, Lust G. Effect of compressive loading and unloading on the synthesis of total protein, proteoglycan, and fibronectin by canine cartilage explants. *J Orthop Res.* 1993; 11(5): 717-729.
57. Milentijevic D, Torzilli PA. Influence of stress rate on water loss, matrix deformation and chondrocyte viability in impacted articular cartilage. *J Biomech.* 2005; 38(3): 493-502.
58. Loening AM, James IE, Levenston ME, Badger AM, Frank EH, Kurz B, Nuttall ME, Hung HH, Blake SM, Grodzinsky AJ, Lark MW. Injurious mechanical compression of bovine articular cartilage induces chondrocyte apoptosis. *Arch Biochem Biophys.* 2000; 381(2): 205-212.
59. Roemhildt ML, Coughlin KM, Peura GD, Badger GJ, Churchill D, Fleming BC, Beynon BD. Effects of increased chronic loading on articular cartilage material properties in the Lapine tibio-femoral joint. *J Biomech.* 2010; 43(12): 2301-8.
60. Borrelli J,Jr, Zaegel MA, Martinez MD, Silva MJ. Diminished cartilage creep properties and increased trabecular bone density following a single, sub-fracture impact of the rabbit femoral condyle. *J Orthop Res.* 2010; 28(10): 1307-14.
61. Goodwin W, McCabe D, Sauter E, Reese E, Walter M, Buckwalter JA, Martin JA. Rotenone prevents impact-induced chondrocyte death. *J Orthop Res.* 2010; 28(8): 1057-1063.
62. Isaac DI, Meyer EG, Kopke KS, Haut RC. Chronic changes in the rabbit tibial plateau following blunt trauma to the tibiofemoral joint. *J Biomech.* 2010; 43(9): 1682-1688.
63. Verteramo A, Seedhom BB. Effect of a single impact loading on the structure and mechanical properties of articular cartilage. *J Biomech.* 2007; 40(16): 3580-3589.

64. Ewers BJ, Jayaraman VM, Banglmaier RF, Haut RC. Rate of blunt impact loading affects changes in retropatellar cartilage and underlying bone in the rabbit patella. *J Biomech.* 2002; 35(6): 747-755.
65. Szczodry M, Coyle CH, Kramer SJ, Smolinski P, Chu CR. Progressive chondrocyte death after impact injury indicates a need for chondroprotective therapy. *Am J Sports Med.* 2009; 37(12): 2318-2322.
66. Torzilli PA, Grigiene R, Borrelli J, Jr, Helfet DL. Effect of impact load on articular cartilage: cell metabolism and viability, and matrix water content. *J Biomech Eng.* 1999; 121(5): 433-441.
67. Backus JD, Furman BD, Swimmer T, Kent CL, McNulty AL, Defrate LE, Guilak F, Olson SA. Cartilage viability and catabolism in the intact porcine knee following transarticular impact loading with and without articular fracture. *J Orthop Res.* 2011; 29(4): 501-510.
68. Chen CT, Burton-Wurster N, Lust G, Bank RA, Tekoppele JM. Compositional and metabolic changes in damaged cartilage are peak-stress, stress-rate, and loading-duration dependent. *J Orthop Res.* 1999; 17(6): 870-879.
69. Brown TD, Johnston RC, Saltzman CL, Marsh JL, Buckwalter JA. Posttraumatic osteoarthritis: a first estimate of incidence, prevalence, and burden of disease. *J Orthop Trauma.* 2006; 20(10): 739-744.
70. Zgonis T, Stapleton JJ, Roukis TS. Use of circular external fixation for combined subtalar joint fusion and ankle distraction. *Clin Podiatr Med Surg.* 2008; 25(4): 745-53, xi.
71. Intema F, Van Roermund PM, Marijnissen AC, Cotofana S, Eckstein F, Castelein RM, Bijlsma JW, Mastbergen SC, Lafeber FP. Tissue structure modification in knee osteoarthritis by use of joint distraction: an open 1-year pilot study. *Ann Rheum Dis.* 2011.
72. van Roermund PM, Marijnissen AC, Lafeber FP. Joint distraction as an alternative for the treatment of osteoarthritis. *Foot Ankle Clin.* 2002; 7(3): 515-527.
73. Segal NA, Anderson DD, Iyer KS, Baker J, Torner JC, Lynch JA, Felson DT, Lewis CE, Brown TD. Baseline articular contact stress levels predict incident symptomatic knee osteoarthritis development in the MOST cohort. *J Orthop Res.* 2009; 27(12): 1562-1568.
74. Apprich S, Welsch GH, Mamisch TC, Szomolanyi P, Mayerhoefer M, Pinker K, Trattnig S. Detection of degenerative cartilage disease: comparison of high-resolution morphological MR and quantitative T2 mapping at 3.0 Tesla. *Osteoarthritis Cartilage.* 2010; 18(9): 1211-1217.

75. Nissi MJ, Toyras J, Laasanen MS, Rieppo J, Saarakkala S, Lappalainen R, Jurvelin JS, Nieminen MT. Proteoglycan and collagen sensitive MRI evaluation of normal and degenerated articular cartilage. *J Orthop Res.* 2004; 22(3): 557-564.
76. Burstein D. Tracking longitudinal changes in knee degeneration and repair. *J Bone Joint Surg Am.* 2009; 91 Suppl 1: 51-53.
77. Lyyra-Laitinen T, Niinimäki M, Toyras J, Lindgren R, Kiviranta I, Jurvelin JS. Optimization of the arthroscopic indentation instrument for the measurement of thin cartilage stiffness. *Phys Med Biol.* 1999; 44(10): 2511-2524.
78. Bae WC, Schumacher BL, Sah RL. Indentation probing of human articular cartilage: Effect on chondrocyte viability. *Osteoarthritis Cartilage.* 2007; 15(1): 9-18.
79. Huang YP, Zheng YP. Intravascular Ultrasound (IVUS): A Potential Arthroscopic Tool for Quantitative Assessment of Articular Cartilage. *Open Biomed Eng J.* 2009; 3: 13-20.
80. Matta JM. Fractures of the acetabulum: accuracy of reduction and clinical results in patients managed operatively within three weeks after the injury. *J Bone Joint Surg Am.* 1996; 78(11): 1632-1645.
81. Marsh JL, Weigel DP, Dirschl DR. Tibial plafond fractures. How do these ankles function over time? *J Bone Joint Surg Am.* 2003; 85-A(2): 287-295.
82. Chang A, Moisio K, Chmiel JS, Eckstein F, Guermazi A, Almagor O, Cahue S, Wirth W, Prasad P, Sharma L. Subregional effects of meniscal tears on cartilage loss over 2 years in knee osteoarthritis. *Ann Rheum Dis.* 2011; 70(1): 74-79.
83. Thomas TP, Anderson DD, Mosqueda TV, Van Hofwegen CJ, Hillis SL, Marsh JL, Brown TD. Objective CT-based metrics of articular fracture severity to assess risk for posttraumatic osteoarthritis. *J Orthop Trauma.* 2010; 24(12): 764-769.
84. Buckwalter JA, Brown TD. Joint injury, repair, and remodeling: roles in post-traumatic osteoarthritis. *Clin Orthop Relat Res.* 2004(423): 7-16.
85. Thompson RC, Jr, Oegema TR, Jr, Lewis JL, Wallace L. Osteoarthrotic changes after acute transarticular load. An animal model. *J Bone Joint Surg Am.* 1991; 73(7): 990-1001.
86. Jeffrey JE, Gregory DW, Aspden RM. Matrix damage and chondrocyte viability following a single impact load on articular cartilage. *Arch Biochem Biophys.* 1995; 322(1): 87-96.

87. Anderson DD, Mosqueda T, Thomas T, Hermanson EL, Brown TD, Marsh JL. Quantifying tibial plafond fracture severity: absorbed energy and fragment displacement agree with clinical rank ordering. *J Orthop Res.* 2008; 26(8): 1046-1052.
88. Thomas TP, Anderson DD, Marsh JL, Brown TD. A method for the estimation of normative bone surface area to aid in objective CT-based fracture severity assessment. *Iowa Orthop J.* 2008; 28: 9-13.
89. Beardsley CL, Anderson DD, Marsh JL, Brown TD. Interfragmentary surface area as an index of comminution severity in cortical bone impact. *J Orthop Res.* 2005; 23(3): 686-690.
90. Blokker CP, Rorabeck CH, Bourne RB. Tibial plateau fractures. An analysis of the results of treatment in 60 patients. *Clin Orthop Relat Res.* 1984(182): 193-199.
91. Lansinger O, Bergman B, Korner L, Andersson GB. Tibial condylar fractures. A twenty-year follow-up. *J Bone Joint Surg Am.* 1986; 68(1): 13-19.
92. Honkonen SE. Degenerative arthritis after tibial plateau fractures. *J Orthop Trauma.* 1995; 9(4): 273-277.
93. Hak DJ, Hamel AJ, Bay BK, Sharkey NA, Olson SA. Consequences of transverse acetabular fracture malreduction on load transmission across the hip joint. *J Orthop Trauma.* 1998; 12(2): 90-100.
94. Konrath GA, Hamel AJ, Sharkey NA, Bay BK, Olson SA. Biomechanical consequences of anterior column fracture of the acetabulum. *J Orthop Trauma.* 1998; 12(8): 547-552.
95. Mulcahy DM, McCormack DM, Stephens MM. Intra-articular calcaneal fractures: effect of open reduction and internal fixation on the contact characteristics of the subtalar joint. *Foot Ankle Int.* 1998; 19(12): 842-848.
96. Olson SA, Bay BK, Pollak AN, Sharkey NA, Lee T. The effect of variable size posterior wall acetabular fractures on contact characteristics of the hip joint. *J Orthop Trauma.* 1996; 10(6): 395-402.
97. Brown TD, Anderson DD, Nepola JV, Singerman RJ, Pedersen DR, Brand RA. Contact stress aberrations following imprecise reduction of simple tibial plateau fractures. *J Orthop Res.* 1988; 6(6): 851-862.
98. Li W, Anderson DD, Goldsworthy JK, Marsh JL, Brown TD. Patient-specific finite element analysis of chronic contact stress exposure after intraarticular fracture of the tibial plafond. *J Orthop Res.* 2008; 26(8): 1039-1045.

99. Anderson DD, Goldsworthy JK, Shivanna K, Grosland NM, Pedersen DR, Thomas TP, Tochigi Y, Marsh JL, Brown TD. Intra-articular contact stress distributions at the ankle throughout stance phase-patient-specific finite element analysis as a metric of degeneration propensity. *Biomech Model Mechanobiol.* 2006; 5(2-3): 82-89.
100. Bigliani LU, Weinstein DM, Glasgow MT, Pollock RG, Flatow EL. Glenohumeral arthroplasty for arthritis after instability surgery. *J Shoulder Elbow Surg.* 1995; 4(2): 87-94.
101. Graham GP, Fairclough JA. Early osteoarthritis in young sportsmen with severe anterolateral instability of the knee. *Injury.* 1988; 19(4): 247-248.
102. Kannus P, Jarvinen M. Posttraumatic anterior cruciate ligament insufficiency as a cause of osteoarthritis in a knee joint. *Clin Rheumatol.* 1989; 8(2): 251-260.
103. Maletius W, Messner K. Eighteen- to twenty-four-year follow-up after complete rupture of the anterior cruciate ligament. *Am J Sports Med.* 1999; 27(6): 711-717.
104. Sommerlath KG. Results of meniscal repair and partial meniscectomy in stable knees. *Int Orthop.* 1991; 15(4): 347-350.
105. McDevitt C, Gilbertson E, Muir H. An experimental model of osteoarthritis; early morphological and biochemical changes. *J Bone Joint Surg Br.* 1977; 59(1): 24-35.
106. McDevitt CA, Muir H. Biochemical changes in the cartilage of the knee in experimental and natural osteoarthritis in the dog. *J Bone Joint Surg Br.* 1976; 58(1): 94-101.
107. Dedrick DK, Goldstein SA, Brandt KD, O'Connor BL, Goulet RW, Albrecht M. A longitudinal study of subchondral plate and trabecular bone in cruciate-deficient dogs with osteoarthritis followed up for 54 months. *Arthritis Rheum.* 1993; 36(10): 1460-1467.
108. Lovasz G, Park SH, Ebramzadeh E, Benya PD, Llinas A, Bellyei A, Luck JV, Jr, Sarmiento A. Characteristics of degeneration in an unstable knee with a coronal surface step-off. *J Bone Joint Surg Br.* 2001; 83(3): 428-436.
109. McKinley TO, Rudert MJ, Koos DC, Brown TD. Incongruity versus instability in the etiology of posttraumatic arthritis. *Clin Orthop Relat Res.* 2004(423): 44-51.
110. McKinley TO, Rudert MJ, Koos DC, Pedersen DR, Baer TE, Tochigi Y, Brown TD. Contact stress transients during functional loading of ankle stepoff incongruities. *J Biomech.* 2006; 39(4): 617-626.
111. McKinley TO, McKinley T, Rudert MJ, Koos DC, Pedersen DR, Baer TE, Tochigi Y, Brown TD. Stance-phase aggregate contact stress and contact stress gradient changes

- resulting from articular surface stepoffs in human cadaveric ankles. *Osteoarthritis Cartilage*. 2006; 14(2): 131-138.
112. Moussavi-Harami SF, Pedersen DR, Martin JA, Hillis SL, Brown TD. Automated objective scoring of histologically apparent cartilage degeneration using a custom image analysis program. *J Orthop Res*. 2009; 27(4): 522-528.
113. Shamir L, Ling SM, Scott W, Hochberg M, Ferrucci L, Goldberg IG. Early detection of radiographic knee osteoarthritis using computer-aided analysis. *Osteoarthritis Cartilage*. 2009; 17(10): 1307-1312.
114. Green AE, Naghdi PM. Flow of fluid through an elastic solid. *Acta Mech*. 1970; 9(3-4): 329-340.
115. Mak AF, Lai WM, Mow VC. Biphasic indentation of articular cartilage--I. Theoretical analysis. *J Biomech*. 1987; 20(7): 703-714.
116. Mow VC, Gibbs MC, Lai WM, Zhu WB, Athanasiou KA. Biphasic indentation of articular cartilage--II. A numerical algorithm and an experimental study. *J Biomech*. 1989; 22(8-9): 853-861.
117. Korhonen RK, Laasanen MS, Toyras J, Lappalainen R, Helminen HJ, Jurvelin JS. Fibril reinforced poroelastic model predicts specifically mechanical behavior of normal, proteoglycan depleted and collagen degraded articular cartilage. *J Biomech*. 2003; 36(9): 1373-1379.
118. Garcia JJ, Cortes DH. A nonlinear biphasic viscohyperelastic model for articular cartilage. *J Biomech*. 2006; 39(16): 2991-2998.
119. Garcia JJ, Cortes DH. A biphasic viscohyperelastic fibril-reinforced model for articular cartilage: formulation and comparison with experimental data. *J Biomech*. 2007; 40(8): 1737-1744.
120. Lai WM, Hou JS, Mow VC. A triphasic theory for the swelling and deformation behaviors of articular cartilage. *J Biomech Eng*. 1991; 113(3): 245-258.
121. Lu XL, Wan LQ, Guo XE, Mow VC. A linearized formulation of triphasic mixture theory for articular cartilage, and its application to indentation analysis. *J Biomech*. 2010; 43(4): 673-679.
122. Li LP, Herzog W, Korhonen RK, Jurvelin JS. The role of viscoelasticity of collagen fibers in articular cartilage: axial tension versus compression. *Med Eng Phys*. 2005; 27(1): 51-57.

123. Lai WM, Mow VC, Roth V. Effects of nonlinear strain-dependent permeability and rate of compression on the stress behavior of articular cartilage. *J Biomech Eng.* 1981; 103(2): 61-66.
124. Goreham-Voss CM, McKinley TO, Brown TD. A finite element exploration of cartilage stress near an articular incongruity during unstable motion. *J Biomech.* 2007; 40(15): 3438-3447.
125. Chantarapanich N, Nanakorn P, Chernchujit B, Sitthiseripratip K. A finite element study of stress distributions in normal and osteoarthritic knee joints. *J Med Assoc Thai.* 2009; 92 Suppl 6: S97-103.
126. Yang N, Nayeb-Hashemi H, Canavan PK. The combined effect of frontal plane tibiofemoral knee angle and meniscectomy on the cartilage contact stresses and strains. *Ann Biomed Eng.* 2009; 37(11): 2360-2372.
127. Ateshian GA, Ellis BJ, Weiss JA. Equivalence between short-time biphasic and incompressible elastic material responses. *J Biomech Eng.* 2007; 129(3): 405-412.
128. Garcia JJ, Altiero NJ, Haut RC. An approach for the stress analysis of transversely isotropic biphasic cartilage under impact load. *J Biomech Eng.* 1998; 120(5): 608-613.
129. Anderson IA, Mucalo MR, Johnson GS, Lorier MA. The processing and characterization of animal-derived bone to yield materials with biomedical applications. Part III: material and mechanical properties of fresh and processed bovine cancellous bone. *J Mater Sci Mater Med.* 2000; 11(11): 743-749.
130. Li B, Aspden RM. Mechanical and material properties of the subchondral bone plate from the femoral head of patients with osteoarthritis or osteoporosis. *Ann Rheum Dis.* 1997; 56(4): 247-254.
131. Kelly PA, O'Connor JJ. Transmission of rapidly applied loads through articular cartilage. Part 2: Cracked cartilage. *Proc Inst Mech Eng H.* 1996; 210(1): 39-49.
132. LeRoux MA, Arokoski J, Vail TP, Guilak F, Hyttinen MM, Kiviranta I, Setton LA. Simultaneous changes in the mechanical properties, quantitative collagen organization, and proteoglycan concentration of articular cartilage following canine meniscectomy. *J Orthop Res.* 2000; 18(3): 383-392.
133. Milentijevic D, Rubel IF, Liew AS, Helfet DL, Torzilli PA. An in vivo rabbit model for cartilage trauma: a preliminary study of the influence of impact stress magnitude on chondrocyte death and matrix damage. *J Orthop Trauma.* 2005; 19(7): 466-473.
134. Morel V, Quinn TM. Cartilage injury by ramp compression near the gel diffusion rate. *J Orthop Res.* 2004; 22(1): 145-151.

135. Demarteau O, Pillet L, Inaebnit A, Borens O, Quinn TM. Biomechanical characterization and in vitro mechanical injury of elderly human femoral head cartilage: comparison to adult bovine humeral head cartilage. *Osteoarthritis Cartilage*. 2006; 14(6): 589-596.
136. Zhang H, Vrahas MS, Baratta RV, Rosler DM. Damage to rabbit femoral articular cartilage following direct impacts of uniform stresses: an in vitro study. *Clin Biomech*. 1999; 14(8): 543-548.
137. Mankin HJ, Dorfman H, Lippiello L, Zarins A. Biochemical and metabolic abnormalities in articular cartilage from osteo-arthritic human hips. II. Correlation of morphology with biochemical and metabolic data. *J Bone Joint Surg Am*. 1971; 53(3): 523-537.
138. Tomatsu T, Imai N, Takeuchi N, Takahashi K, Kimura N. Experimentally produced fractures of articular cartilage and bone. The effects of shear forces on the pig knee. *J Bone Joint Surg Br*. 1992; 74(3): 457-462.
139. Krueger JA, Thisse P, Ewers BJ, Dvoracek-Driksna D, Orth MW, Haut RC. The extent and distribution of cell death and matrix damage in impacted chondral explants varies with the presence of underlying bone. *J Biomech Eng*. 2003; 125(1): 114-119.
140. Ewers BJ, Dvoracek-Driksna D, Orth MW, Haut RC. The extent of matrix damage and chondrocyte death in mechanically traumatized articular cartilage explants depends on rate of loading. *J Orthop Res*. 2001; 19(5): 779-784.
141. Flachsmann R, Kistler M, Rentzios A, Broom ND. Influence of an initiating microsplit on the resistance to compression-induced rupture of the articular surface. *Connect Tissue Res*. 2006; 47(2): 77-84.
142. Flachsmann R, Kim W, Broom N. Vulnerability to rupture of the intact articular surface with respect to age and proximity to site of fibrillation: a dynamic and static-investigation. *Connect Tissue Res*. 2005; 46(3): 159-169.
143. Lei F, Szeri AZ. Inverse analysis of constitutive models: biological soft tissues. *J Biomech*. 2007; 40(4): 936-940.
144. DiSilvestro MR, Zhu Q, Suh JK. Biphasic poroviscoelastic simulation of the unconfined compression of articular cartilage: II--Effect of variable strain rates. *J Biomech Eng*. 2001; 123(2): 198-200.
145. DiSilvestro MR, Zhu Q, Wong M, Jurvelin JS, Suh JK. Biphasic poroviscoelastic simulation of the unconfined compression of articular cartilage: I--Simultaneous prediction of reaction force and lateral displacement. *J Biomech Eng*. 2001; 123(2): 191-197.

146. Lewis JL, Deloria LB, Oyen-Tiesma M, Thompson RC, Jr, Ericson M, Oegema TR, Jr. Cell death after cartilage impact occurs around matrix cracks. *J Orthop Res.* 2003; 21(5): 881-887.
147. Julkunen P, Kiviranta P, Wilson W, Jurvelin JS, Korhonen RK. Characterization of articular cartilage by combining microscopic analysis with a fibril-reinforced finite-element model. *J Biomech.* 2007; 40(8): 1862-1870.
148. Li LP, Buschmann MD, Shirazi-Adl A. A fibril reinforced nonhomogeneous poroelastic model for articular cartilage: inhomogeneous response in unconfined compression. *J Biomech.* 2000; 33(12): 1533-1541.
149. Buckley MR, Gleghorn JP, Bonassar LJ, Cohen I. Mapping the depth dependence of shear properties in articular cartilage. *J Biomech.* 2008; 41(11): 2430-2437.
150. Chen AC, Bae WC, Schinagl RM, Sah RL. Depth- and strain-dependent mechanical and electromechanical properties of full-thickness bovine articular cartilage in confined compression. *J Biomech.* 2001; 34(1): 1-12.
151. Verteramo A, Seedhom BB. Zonal and directional variations in tensile properties of bovine articular cartilage with special reference to strain rate variation. *Biorheology.* 2004; 41(3-4): 203-213.
152. Ateshian GA, Maas S, Weiss JA. Finite Element Algorithm for Frictionless Contact of Porous Permeable Media Under Finite Deformation and Sliding. *J Biomech Eng.* 2010; 132(6): 610061-6100613.
153. Zheng YP, Niu HJ, Arthur Mak FT, Huang YP. Ultrasonic measurement of depth-dependent transient behaviors of articular cartilage under compression. *J Biomech.* 2005; 38(9): 1830-1837.
154. Neu CP, Hull ML, Walton JH. Heterogeneous three-dimensional strain fields during unconfined cyclic compression in bovine articular cartilage explants. *J Orthop Res.* 2005; 23(6): 1390-1398.
155. Borrelli J, Jr, Burns ME, Ricci WM, Silva MJ. A method for delivering variable impact stresses to the articular cartilage of rabbit knees. *J Orthop Trauma.* 2002; 16(3): 182-188.
156. Donzelli PS, Spilker RL, Ateshian GA, Mow VC. Contact analysis of biphasic transversely isotropic cartilage layers and correlations with tissue failure. *J Biomech.* 1999; 32(10): 1037-1047.
157. Atkinson TS, Haut RC, Altiero NJ. Impact-induced fissuring of articular cartilage: an investigation of failure criteria. *J Biomech Eng.* 1998; 120(2): 181-187.

158. Furman BD, Strand J, Hembree WC, Ward BD, Guilak F, Olson SA. Joint degeneration following closed intraarticular fracture in the mouse knee: a model of posttraumatic arthritis. *J Orthop Res.* 2007; 25(5): 578-592.
159. Intema F, DeGroot J, Elshof B, Vianen ME, Yocum S, Zuurmond A, Mastbergen SC, Lafeber FP. The canine bilateral groove model of osteoarthritis. *J Orthop Res.* 2008; 26(11): 1471-1477.
160. Funakoshi Y, Hariu M, Tapper JE, Marchuk LL, Shrive NG, Kanaya F, Rattner JB, Hart DA, Frank CB. Periarticular ligament changes following ACL/MCL transection in an ovine stifle joint model of osteoarthritis. *J Orthop Res.* 2007; 25(8): 997-1006.
161. Gabriel N, Innes JF, Caterson B, Vaughan-Thomas A. Development of an in vitro model of feline cartilage degradation. *J Feline Med Surg.* 2010; 12(8): 614-620.
162. Huser CA, Davies ME. Calcium signaling leads to mitochondrial depolarization in impact-induced chondrocyte death in equine articular cartilage explants. *Arthritis Rheum.* 2007; 56(7): 2322-2334.
163. Julkunen P, Halmesmaki EP, Iivarinen J, Rieppo L, Narhi T, Marjanen J, Rieppo J, Arokoski J, Brama PA, Jurvelin JS, Helminen HJ. Effects of growth and exercise on composition, structural maturation and appearance of osteoarthritis in articular cartilage of hamsters. *J Anat.* 2010; 217(3): 262-274.
164. Blumberg TJ, Natoli RM, Athanasiou KA. Effects of doxycycline on articular cartilage GAG release and mechanical properties following impact. *Biotechnol Bioeng.* 2008; 100(3): 506-515.
165. Haut RC, Ide TM, De Camp CE. Mechanical responses of the rabbit patello-femoral joint to blunt impact. *J Biomech Eng.* 1995; 117(4): 402-408.
166. Duda GN, Maldonado ZM, Klein P, Heller MO, Burns J, Bail H. On the influence of mechanical conditions in osteochondral defect healing. *J Biomech.* 2005; 38(4): 843-851.
167. Rothstock S, Uhlenbrock A, Bishop N, Laird L, Nassutt R, Morlock M. Influence of interface condition and implant design on bone remodelling and failure risk for the resurfaced femoral head. *J Biomech.* 2011; 44(9): 1646-1653.
168. Maxian TA, Brown TD, Pedersen DR, Callaghan JJ. Adaptive finite element modeling of long-term polyethylene wear in total hip arthroplasty. *J Orthop Res.* 1996; 14(4): 668-675.
169. Lundberg HJ, Stewart KJ, Pedersen DR, Callaghan JJ, Brown TD. Nonidentical and outlier duty cycles as factors accelerating UHMWPE wear in THA: a finite element exploration. *J Orthop Res.* 2007; 25(1): 30-43.

170. Goreham-Voss CM, Hyde PJ, Hall RM, Fisher J, Brown TD. Cross-shear implementation in sliding-distance-coupled finite element analysis of wear in metal-on-polyethylene total joint arthroplasty: Intervertebral total disc replacement as an illustrative application. *J Biomech.* 2010; 43(9): 1674-1681.
171. Stok K, Oloyede A. Conceptual fracture parameters for articular cartilage. *Clin Biomech.* 2007; 22(6): 725-735.
172. Ateshian GA, Likhitpanichkul M, Hung CT. A mixture theory analysis for passive transport in osmotic loading of cells. *J Biomech.* 2006; 39(3): 464-475.
173. Albro MB, Chahine NO, Li R, Yeager K, Hung CT, Ateshian GA. Dynamic loading of deformable porous media can induce active solute transport. *J Biomech.* 2008; 41(15): 3152-3157.